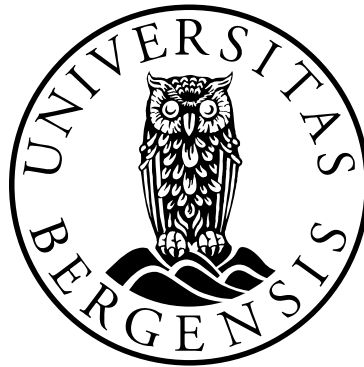


NEAR-SURFACE PETROCHEMICAL SENSING USING COPLANAR WAVEGUIDES



Magnus Lien Solberg

MASTER PROJECT

Measurement Science and Instrumentation

**Department of Physics and Technology
Faculty of Mathematics and Natural Sciences
University of Bergen**

ABSTRACT

The project studies the ability of coplanar waveguide sensor in sensing thin layers of petrochemical liquid. A coplanar waveguide is built on flexible printable circuit board partially based on an existing design. Two sensors are constructed with the coplanar waveguide to test the industrial applicability of sensor mounted on the inside of pipe wall. Simulation tool are used to examine the viability of incorporating simulation in microwave frequency experiments and sensor design. The experiments focus on performance of the sensors and place emphasis on the measurement output of liquid with non-uniform thickness.

The test liquid stays above the entire surface of the coplanar waveguide sensor. At the side of the sensor, a vertical transition is implemented to connect coplanar waveguide to coaxial one. Microwave frequency range signal is excited at the ports, and interacts with the liquid as it is transmitted on the coplanar waveguide. The effective permittivity, influenced by both the thickness and the permittivity of the test liquid above the coplanar waveguide, affects the characteristic of the transmission of the wave between the ports. Thus, the measured S-parameters can be used to interpret the permittivity.

The sensors in the project produce more accurate permittivity measurements than the old prototype for frequencies below 200 MHz. The viability of coplanar waveguide built on flexible printed circuit board is therefore verified as effective in near-surface permittivity measurements. Bending of the coplanar waveguide has minimum influence on the measurements. It is therefore concluded that it should be possible to place it in-line on the pipe wall. The simulation software is confirmed to be stable in producing realistic result within the frequency range and permittivity range in the project. Non-uniform thin layers of the petroleum products can be measured by permittivity measurement using the coplanar waveguide sensors. A small change in effective permittivity caused by thickness variation can be detected regardless of the type of test liquid. The calculated effective permittivity of test liquid does not vary as long as the average thickness across the sensor area is the same. The thickness non-uniformity therefore does not affect significantly the effective permittivity of the test liquid.

ACKNOWLEDGEMENTS

I would like to thank the following persons for their great help during this project:

I thank Kjetil Folgerø for his continuous help in the project at Christian Michelsen Research. Kjetil put much effort into ensuring that I have minimum obstacles during the construction process of the sensor.

I thank Bjørn Tore Hjertaker for his caring throughout the process of the master degree, both technically and morally.

I thank Sigve Naustdal and Truls Anderson for his moral support and friendship during the master study.

I thank Kjetil Haukalid for his engagement when I needed consultation as well as help about sensor A.

I thank Bård Henriksen for his help for formatting files for the making of the conductor part of the coplanar waveguide.

I thank Jan Kocbach for his advices in the use of software COMSOL.

I thank Alan, Eunice, Jahara, Jelena and Bjørn Carlsen for the support in both professional and private support.

I thank Jo Inge Bitubekk for his continuous support and friendship.

Finally, I thank my family and all my friends that have supported me throughout the master study.

CONTENTS

1 INTRODUCTION	1
1.1 MOTIVATION	1
1.2 BACKGROUND	2
1.3 OBJECTIVES.....	3
1.4 OUTLINE.....	4
2 THEORY	5
2.1 DIELECTRIC THEORY	5
2.1.1 Dielectric.....	5
2.1.2 Electric dipole	5
2.1.3 Permittivity.....	7
2.2 USING TRANSMISSION LINES FOR MEASUREMENT OF MATERIAL PROPERTIES	10
2.2.1 Transmission line	10
2.2.2 Scattering parameters	11
2.2.3 Dielectric spectroscopy.....	12
2.3 COPLANAR WAVEGUIDES	14
2.4 NATURAL GAS HYDRATES	16
3 SENSOR DESIGN AND SIMULATIONS	19
3.1 DESIGN OF THE COPLANAR WAVEGUIDE	20
3.1.1 Coplanar lines on PCB	20
3.1.2 Transition between coaxial and coplanar waveguides	25
3.2 MODELLING OF SENSOR A	28
3.3 SIMULATIONS ON SENSOR A	30
3.3.1 Software modelling and simulation.....	30
3.3.2 Preliminary testing.....	31
3.3.3 Simulation configuration.....	33
3.3.4 Results	33
3.3.5 Verification of simulation.....	35

3.4 MODELLING OF SENSOR B.....	38
3.5 SIMULATIONS ON SENSOR B	39
3.5.1 <i>Simulation configuration</i>	39
3.5.2 <i>Results</i>	42
3.6 DESIGN OF SENSOR B AND SENSOR C	46
3.6.1 <i>Structure of sensor B</i>	46
3.6.2 <i>Structure of sensor C</i>	47
4 EXPERIMENTS	49
4.1 EXPERIMENTS REPEATED ON SENSOR A.....	49
4.1.1 <i>Setup and procedure</i>	49
4.1.2 <i>Results</i>	50
4.2 EXPERIMENTS ON SENSOR B.....	54
4.2.1 <i>Setup and procedure</i>	54
4.2.2 <i>Results</i>	59
4.3 EXPERIMENTS ON SENSOR C.....	63
4.3.1 <i>Setup and procedure</i>	63
4.3.2 <i>Results</i>	63
5 DISCUSSION	69
5.1 COMPARISON BETWEEN SENSORS	69
5.1.1 <i>Sensor A and sensor B</i>	69
5.1.2 <i>Sensor B and sensor C</i>	72
5.1.3 <i>Calculated relative permittivity</i>	73
5.2 SIMULATION AND EXPERIMENT	75
5.3 LEAKAGE OF LIQUID IN EXPERIMENT	77
5.4 SENSING OF NON-UNIFORM LAYERS.....	78
5.4.1 <i>Effective permittivity and non-uniformity</i>	79
6 SUMMARY	83
6.1 CONCLUSION.....	83

6.2 OUTLOOK	84
REFERENCES	87
APPENDIX	91

LIST OF FIGURES

FIGURE 1.1 SKETCH OF SENSOR BUILT FROM PREVIOUS PROJECT WITH MOUNTED TEST CHAMBER (BLUE) AND CONNECTOR (DARK ORANGE) CONNECTED TO COAXIAL CABLE (BLACK) (HAUKALID, 2011).....	3
FIGURE 2.1 BALL-AND-STICK MODEL OF A WATER MOLECULE.....	6
FIGURE 2.2 A DIPOLE CONSISTS OF TWO POINTS WITH OPPOSITE CHARGES.....	6
FIGURE 2.3 FREQUENCY DEPENDENCY OF COMPLEX PERMITTIVITY	9
FIGURE 2.4 DEBYE-RELAXATION FOR SOME NON-CONDUCTIVE MATERIAL ("DIPOLE RELAXATION," N. D.).....	10
FIGURE 2.5 SCHEMATIC GRAPH OF A TWO-PORT NETWORK.....	12
FIGURE 2.6 STRUCTURAL DIMENSIONS OF A CPW	15
FIGURE 2.7 TYPICAL STRUCTURE OF GAS HYDRATE	17
FIGURE 3.1 GEOMETRY OF THE COPLANAR LINE.	22
FIGURE 3.2 DIMENSION DETAILS OF THE PCB AROUND CPW TO COAXIAL TRANSITION. .	23
FIGURE 3.3 PHOTOGRAPH OF THE CPW PRODUCED ON FLEXIBLE PCB.....	24
FIGURE 3.4 VERTICAL-MOUNTED SMA CONNECTOR AS TRANSITION FROM THE COAXIAL CABLE TO THE CPW.....	26
FIGURE 3.5 DESIGN DETAIL OF CPW NEAR THE TRANSITION AREA FOR THE COAXIAL CONNECTOR.	27
FIGURE 3.6 SENSOR A (HAUKALID, 2011) AND ITS MODEL IN COMSOL MULTIPHYSICS.	28
FIGURE 3.7 THE EXCITATION PORT OF THE MODELLED SENSOR.....	29
FIGURE 3.8 THE COPLANAR LINE STRUCTURE OF THE MODELLED SENSOR.	30
FIGURE 3.9 CONVERGENCE TEST OF SIMULATION AS A FUNCTION OF DIFFERENT MESH RESOLUTIONS	32
FIGURE 3.10 THE SIMULATED FREQUENCY RESPONSE OF MAGNITUDE AND PHASE OF S-PARAMETERS ON SENSOR A WITH AIR AS MUT.....	34
FIGURE 3.11 THE SIMULATED FREQUENCY RESPONSE OF MAGNITUDE AND PHASE OF S-PARAMETERS ON SENSOR A WITH WATER AS MUT.	35

FIGURE 3.12 THE REFLECTION AND TRANSMISSION LOSS ON SENSOR A WITH AIR AS MUT.	36
FIGURE 3.13 THE REFLECTION AND TRANSMISSION LOSS ON SENSOR A WITH WATER AS MUT.....	37
FIGURE 3.14 THE MODEL OF SENSOR B	38
FIGURE 3.15 ‘FINER’ MESH CONFIGURATION USED FOR SENSOR B.....	39
FIGURE 3.16 ‘EXTRA FINE’ MESH CONFIGURATION USED FOR SENSOR B.....	40
FIGURE 3.17 THE SLOPE GEOMETRY ESTABLISHED FOR MODEL OF SENSOR B.	42
FIGURE 3.18 MAGNITUDE AND PHASE OF MEASURED S-PARAMETERS WITH AIR AS MUT IN SIMULATION ON SENSOR B.	43
FIGURE 3.19 MAGNITUDE AND PHASE OF MEASURED S-PARAMETERS WITH WATER AS MUT IN THREE SIMULATION SCENARIOS ON SENSOR B.	44
FIGURE 3.20 MAGNITUDE AND PHASE OF MEASURED S-PARAMETERS WITH METHANOL AS MUT IN THREE SIMULATION SCENARIOS ON SENSOR B.	45
FIGURE 3.21 THE STRUCTURE OF SENSOR B AS SEEN FROM THE TOP AND THE BOTTOM. ..	47
FIGURE 3.22 THE STRUCTURE OF SENSOR C AS SEEN FROM THE TOP AND THE BOTTOM. ..	47
FIGURE 4.1 COMPARISON BETWEEN NEW AND OLD MEASUREMENT TAKEN WITH AIR AS MUT ON SENSOR A.....	51
FIGURE 4.2 COMPARISON BETWEEN NEW AND OLD MEASUREMENT TAKEN WITH WATER AS MUT ON SENSOR A.....	52
FIGURE 4.3 COMPARISON BETWEEN NEW AND OLD MEASUREMENT TAKEN WITH METHANOL AS MUT ON SENSOR A.	53
FIGURE 4.4 PHOTOGRAPH OF THE VERTICAL COAXIAL CONNECTION ON SENSOR B.	55
FIGURE 4.5 PHOTOGRAPH OF EXPERIMENT SETUP.	56
FIGURE 4.6 CLOSE PHOTOGRAPH FROM ABOVE SENSOR B DURING THE EXPERIMENT.	57
FIGURE 4.7 PHOTOGRAPH OF USING POM PHANTOM TO CONTROL THE THICKNESS OF MUT.....	58
FIGURE 4.8 MAGNITUDE AND PHASE OF MEASURED S-PARAMETERS WITH AIR AS MUT IN THREE EXPERIMENT SCENARIOS ON SENSOR B.	60

FIGURE 4.9 MAGNITUDE AND PHASE OF MEASURED S-PARAMETERS WITH WATER AS MUT IN THREE EXPERIMENT SCENARIOS ON SENSOR B.	61
FIGURE 4.10 MAGNITUDE AND PHASE OF MEASURED S-PARAMETERS WITH ETHANOL AS MUT IN THREE EXPERIMENT SCENARIOS ON SENSOR B.....	62
FIGURE 4.11 PHOTOGRAPH OF SENSOR C DURING THE EXPERIMENT.	63
FIGURE 4.12 MEASUREMENT RESULTS COMPARED FOR SENSOR B AND C WITH AIR AS MUT.....	64
FIGURE 4.13 MEASUREMENT RESULTS COMPARED FOR SENSOR B AND C WITH WATER AS MUT.....	65
FIGURE 4.14 MEASUREMENT RESULTS COMPARED FOR SENSOR B AND C WITH METHANOL AS MUT.....	66
FIGURE 4.15 MEASUREMENT RESULTS COMPARED FOR SENSOR B AND C WITH ETHANOL AS MUT.....	67
FIGURE 4.16 MEASUREMENT RESULTS COMPARED FOR SENSOR B AND C WITH VEGETABLE OIL AS MUT.....	68
FIGURE 5.1 MEASUREMENT RESULTS COMPARED FOR SENSOR A AND B WITH AIR AS MUT.	70
FIGURE 5.2 MEASUREMENT RESULTS COMPARED FOR SENSOR A AND B WITH WATER AS MUT.....	71
FIGURE 5.3 MEASUREMENT RESULTS COMPARED FOR SENSOR A AND B WITH METHANOL AS MUT.....	72
FIGURE 5.4 CALCULATED RELATIVE PERMITTIVITY OF METHANOL.....	74
FIGURE 5.5 COMPARISON BETWEEN EXPERIMENT AND SIMULATION RESULTS TAKEN WITH AIR AS MUT ON SENSOR B.....	75
FIGURE 5.6 COMPARISON BETWEEN EXPERIMENT AND SIMULATION RESULTS TAKEN WITH WATER AS MUT ON SENSOR B.	76
FIGURE 5.7 COMPARISON BETWEEN EXPERIMENT AND SIMULATION RESULTS TAKEN WITH METHANOL AS MUT ON SENSOR B.....	77
FIGURE 5.8 BRIEF COMPARISON OF CALCULATED PERMITTIVITY FOR ETHANOL WITH DIFFERENT THICKNESSES.....	79

FIGURE 5.9 CALCULATED EFFECTIVE PERMITTIVITY AS A FUNCTION OF THICKNESS OF ETHANOL.....	80
FIGURE 5.10 CALCULATED EFFECTIVE PERMITTIVITY AS A FUNCTION OF THICKNESS OF WATER.	81
FIGURE 5.11 CALCULATED EFFECTIVE PERMITTIVITY AS A FUNCTION OF THICKNESS OF AIR.	81
FIGURE 6.1 SPECIFICATION OF COAXIAL SMA CONNECTOR.....	93
FIGURE 6.2 COMPARISON BETWEEN NEW AND OLD MEASUREMENT TAKEN WITH 1-PENTANOL AS MUT ON SENSOR A.	94
FIGURE 6.3 COMPARISON BETWEEN NEW AND OLD MEASUREMENT TAKEN WITH ACETONE AS MUT ON SENSOR A.	95

LIST OF TABLES

TABLE 3.1 OVERVIEW OF THE SENSORS USED IN THIS PROJECT	19
TABLE 3.2 DIMENSIONS OF THE COPLANAR LINE.....	23
TABLE 4.1 EQUIPMENT USED IN THE EXPERIMENTS.....	49
TABLE 4.2 COLE-COLE PARAMETERS THAT DESCRIBE THE DIELECTRIC PROPERTIES OF MUTS AT 20 °C (HAUKALID, 2011; JAKOBSEN & FOLGERØ, 1997; VRBA & VRBA, 2013).	54
TABLE 6.1 TABLE OF DETAILED SPECIFICATIONS ON FPC	92

ABBREVIATIONS AND ACRONYMS

CPW	Coplanar Waveguide
FEM	Finite Element Method
GCPW	Grounded Coplanar Waveguide
MUT	Material Under Test
PCB	Printed Circuit Board
PMMA	Polymethyl methacrylate
POM	Polyoxymethylene
PVC	Polyvinyl chloride
SMA	SubMiniature version A
TEM	Transverse Electromagnetic

1 INTRODUCTION

In this chapter, the motivation and background of the project are presented. Following the project objectives are listed, and finally an outline of the thesis is given.

1.1 Motivation

The motivation for the project is to measure thin deposition layers of natural gas hydrates on the wall of pipelines transporting multiphase hydrocarbon.

Gas hydrates may form at process conditions constituting high pressures and low temperatures. The occurrence of hydrate formation in pipelines can have severe consequences concerning both safety and economic issues. Therefore, it is of importance to research real-time sensing methods for hydrate depositions, which can control the formation of hydrates in the pipeline and consequently the overall operational cost.

Hydrate deposits likely start to grow on the wall of the pipelines that transport petroleum products. Therefore, a measurement technology that allows for characterizing thin layers of hydrocarbon close to the wall is useful for monitoring hydrate deposits. On the other hand, the deposition of hydrates is a random process, and the thickness of the hydrates deposits on the pipe wall is usually not uniform. Consequently, it is important to be able to measure non-uniformity in thickness of the layers.

In short, an instrument able to detect and characterize the thickness of non-uniform hydrocarbon layers is required. As the permittivity spectrum of hydrates differ from the permittivity spectrum of water and oil (Jakobsen & Folgerø, 1997), near-wall permittivity measurements can be used to detect the presence of a hydrate layer and

possibly estimate the thickness of the layer. Coplanar waveguide (CPW) technology provides the possibility of conducting permittivity measurements on material that lies on a large plain area above the waveguide. The feasibility of using CPW to detect hydrocarbon layer and estimate its thickness through permittivity measurements is the focus of this project.

1.2 Background

CPWs are used in materials property characterization (Chen, 2004). The value of the effective dielectric constant of the material under test (MUT) alters with the frequency of the electromagnetic waves due to the dispersion of the permittivity across the spectrum. Therefore, measurement of the transmission and reflection properties using S-parameter measurements can be utilized to characterize the MUT by interpreting dielectric property.

During several research project between Christian Michelsen Research and the University of Bergen, a solid knowledge base on the measurement of hydrocarbons via dielectric spectroscopy methods have been developed. Prototypes of CPWs as sensors for measuring thin layers of hydrocarbon have been constructed and its feasibility verified in a previous master project (Haukalid, 2011). His project aimed to study the characteristics of CPW as a non-intrusive permittivity sensor. Dielectric spectroscopy is used as experimental method. The work placed emphasis on how cross-sectional dimensions and length of the sensor should be chosen to reach the highest possible sensitivity as well as the depth sensitivity (for liquid MUT with thickness from 0.5 mm to 8.5 mm), within a given permittivity range (2 to 80) and frequency range (10 MHz to 10 GHz). Depth sensitivity indicates how far into the MUT the sensor is sensitive to change in permittivity. Three sensors are constructed in the project. Figure 1.1 shows a sketch of one of the designs.

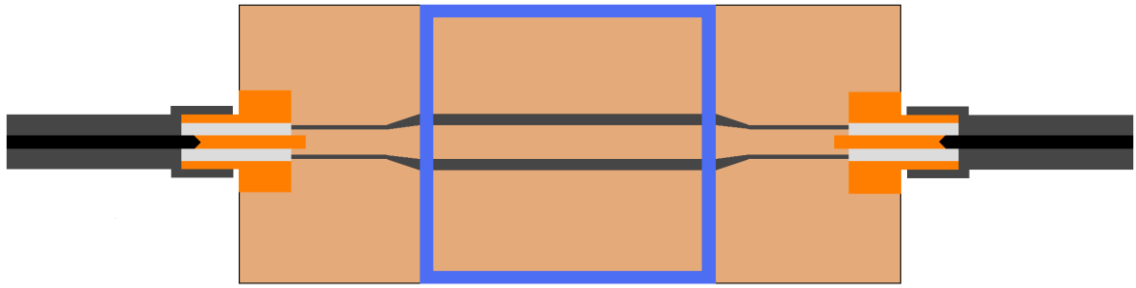


Figure 1.1 Sketch of sensor built from previous project with mounted test chamber (blue) and connector (dark orange) connected to coaxial cable (black) (Haukalid, 2011).

Measurements were conducted for 10 liquids with known permittivity on all three sensors. Results showed good agreement with data from the literature. The measurement uncertainty rises significantly for liquids with high permittivity at frequencies about 1 GHz.

The interesting results gained in Haukalid's master project are investigated further in this project with focus on examining the industrial applicability of CPW-based near-surface sensor.

1.3 Objectives

The aim of this project is to have a better understanding of using CPWs in sensing of hydrocarbon non-uniform thin layers close to the pipe wall surface. New CPW sensors have been designed and built based on Finite Element Method (FEM) simulations. The following objectives are set for the project work:

- i. To examine the reliability of the COMSOL multiphysics computational simulation tool providing realistic simulation results in microwave physics: In the project, the simulation tool can possibly provide additional information not easily available from actual experimental setups. Thus, this part of the project concerns the ability of the simulation tool to provide realistic simulation results. By clarifying the advantages and possible disadvantages of the simulation tool, useful experience can be passed on to future research making use of this simulation tool. The feasibility of the software is verified in the early phase of the project, and the software tool is used during the design phase of the sensors. In the concluding phase of the project, it is used to perform simulations under similar experimental conditions to those of the real experiments.

- ii. To design and test new sensors possessing properties able to carry it one-step closer to actual industrial applications: The main body of the sensor are made of a flexible material, together with a through-hole transition from the coaxial probe to the CPW. The purpose of this is for the sensor to be bended to fit the inner wall of an actual pipeline without intrusion. Obstacles experienced during the design and production phase are investigated and explained. This information will be helpful in further development work on the sensors.
- iii. To build knowledge on sensing of non-uniform thin layers using CPW sensors: the focus of the work is on how the measured reflection and transmission losses can be interpreted into effective permittivity measurements of the MUT, and how the effective permittivity measurement is related to the non-uniformity in the thickness of the MUT. As explained in the part of motivation, both the substance information of MUT and its non-uniform thickness are of importance concerning sensing of natural gas hydrate depositions.

1.4 Outline

The outline of the thesis is as follows:

Chapter 2 - introduces relevant theories related to the project, including dielectric theory, use of transmission lines in material characterization, CPW and natural gas hydrate.

Chapter 3 - concerns the design details of the sensors and their models, and presents the simulations performed on the sensors, including the simulation results.

Chapter 4 - describes the experiments conducted on the sensors. The experimental procedures are documented, and the results are presented.

Chapter 5 - analyses and discusses the simulation and experimental results from the chapter 3 and 4.

Chapter 6 – presents conclusions and suggests directions for further research.

2 THEORY

In this chapter, relevant theories related to the project are presented. These include dielectric theory, use of transmission lines in material characterization, CPWs and natural gas hydrate.

2.1 Dielectric theory

2.1.1 Dielectric

A dielectric material is an electrical insulator or a poor conductor that can be polarized by an applied electric field. When an electric field is posed on the dielectric material, almost no electric current runs through it. Instead, electric charges in the dielectric material align themselves with regard to the electric field applied. They shift from their equilibrium positions, and while positive charges tend to displace themselves towards the direction of the external electric field and the negative charges displace towards the opposite. The new alignment of the charges creates an internal electric field that counters the direction of the external electric field. Consequently, the overall electric field within the dielectric is reduced.

2.1.2 Electric dipole

An electric dipole is a pair of equal and opposite electric charges, the centres of which are not coincident. For example, as shown in Figure 2.1, a water molecule, in which two hydrogen atoms stick out on one side and form together with the oxygen atom as vertex a 105° angle, constitutes a permanent electric dipole.

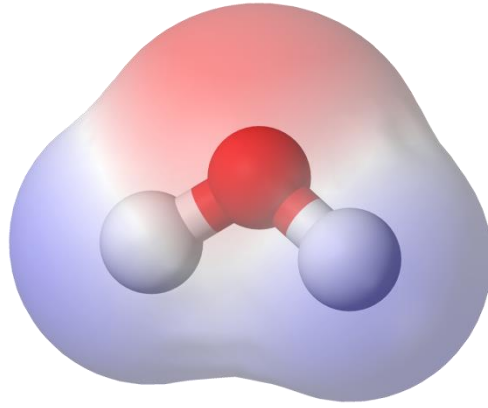


Figure 2.1 Ball-and-stick model of a water molecule where the red shade represents the negative pole and blue shade the positive pole ("Chemical polarity," n. d.).

In an external electric field, a dipole with opposite charges undergoes a torque, tending to rotate so that its axis becomes aligned with the direction of the electric field ("Electric dipole," 2015). Therefore, material consisting of permanent electric dipoles tends to be dielectric. An applied electric field on such a material will polarize it, causing the dipoles to realign, and creating an electric field inside the material.

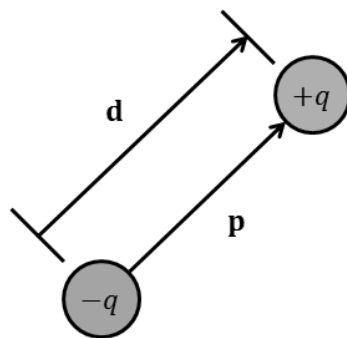


Figure 2.2 A dipole consists of two points with opposite charges.

In the simple case of two point charges, as shown in Figure 2.2, for opposite charges of magnitude q , the electric dipole moment \mathbf{p} is defined as the magnitude of the charge times the distance d between them with the direction pointing towards the positive charge:

$$\mathbf{p} = q\mathbf{d} \quad (1)$$

For a medium consisting of N such polarized particles with an average electric dipole moment of \mathbf{p} per unit volume, a property \mathbf{P} can be defined as a measure of how strong and how aligned the dipoles are in the medium. The polarization density \mathbf{P} is defined as the average electric dipole moment \mathbf{p} per unit volume of this dielectric material (Grant & Phillips, 1990):

$$\mathbf{P} = N\mathbf{p} = Nq\mathbf{d} \quad (2)$$

By this definition, the polarization density \mathbf{P} can be seen as a measure of the electrical field induced in the material when the dipoles realign in response to the external field.

2.1.3 Permittivity

The permittivity, denoted ε , is the measure of the resistance that is encountered when forming an electric field in a medium. In other words, permittivity is a measure of how an electric field affects, and is affected by, a dielectric medium. In dealing with polarization phenomena induced in dielectric in presence of external electric field, the quantity electric displacement field \mathbf{D} is defined as:

$$\mathbf{D} = \varepsilon_0\mathbf{E} + \mathbf{P} \quad (3)$$

where \mathbf{P} represents reaction of the material and \mathbf{E} as a field quantity induced by both the external sources and the sources within the material. $\varepsilon_0 = 8.854 \times 10^{-12}$ F/m is the permittivity of free space (vacuum permittivity).

In a linear, homogeneous, isotropic dielectric, \mathbf{P} depends linearly on the electric field:

$$\mathbf{P} = \varepsilon_0\chi\mathbf{E} \quad (4)$$

where χ is the electric susceptibility of the material.

By combining the two equations (3) and (4):

$$\mathbf{D} = \varepsilon_0(\chi + 1)\mathbf{E} = \varepsilon_0\varepsilon_r\mathbf{E} \quad (5)$$

where $\varepsilon_r = \chi + 1$ is the relative (to vacuum) permittivity of the material. Thus, the relationship between an existing field \mathbf{E} on the dielectric and the displacement field \mathbf{D} can be represented in a simpler way:

$$\mathbf{D} = \varepsilon_0 \varepsilon_r \mathbf{E} = \varepsilon \mathbf{E} \quad (6)$$

where $\varepsilon = \varepsilon_0 \varepsilon_r$ is the permittivity of the material.

Until now, the phenomenon caused by a static electric field posed on a dielectric medium has been described. However, the characteristic of this phenomenon is much more complex when an oscillating electric field is imposed across the dielectric. It takes a small amount of time for the dipoles or charges to realign to their final position when an oscillating external electric field is imposed. Therefore, when the frequency of the external field reaches a certain value, the bounded charges inside the dielectric will not be able to follow the electrical field change and realign themselves in time. This unspontaneous reaction is named dielectric relaxation and is represented by a phase difference between \mathbf{D} and \mathbf{E} , as follows:

$$\varepsilon^* = \frac{\mathbf{D}}{\mathbf{E}} = \varepsilon' - i\varepsilon'' \quad (7)$$

where ε becomes a complex quantity ε^* describing the dielectric property that is frequency dependent. Combined with equation (6), the complex relative permittivity can be represented as:

$$\varepsilon_r^* = \varepsilon_r' - i\varepsilon_r'' \quad (8)$$

Figure 2.3 shows how the complex permittivity of a material can vary as a function of frequency due to the dielectric relaxation. The frequency dependency is related to four main types of polarization: ionic polarization, rotational (dipolar) polarization, atomic polarization and electronic polarization. Ionic polarization is polarization caused by relative displacements between positive and negative ions in ionic crystals. In materials consisting of polar molecules, the electric field tends to direct these dipoles causing orientation polarization. Atomic polarization is caused by the displacement of atoms or atom groups in the molecule under the influence of external electric field, whereas electronic polarization is due to the displacement of nuclear and electrons in the atom under the influence of an external electric field.

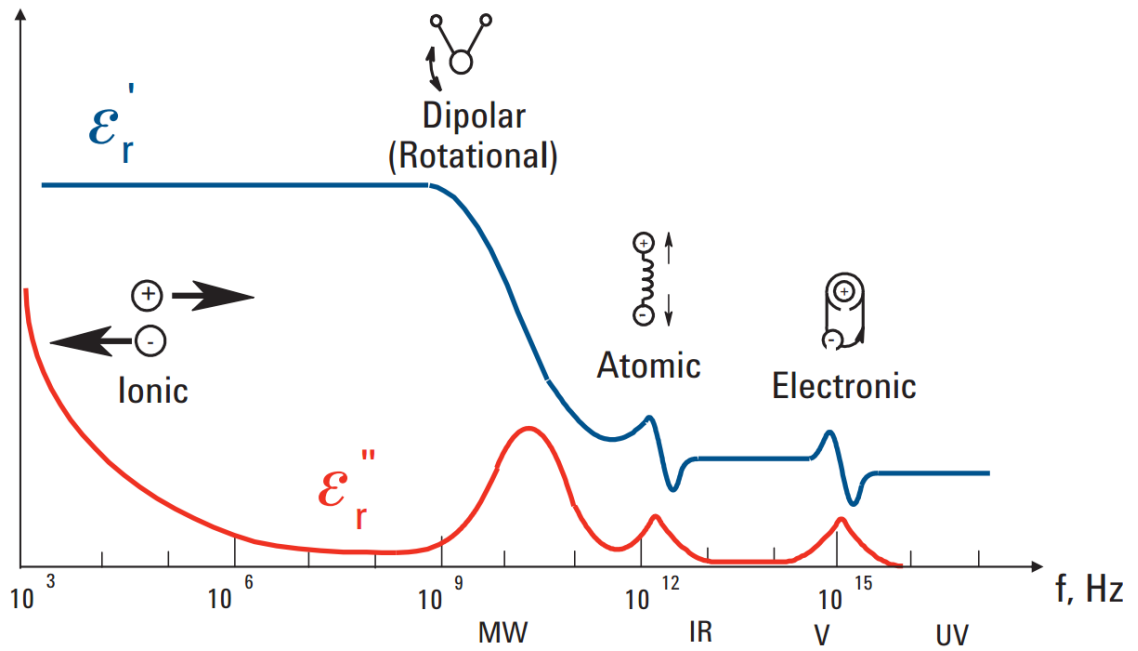


Figure 2.3 Frequency dependency of complex permittivity. Dielectric mechanisms including ionic polarization, dipolar polarization, atomic polarization and electronic polarization contribute to the dielectric relaxation behaviour (Agilent Technologies, 2014).

The Debye equation has been used to describe the frequency dependency of the complex permittivity (Debye, 1929):

$$\varepsilon^*(\omega) = \varepsilon_\infty + \frac{\varepsilon_s - \varepsilon_\infty}{1 + j\omega\tau} - j \frac{\sigma}{\omega\varepsilon_0} \quad (9)$$

The complex permittivity is a function of field frequency ω . ε_s is the static, low frequency permittivity and ε_∞ is the permittivity at the high frequency limit, as shown in Figure 2.4. σ is the conductivity of the media. τ is defined as relaxation time of the media.

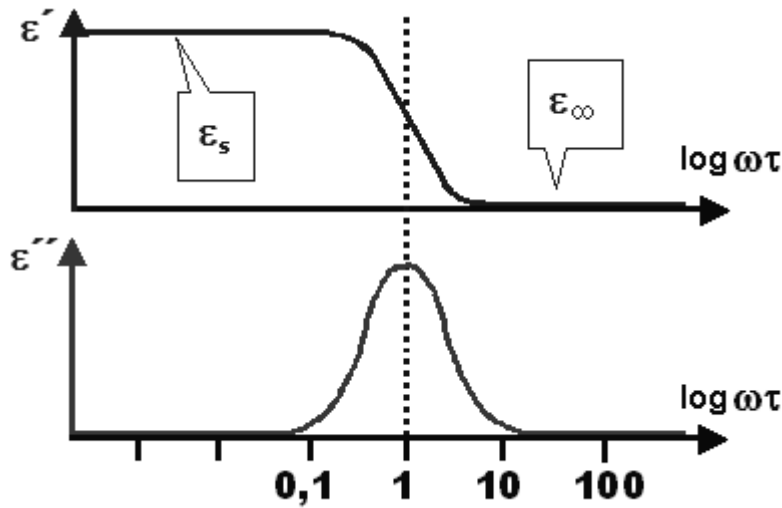


Figure 2.4 Debye-relaxation for some non-conductive material ("Dipole Relaxation," n. d.).

In sensing application implemented in petroleum production process, MUTs are often complicated emulsion of various dielectrics. The measured permittivity is therefore referred to as the effective permittivity ϵ_{eff} , as it represents the combined dielectric property of all dielectrics in the emulsion.

2.2 Using transmission lines for measurement of material properties

2.2.1 Transmission line

A transmission line is a closed system in which power is transmitted from a source to a destination. Since the size of the circuit is comparable to the wavelength of the electric signal, the voltage $[V]$ and the current $[I]$ of the signal on a transmission line is a function of both time and position. For a transverse electromagnetic wave (TEM) with an angular frequency ω propagating in the $+z$ direction through a transmission line filled with a dielectric material of permittivity ϵ^* , its voltage at time t and position z from the source is described as:

$$V(z, t) = V_0 e^{j\omega t - \gamma z} \quad (10)$$

where V_0 is the amplitude of the voltage at the source and γ is the propagation constant of the transmission line. The propagation constant γ is used for characterizing the properties of a certain transmission line. The propagation constant γ for TEM wave is:

$$\gamma = j \frac{\omega}{c} \sqrt{\epsilon^*} \quad (11)$$

where c is the speed of light in vacuum. The propagation constant is a complex quantity that can be generally represented as:

$$\gamma = \alpha + i\beta \quad (12)$$

where the real part α is called the attenuation constant and the imaginary part β is called the phase constant.

When encountering an impedance discontinuity in a transmission line, the travelling electromagnetic wave will be partially reflected and partially transmitted. Two coefficients: the reflection and the transmission coefficients are then defined to describe the property of transmission line by the reflected and transmitted waves. The reflection coefficient Γ is defined as:

$$\Gamma = \frac{V_r}{V_i} \quad (13)$$

where V_r represents the reflected voltage wave, and V_i represents the incident voltage wave. Similarly, the transmission coefficient T is defined as:

$$T = \frac{V_t}{V_i} \quad (14)$$

where V_t represents the transmitted voltage wave.

2.2.2 Scattering parameters

In an electrical network consisting of two ports, as shown in Figure 2.5, the input waves at port 1 and port 2 can be denoted as a_1 and a_2 , respectively, whereas the output waves from the two ports are denoted b_1 and b_2 .

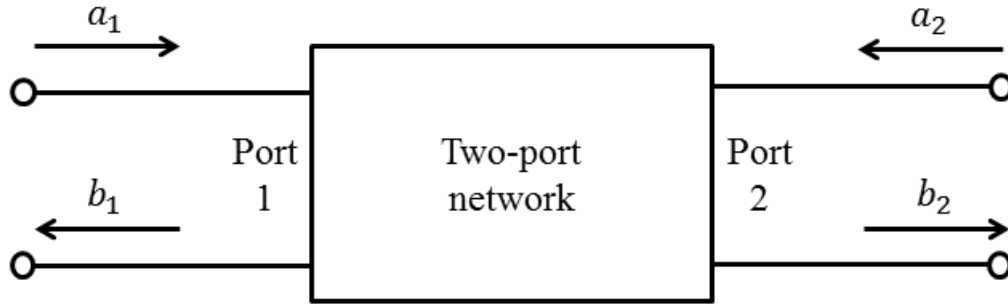


Figure 2.5 Schematic graph of a two-port network with incoming waves a_1 and a_2 and outgoing waves b_1 and b_2 .

The relationships between the input and output wave are often described by scattering parameters (S-parameters) given as:

$$[S] = \begin{bmatrix} S_{11} & S_{12} \\ S_{21} & S_{22} \end{bmatrix} \quad (15)$$

where $[S]$ is the scattering matrix consists of four scattering parameters in the form of S_{ij} where i stands for the port for output and j the port for input:

$$S_{ij} = \frac{b_i}{a_j} \quad (16)$$

Each of the S-parameters is calculated when only the respective port j is excited.

2.2.3 Dielectric spectroscopy

Dielectric spectroscopy is a method for measuring the dielectric properties of a medium as a function of frequency (Kremer & Schönhal, 2003). In the case where transmission lines are used to perform dielectric spectroscopy, the interpretation of the measured effective permittivity is calculated from the measured S-parameters.

If the MUT is non-magnetic material, and the wave propagating in the transmission line is in transverse electromagnetic (TEM) or quasi-TEM mode (Chen, 2004), the propagation constant γ can be represented as:

$$\gamma = j \frac{\omega}{c} \sqrt{\epsilon_{eff}^T} \quad (17)$$

where ε_{eff}^T represents the effective permittivity of the transmission line with the MUT. The propagation constant when there is no MUT, denoted as γ_0 , can be represented as:

$$\gamma_0 = j \frac{\omega}{c} \sqrt{\varepsilon_{eff0}^T} \quad (18)$$

where ε_{eff0}^T stands for the effective permittivity of the transmission line without the MUT. Thus, the reflection coefficient and transmission coefficient can be written respectively as (Chen, 2004):

$$\Gamma = \frac{\gamma_0 - \gamma}{\gamma_0 + \gamma} \quad (19)$$

$$T = e^{-\gamma L} \quad (20)$$

where L is the length of the transmission line with the MUT.

Measured S-parameters are used for deducing the transmission and reflection coefficients at the plane where the transmission line meets the impedance discontinuity caused by the MUT. Their relationship is given as (Nicolson & Ross, 1970):

$$S_{11} = S_{22} = \frac{\Gamma(1 - T^2)}{1 - \Gamma^2 T^2} \quad (21)$$

$$S_{21} = S_{12} = \frac{T(1 - \Gamma^2)}{1 - \Gamma^2 T^2} \quad (22)$$

Once calculated, the coefficients are used to calculate the propagation constant γ of the wave in the MUT according to equations (19) and (20). The effective permittivity ε_{eff} determines the propagation constant γ as in equation (17), and the permittivity of the MUT can therefore be calculated.

For the sensors used in this project, the S-parameters are measured at the two ports. Measurements are done via coaxial cable connected to a network analyser. However, the two ports are not where the transmission line meets the impedance difference at the boundary of the MUT. Therefore, there are two groups of S-parameters. It is convenient to call the S-parameters at the two ports the measured S-parameters S_{ij}^M and those at the boundary of the MUT the reference S-parameters S_{ij}^R . These two groups are different due to the impedance mismatch at the transition from the CPW to the coaxial cable. The measured S-parameters contain the information of the mismatch while the reference S-parameters only represent the interaction of the wave and the MUT.

In order to obtain the reference S-parameter, a transformation method is used (Folgerø, 1996):

$$S_{ij}^R = \frac{A_{ij}S_{ij}^M + B_{ij}}{C_{ij}S_{ij}^M + 1} \quad (23)$$

where A_{ij} , B_{ij} and C_{ij} can be determined by three reference measurements taken. The three reference measurements are performed using the same measurement instrument on three materials with known permittivity.

Furthermore, in order to avoid the use of an iterative method in calculating the permittivity from the reference S-parameters S_{ij}^R , the calculation process can be simplified by series expansion of the reflection coefficient T :

$$T = 1 - \gamma L + \frac{1}{2}(\gamma L)^2 - \frac{1}{4}(\gamma L)^3 + \dots \quad (24)$$

By ignoring the higher order elements (above two) and combining the equation with equation (23), a simplified relationship between measured S-parameters and the permittivity of the MUT can be established as (Folgerø, 1996):

$$\varepsilon^* = \frac{\widetilde{A}_{ij}S_{ij}^M + \widetilde{B}_{ij}}{\widetilde{C}_{ij}S_{ij}^M + 1} \quad (25)$$

where \widetilde{A}_{ij} , \widetilde{B}_{ij} and \widetilde{C}_{ij} can be determined by three reference measurements taken at similar conditions to those described for equation (23).

2.3 Coplanar waveguides

A waveguide is a structure that conveys electromagnetic waves between its endpoints. The design of the sensor presented in this paper is based on the concept of CPW, which is a type of waveguide that originates from the concept of planar transmission line. It is used to convey microwave frequency signals. The fundamental mode of propagation in the CPW is a quasi-TEM mode (Chen, 2004), which allows the permittivity to be interpreted, as explained in the later section 2.2.3. A normal CPW typically has the form as shown in Figure 2.6 below.

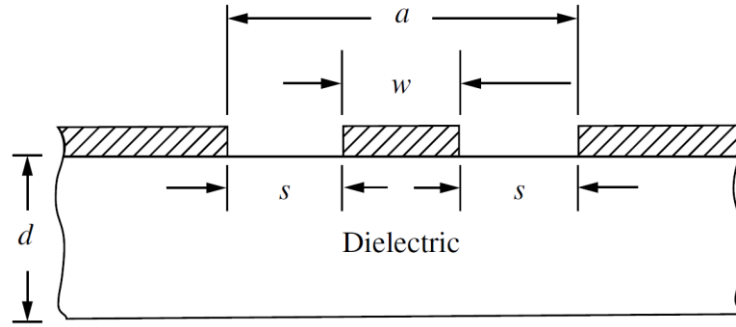


Figure 2.6 Structural dimensions of a CPW (Chen, 2004).

In a CPW, all the conductors for transmission of electromagnetic waves are located on the upper surface of a dielectric substrate. Consequently, the characteristics of a CPW can be controlled by the dimensions on a single plane: width of the central conductor w and the gap s between the central conductor and the side ground conductor. Therefore, the circuit fabrication can be conveniently carried out, which makes prototyping easy.

The material above the conductor (normally air), together with the dielectric substrate under the conductor, constitutes the insulator of the transmission line, as in a traditional coaxial cable. In the case where the thickness of the conductor strip is negligible, and the substrate is very thick, the effective permittivity of the CPW can be represented as:

$$\varepsilon_{eff}^T = \frac{\varepsilon_{sub} + \varepsilon_{eff}}{2} \quad (26)$$

where ε_{sub} is the permittivity of the material used for the substrate, and ε_{eff} is the effective permittivity of the substance above the conductor plane.

Previous experience has shown that CPW possesses some advantages over grounded coplanar waveguide (GCPW) when used for material characterization purposes (Haukalid, 2011). The most obvious disadvantage of GCPW is that the ground plane located closely under the dielectric substrate will change the even distribution of electric field above and under the conductor plane, and more field energy will be directed to the dielectric substrate. This leads to a reduction of electric field energy above the conductor plane. Therefore, equation (26) will no longer be valid. In using CPW for measurement of dielectric property, the transmission and reflection of the wave due to its interaction with the MUT is the actual measurement modality. If the MUT was placed above the waveguide, better electric field energy above the plain would

contribute to a more sensitive measurement result. Consequently, the sensitivity to the MUT of the GCPW will be reduced compared to that of the CPW.

By assuming that the thickness of the conductors are zero, grounded conductors are infinitely wide and the substrate has infinite thickness, approximate formulas (Ramo, Whinnery, & Van Duzer, 1994) can be used to determine the characteristic impedance of the CPW:

$$Z_c = \frac{\eta_0}{\pi \sqrt{\epsilon_{eff}^T}} \ln \left(2 \sqrt{\frac{a}{w}} \right) \quad (27)$$

when $0 < w/a < 0.173$, where $a = w + 2s$ as in Figure 2.6 and $\eta_0 = \sqrt{\frac{\mu_0}{\epsilon_0}}$ is the wave impedance of plane waves in free space:

$$Z_c = \frac{\pi \eta_0}{4 \sqrt{\epsilon_{eff}^T}} \left(\ln \left(2 \frac{1 + \sqrt{w/a}}{1 - \sqrt{w/a}} \right) \right)^{-1} \quad (28)$$

when $0.173 < w/a < 1$.

2.4 Natural gas hydrates

Natural gas is a subcategory of petroleum that is a naturally occurring complex of hydrocarbons with a minor amount of inorganic compounds (Guo & Ghalambor, 2012). It primarily consists of methane, together with varying amounts of other higher alkanes. Natural gas is an energy source often used for heating, cooking, electricity generation and as fuel for vehicles.

Natural gas hydrates (or clathrate hydrates) are crystalline solids composed of water and gas. The gas molecules (guests) are trapped in water cavities (host) that are composed of hydrogen-bonded water molecules. Typical natural gas molecules include methane, ethane, propane, and carbon dioxide (Sloan & Koh, 2008). A typical gas hydrate structure is shown in Figure 2.7.

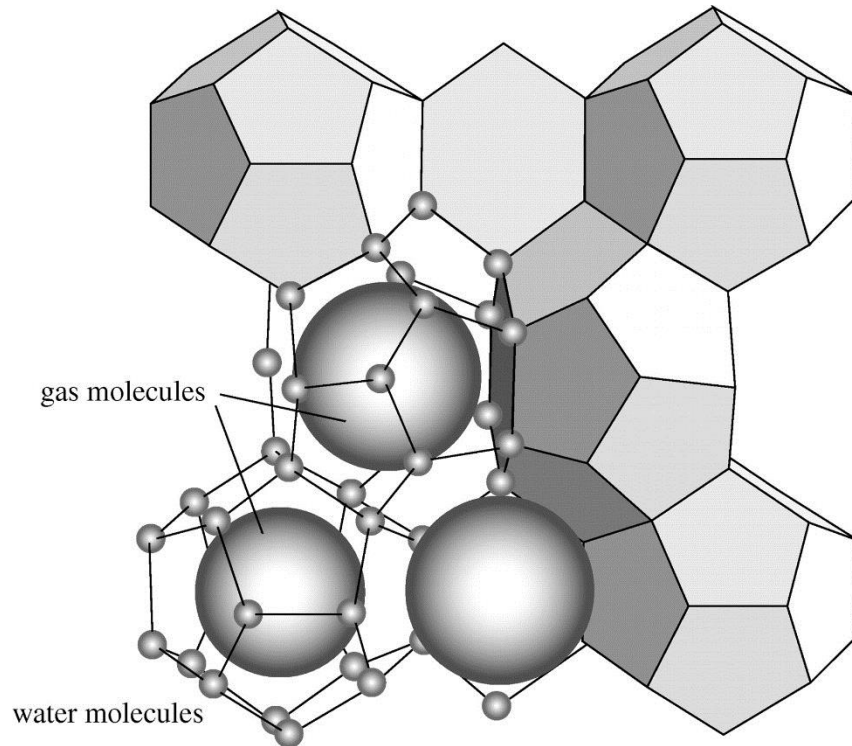


Figure 2.7 Typical structure of gas hydrate with water molecules linked together to form a cage trapping a gas molecule such as methane within (Maslin et al., 2010).

Gas hydrates can form ice-like structures in a petroleum pipeline during high pressure, low temperature conditions. It has been suggested that hydrates formed in condensate pipelines may deposit on the pipe wall, similar to a freezing water pipeline (Lingelem, Majeed, & Stange, 1994). Recent hydrate field studies conducted in both Wyoming (Hatton & Kruka, 2002) and the Norwegian Sea sector (Austvik, Hustvedt, Meland, Berge, & Lysne, 1995) suggest that hydrates may adhere to pipe walls. In both field tests, the observed pressure build-ups and fall-offs were consistent with hydrate deposits on the pipe wall before sloughing and moving downstream (Nicholas, Dieker, Sloan, & Koh, 2009). Once formed, hydrate plugs dislodged from the pipe wall can move downstream a flow line at high velocities together with the flowing substance under production. At locations where the pipeline bends, the hydrate plug can rupture the flow line through projectile impact (Sloan & Koh, 2008). Hydrate formation can also simply block pipelines or wellbores, preventing production and related operations.

The dielectric properties of gas hydrates differ from those of water. Dielectric relaxation due to dispersion of gas hydrates occurs around 100 kHz, while that of water occurs at GHz range. A dispersion caused by polarisation inside the conductive water droplets

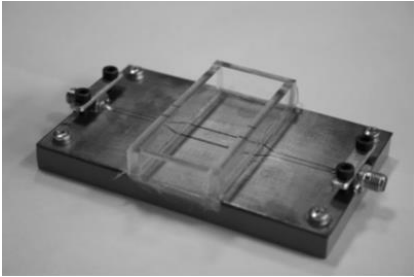
occurs at frequencies around 100 MHz. Hence, formation of gas hydrates in emulsions can be detected by permittivity measurement (Jakobsen & Folgerø, 1997).


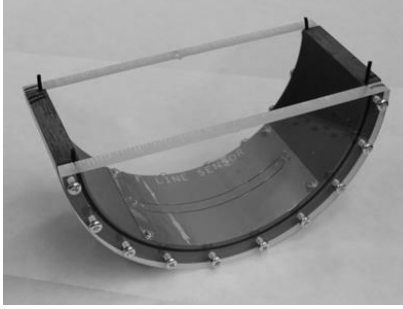
3 SENSOR DESIGN AND SIMULATIONS

In this chapter, the details of the two CPW sensor designs are presented with subsequent sensor simulations. The structures of the two sensors are explained including their models in simulation tool. Following, the simulations performed on the prototypes are presented. Finally, the simulations of both uniform and non-uniform liquid layers on one of the sensors are presented.

Three sensors are investigated in total, as listed in the table below. Sensor A is constructed in a previous research project, whereas sensor B and C are designed and constructed in this project. A single design of flexible-PCB-based CPW is performed in this project. Sensor B and C use the same CPW design, but are constructed differently in geometries.

Table 3.1 Overview of the sensors used in this project

Name	Brief description	Photograph
Sensor A	Small container over CPW with edge-mounted SMA connector.	

Sensor B	Large cuboid chamber above the entire surface of the CPW with a vertical-mounted SMA connector. The design is intended to test the viability of vertical through-hole non-intrusive connection between the connectors and the CPW, as well as the viability of measuring MUT above the entire surface.	
Sensor C	Large chamber in partial cylindrical form above the surface of the CPW. Intended to test the performance of the flexible PCB and the possibility of mounting on inside of pipeline.	

Sensor B and C are described in detail in chapter 3.6.

3.1 Design of the coplanar waveguide

As explained in the previous chapter, it is more practical to incorporate an ungrounded CPW for the sensor design. In this project, only CPW based sensors are therefore investigated. The sensor design has been based on the following two main guidelines:

- i. The design options that are most practical, available and economically viable are prioritized. The reason behind guideline i is the relative short time span of the project. The goal of the project is to construct and examine a prototype in limited time. Therefore, the focus of the project has not been placed on complete optimization of the design.
- ii. The design options that fit for implementation in industrial conditions are favourable. The reason behind guideline ii is the interest relating to testing the industrial applicability of the sensor. When such options are adopted in the design of the prototype, their feasibilities can be evaluated.

3.1.1 Coplanar lines on PCB

The new CPW for sensor B and C adopts similar cross-sectional dimensions used in the CPW of sensor A. However, the new CPW differ from the old CPW primarily in that

the sensing area is much longer. In addition, the new CPW is designed for vertical transition instead of the horizontal transition used in the old CPW. The new CPW is constructed on flexible PCB while the old one is on traditional PCB.

The cross-sectional dimensions of the CPW used in sensor A are partially adopted into the design of sensor B and C. This follows the guidelines i mentioned earlier.

There are three reasons for adopting a the CPW design of sensor A to sensor B and C. Firstly, the design of sensor A is based on previous work done on permittivity sensitivity and thickness sensitivity (Haukalid, 2011). The design of sensor A has been proven to possess improved sensing functions for wave signals within the frequency range of 10 MHz to 10 GHz. The same frequency range is used in this project as well. The reason is that most of the significant dielectric relaxation phenomenon happens within or close to this frequency range, and because the frequency range is limited by the simulation bottleneck of the software. It is therefore practical to adopt a similar design. Secondly, further optimization on sensor dimensions is not pursued since the optimization is frequency dependent. Optimizing the design will cause the sensor to function better inside a narrow frequency range but will lose sensitivity at frequencies outside that range. Since the project goal is to perform a generic feasibility study on the sensor design, a wider working frequency range is more favourable since it allows for broader analysis. Thirdly, a similar design provides the opportunity to compare measurement results between the old and the new sensors.

Figure 3.1 below shows a layout of the CPW as seen from above.

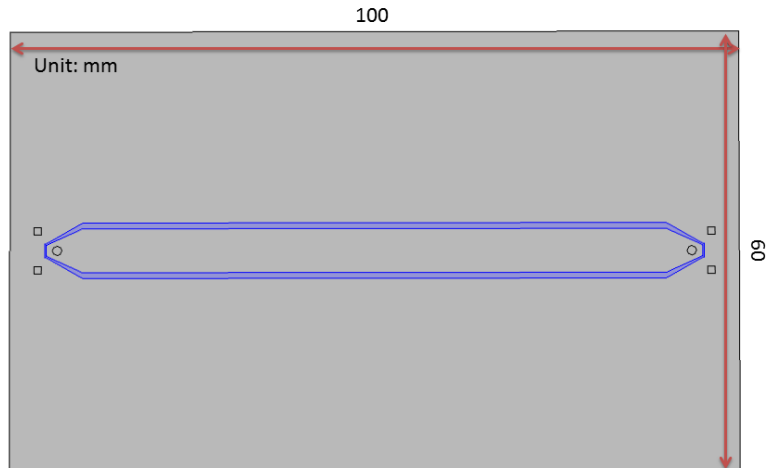


Figure 3.1 Geometry of the coplanar line.

Flexible printed circuit boards are used for the CPW layout, which is in accordance with guideline ii. Using such a material, the sensor can easily fit onto curved structures, for example a pipeline wall. Flexible printed circuit boards, known also as flex circuit boards, represent a technology for assembling electronic circuits by mounting electronic devices on flexible plastic substrates. While they offer the same advantages as that of a rigid printed circuit board, including repeatability and reliability, their most important advantage is the capability to assume three-dimensional configurations (Khandpur, 2006). The metallic clothing over the gap path (dark blue in Figure 3.1) is scraped off, such that the substrate of the PCB is exposed to MUT.

Dimensions consider manufacturing are shown in Figure 3.2. Two square and one circle holes are left hollow for the legs of coaxial connectors, such that the vertical transition can be mounted.

MUT close to the pipe wall. Therefore, a sensor built in this manner would be helpful to examine the feasibility of the design.

In previous research, a part of the transmission line has been left outside of the MUT to better characterize the interaction between the wave and MUT at the boundary between the transmission line and the MUT (Haukalid, 2011). As described previously, no part of the transmission line is left outside the MUT in the two new designs presented in this work. A comparison between sensor A and the two new sensors B and C is already shown in Table 3.1. In the sensor B and C, the wave goes through a coaxial connector and makes contact with the MUT at the exact same location as it enters CPW on the plane from coaxial waveguide.

The designed CPW layout was manufactured by the “ITEAD” in China. The photograph of the designed and produced flex circuit board is shown in Figure 3.3.

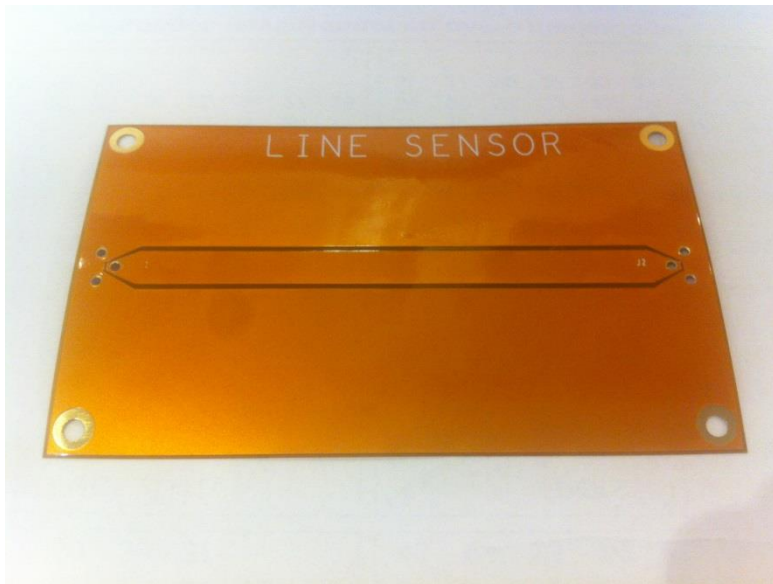


Figure 3.3 Photograph of the CPW produced on flexible PCB.

As shown in the figure, the CPW is manufactured on a 1-layer flexible printed circuit board. The surface is copper. The substrate for flexible circuit is polyimide, which has a dielectric constant of 3.4 at 1 kHz. Other relevant specification details are listed in Table 6.1 in Appendix. According to the manufacturer, the product has good bending characteristics, which is vital for construction of sensor C. Therefore, the sensors built in this project are considered stable under repeated bending, meaning it is not susceptible to significant change in the physical properties due to deformation, which in case would lead to signal distortion. Nevertheless, attentions are paid on the possible

influence of bending during the experiments. The bending characteristics are examined in chapter 4.

3.1.2 Transition between coaxial and coplanar waveguides

Coaxial connectors are used as transition media from the CPW to the coaxial cables in order to enable network analyser excitations and measurements. Vertical mounting of the coaxial connectors has been chosen instead of the previously used edge-mounting of coaxial connectors (Haukalid, 2011). An illustration of the vertical mounting of the coaxial connectors on the CPW sensor is shown in Figure 3.4. The reason for selecting vertical mounting design is that such a design will have practical benefits in an industrial measurement setup. As explained in the example in the previous section, it would not be practical to have the coaxial connection on the same plane as the CPW, since they would otherwise be in contact with the MUT as well, which would affect the measurement and impose intrusiveness in a pipeline containing flowing substances. In addition, the vertical-mounted transition introduced here is also aimed for further testing the influence of through-hole transitions on measurement of dielectrics. The transition from coaxial cable to CPW on sensor A is conducted on the same plane. This is beneficial since the characterization of the transition and the measurement itself become separate. The aim of this work is to test the setup one-step further using a more practical transition and studying its influence on the measurement. In all, the necessity of a vertical through-hole transition in industrial applications of the sensor governs its implementation and testing in this project.

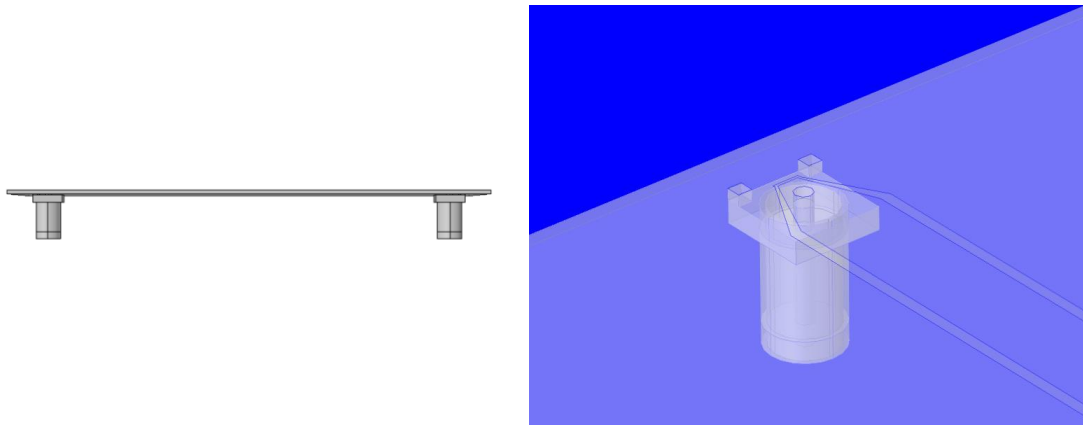


Figure 3.4 Vertical-mounted SMA connector as transition from the coaxial cable to the CPW.

There are various techniques used to perform the through-hole vertical-mounted transition. In consideration of guideline number i, a new method for the through-hole transition is however not developed in this project. The transition technique used is in accordance with existing practices (Holzman, 2006) although with some alteration.

Furthermore, the design is based on the available model of fitting coaxial connector. In order to match the dimension of the coplanar transmission line, SMA (SubMiniature version A) connectors with straight PCB jacks (female) from Huber & Suhner are used in all sensors in this project. Its detailed specification is available in Figure 6.1 in Appendix.

In order to mount the coaxial connector vertically on the CPW, the dimensions of the coplanar line at each end has to be altered. The dimension at the end of the CPW needs to fit with the dimension of the SMA connector for a proper soldering connection to be established. According to equation (28), the characteristic impedance of the coplanar line on the CPW will not change if the ratio between the width of central conductor and that of the gap is maintained. Therefore, a taper with equal ratio is designed at both ends as shown in Figure 3.5.

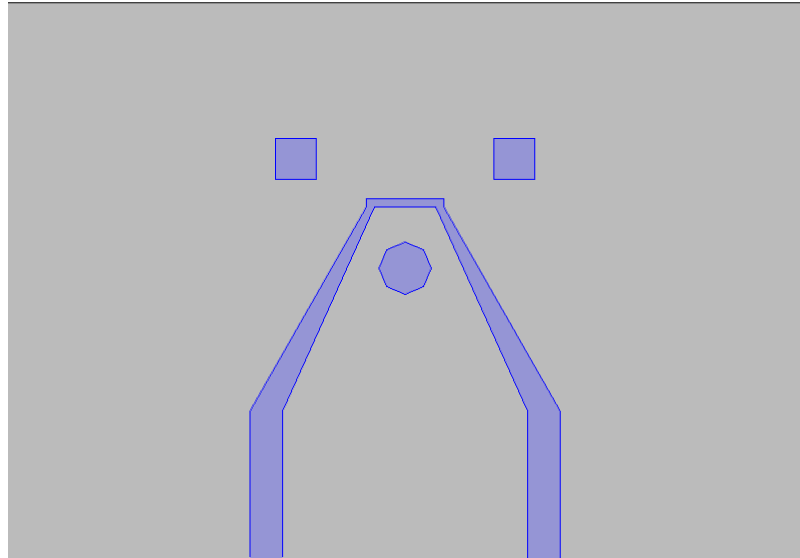


Figure 3.5 Design detail of CPW near the transition area for the coaxial connector.

The ratios are kept unchanged while the dimension of the lines shrinks towards the centre, forming an isosceles trapezoid structure. Subsequently, the centre conductor of the SMA connector connects with the centre conductor of the coplanar line, and two of the outer conductor legs of the SMA connector make contact with the ground conductor of the coplanar line. Due to geometrical limitation, the other two legs are cut. The taper transition will need to be prolonged to fit the other two legs, which will cause a shortening of the centre part of the coplanar line. The aim of this is to keep the transition in a confined area for an easier characterization of the CPW geometry where the transition area is small and sensing length is long. The design of the sensor is quite different compared to the typical use of transmission lines when measuring dielectric properties of a material. Usually, the measurement area including the MUT and other connecting parts of the transmission line, are on the same plane. However, the sensors in this project have a 90-degree transition between the coaxial and the CPW. Thus, an abrupt impedance mismatch caused by the vertical-mounted coaxial connectors is to be expected. As the aim of the project is to evaluate the measurement performance by building and testing prototype sensors, it would serve the purpose better if the impedance mismatch was left unmodified such that its effect would be analysed from the measurements. Consequently, a detailed optimization analysis of the transition is not performed in the project. The transition is designed to be dimensionally as small as possible to minimize this effect.

Moreover, the SMA connector has a characteristic impedance of 50Ω , whereas the characteristic impedance of the coplanar line is 66Ω . Traditionally, impedance transformation is done at such transition to reduce reflections at the interface. In the case of this project, the impedance of the CPW is not well defined at the location of the vertical-mounted transition due to the abrupt impedance change as mentioned above. An impedance transformation will further complicate the electrical properties at the transition. Further impedance transformation is therefore not implemented in order to achieve a simpler model for further analysis.

3.2 Modelling of sensor A

A model of sensor A was established first. The intention was to conduct simulations on this model, and compare the simulation results with measurements done on the “old” sensor, i.e. sensor A. This is to verify that the simulation software will produce realistic results for radio frequency physics models. Additionally, knowledge on configuration of the simulation is gained and used in further modelling and simulation process on other models. The sensor and its model are shown in Figure 3.6.

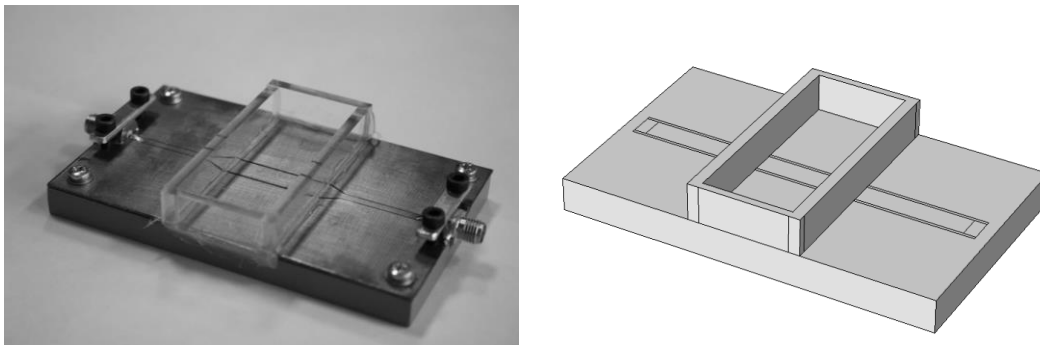


Figure 3.6 Sensor A (Haukalid, 2011) and its model in COMSOL Multiphysics.

Due to the scope of the project, simplifications are made when defining the simulation model. The purpose of the simulation model is to perform testing. Therefore, time was not spent on making a very exact simulation model of the sensor. Three main simplifications are included in the simulation model, as follows.

Firstly, the transition from coaxial to CPW is simplified in the simulation model, as shown in Figure 3.7. The SMA connectors are not implemented in the simulation model. Excitation bridges are however built on both sides of the sensor to achieve similar simulation effect. This is a recognized way of exciting CPW model in COMSOL (Frei, 2013). The side conductor planes are extended to surround the centre conductor

strip, and an additional rectangle (in blue) is introduced for the lumped port, mimicking the function served by the coaxial connector, which provides the excitation signals from the transmission line with a characteristic impedance of 50Ω .

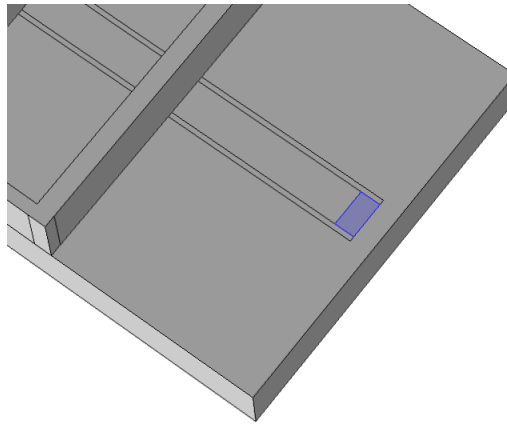


Figure 3.7 The excitation port of the modelled sensor.

Secondly, the taper transformation of the CPW on the original sensor, i.e. the transformation that aims for dimensional change while keeping the characteristic impedance, is neglected, as can be seen in Figure 3.8. Since the coaxial excitation is replaced by excitation bridges in the simulation model, the CPW dimension no longer needs to be designed to fit the transition to the coaxial connector. The bridge is designed to have the same width as the coplanar lines, and the transformation is therefore no longer required.

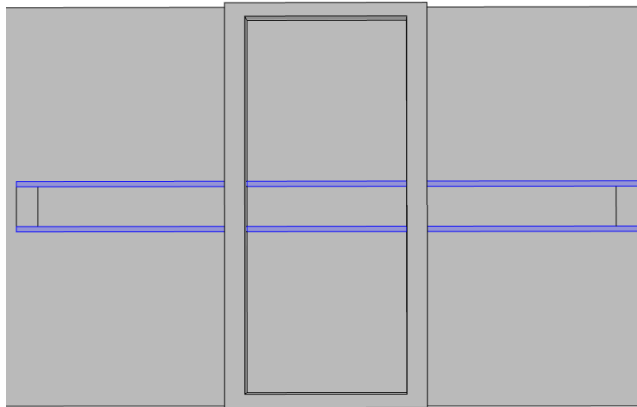


Figure 3.8 The coplanar line structure of the modelled sensor.

Thirdly, the surface conductor material of the CPW is modelled as a perfect electrical conductor instead of using the copper conductor of the original sensor design. Finite element method makes it hard to simulate conductors as layer with a very small but finite thickness. Such design cases require extremely detailed meshes, leading to very high demands on computational resources, including very long simulation processes. Therefore, the conductor is modelled as an infinitely thin surface. Since an infinitely thin surface cannot be made of certain materials, the surface conductors of the CPW are assigned in the model to be perfect electrical conductors.

The container for MUT in the centre of the CPW is modelled exactly. For different experiments, different materials are defined inside the area of the container. The side parts of the sensor make contact with air above the CPW at all times, and the excitation is made on one of the ports. The wave then makes contact with the MUT in the container in the middle of the sensor, transmitted and reflected. Results in the form of S-parameters are collected using simulation probes in the software.

3.3 Simulations on sensor A

The simulations conducted on the model of sensor A are presented here.

3.3.1 Software modelling and simulation

Modelling of the sensors has been conducted using the COMSOL Multiphysics software tool. The models was constructed using the built-in CAD module. Two models

are presented here: the model of the “old” sensor A (Haukalid, 2011) and the model of sensor B. Due to software limitations, the structure of the curved surface CPW, i.e. sensor C, is not modelled using the COMSOL Multiphysics software.

COMSOL Multiphysics version 4.4 was used, and the RF (radio frequency) module was used during the modelling and simulation work in the project. COMSOL Multiphysics is a finite-element analysis and solver software capable of various physics and engineering tasks. Through the CAD module, the geometry of a model is established. Subsequently materials are assigned to the different parts of the model. Simulation boundaries are set afterwards for the model, during which simulation probes, which are similar to probes of network analyser are also configured. Such probes can provide RF excitation and act like signal receivers. Before a simulation can be executed, the mesh quality has to be configured for the FEM iterative solver. Finally, the simulation is performed for a certain frequency range.

3.3.2 Preliminary testing

Firstly, a convergence test is conducted with regard to different intrinsic setups in the software for different qualities of mesh configurations. As for the FEM simulation, a proper and accurate simulation relies on the quality of the simulation mesh. Therefore, such convergence test provides information on how simulation data deviates with regard to mesh setup of different resolutions. Manual configuration of mesh resolution is not performed in the project due to the limited time. The simulations are merely used in the project to assist the sensor design, and to conduct otherwise difficult experiments if the validity of the software simulation tool is verified.

The test is conducted using air as MUT in the frequency range from 10 MHz to 10 GHz. 100 measurement points were taken for each simulation mesh setup ranging from ‘Coarse’ to ‘Extremely fine’, which are all built-in functionalities in the software. The results of the simulation using different simulation mesh resolutions are shown in Figure 3.9.

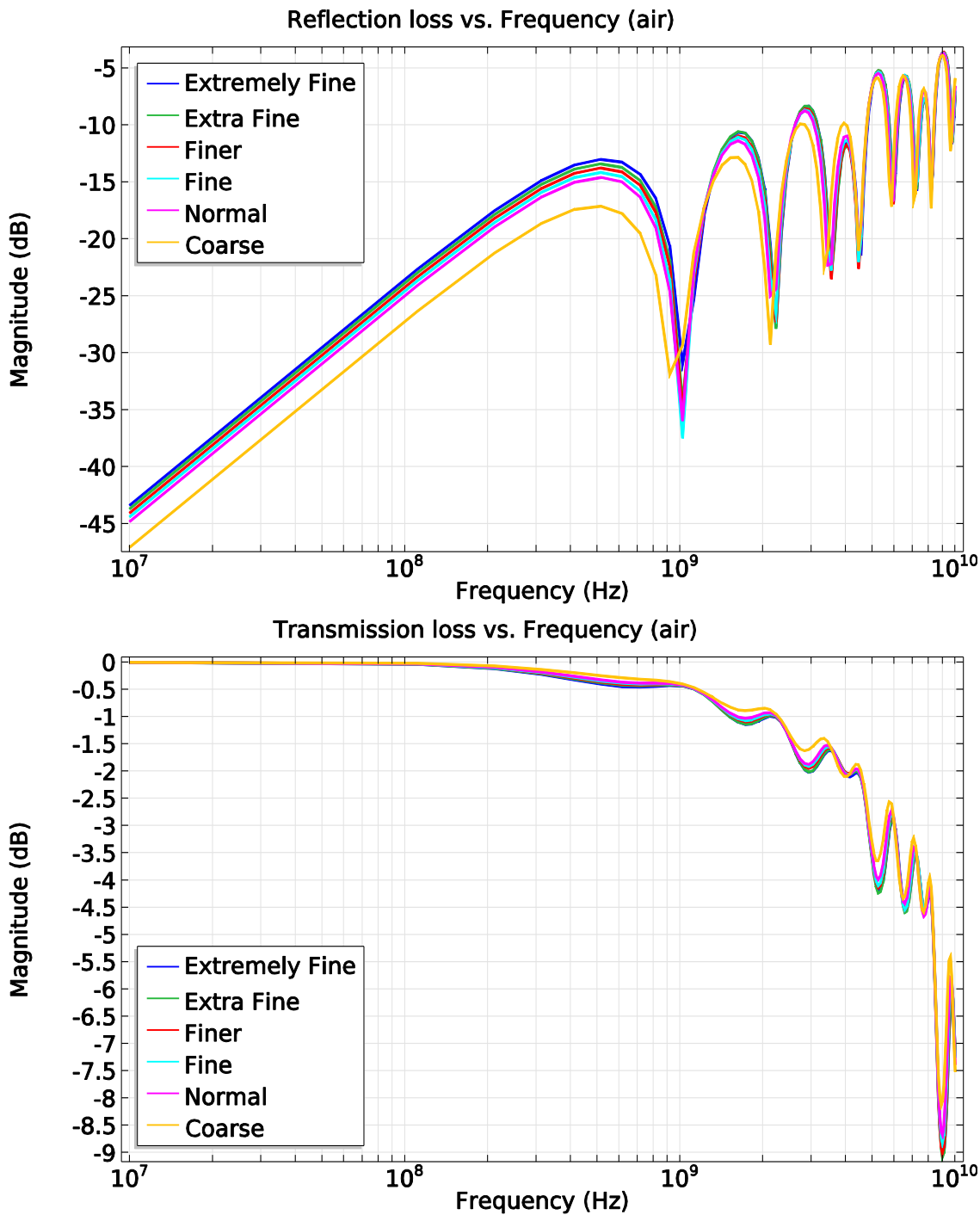


Figure 3.9 Convergence test of simulation as a function of different mesh resolutions. The reflection and transmission loss are plotted against frequency, for sensor A using air as MUT.

As can be seen, the peaks and valleys in the frequency response converge as the resolution of meshes is improved. For mesh qualities better than ‘Coarse’, simulation results are within an acceptable range of differences that is approximately 1 dB. All these mesh resolutions investigated give close simulation results compared to that of the

highest mesh quality, i.e. ‘Extremely fine’. Therefore, all the investigated mesh resolutions are considered as valid approximations in this project. Nevertheless, a mesh resolution better than ‘Normal’ has been chosen for the simulations, as long as the simulation duration is reasonable.

A different challenge is encountered when performing simulations with water as MUT, as the simulation will not converge for frequencies approaching 10 GHz. This might be due to the high relative permittivity of water. Such large dielectric constant makes the wavelength of water extremely small at high frequencies. A rule of thumb for maximum mesh element size is about one fifth of the wavelength. Therefore, a finer mesh is required in order for the simulation model to converge with water as MUT at higher frequencies. The ‘Extremely fine’ mesh configuration is the best mesh quality offered by the software. Manual setting to improve the mesh quality even further has failed due to limited computer memory. Using the current mesh configuration, the simulation converges approximately at 5 GHz. Higher frequencies requires a higher mesh resolution which requires more computational resources. Therefore, in this work, the simulations using water are conducted at frequencies between 10 MHz and 5 GHz.

3.3.3 Simulation configuration

Air and water are used as MUT during the simulations. The mesh is configured to ‘Extra fine’ for air, and 100 measurements are taken evenly in the range 10 MHz to 10 GHz. The mesh is configured to ‘Extremely fine’ for water, and 100 measurements are taken evenly in the range 10 MHz to 5 GHz.

3.3.4 Results

The simulation results in the form of S-parameters, including both magnitude and phase are shown in Figure 3.10 and Figure 3.11, with air and water as MUT respectively.

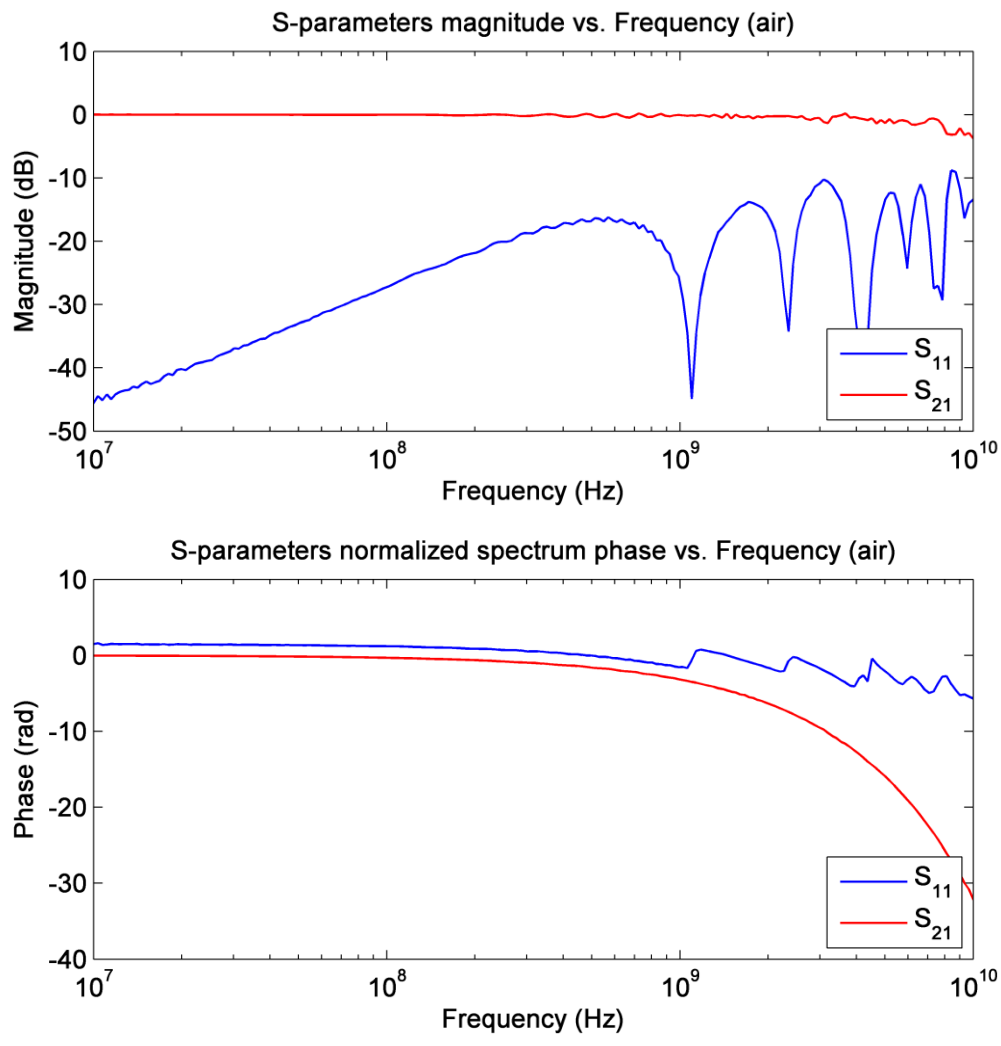


Figure 3.10 The simulated frequency response of magnitude and phase of S-parameters on sensor A with air as MUT.

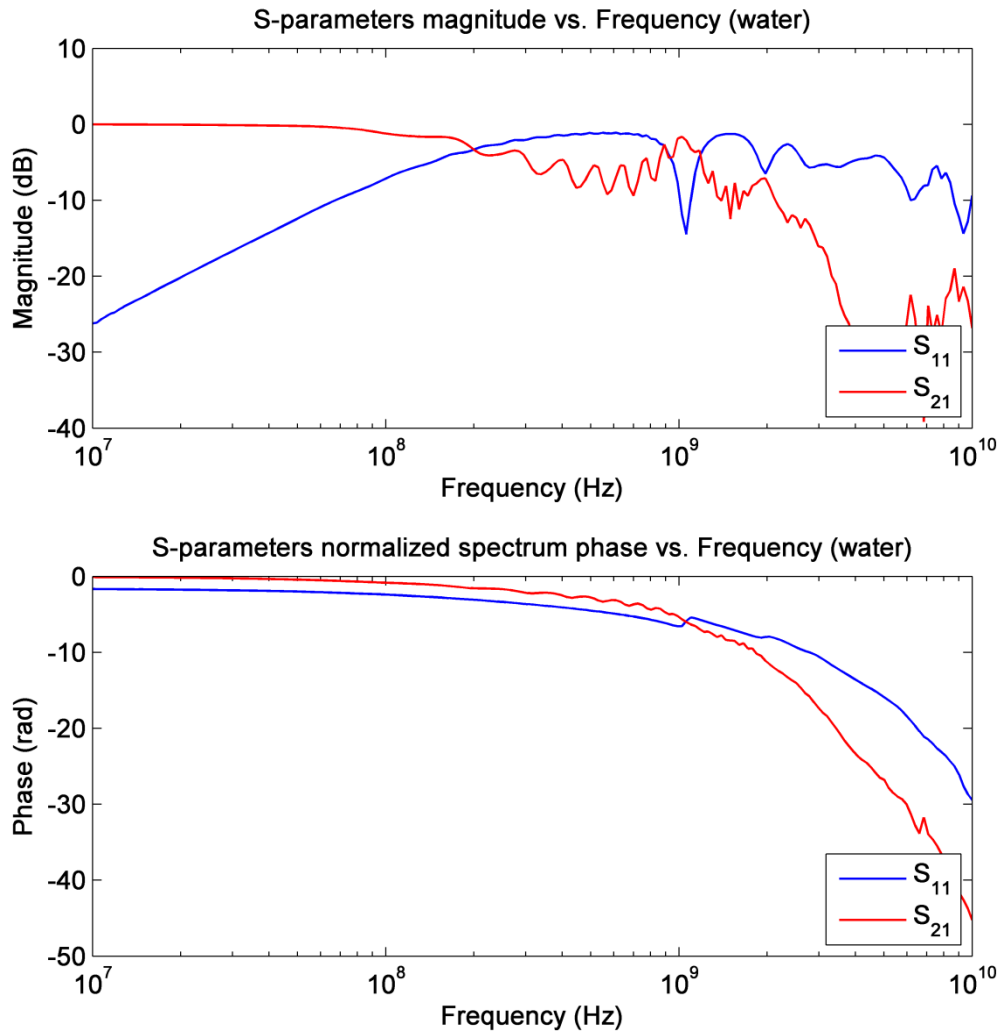


Figure 3.11 The simulated frequency response of magnitude and phase of S-parameters on sensor A with water as MUT.

3.3.5 Verification of simulation

The experiments on sensor A were repeated at the beginning of the project. Two groups of measurements were conducted using air and water as MUT, respectively, and subsequently compared to the simulation results. This comparison was done prior to the modelling of new sensors to verify that the simulation software was producing realistic results for the CPW sensor setup. Although the results are presented in this chapter of the thesis, details on the experimental setup and procedures are presented in the next chapter.

The S-parameters S_{11} and S_{21} are compared for both water and air as MUT. When only port 1 is excited, the magnitude of S_{11} and S_{21} can be interpreted as the reflection loss

and the transmission loss, respectively. The comparison for air is shown in Figure 3.12 below.

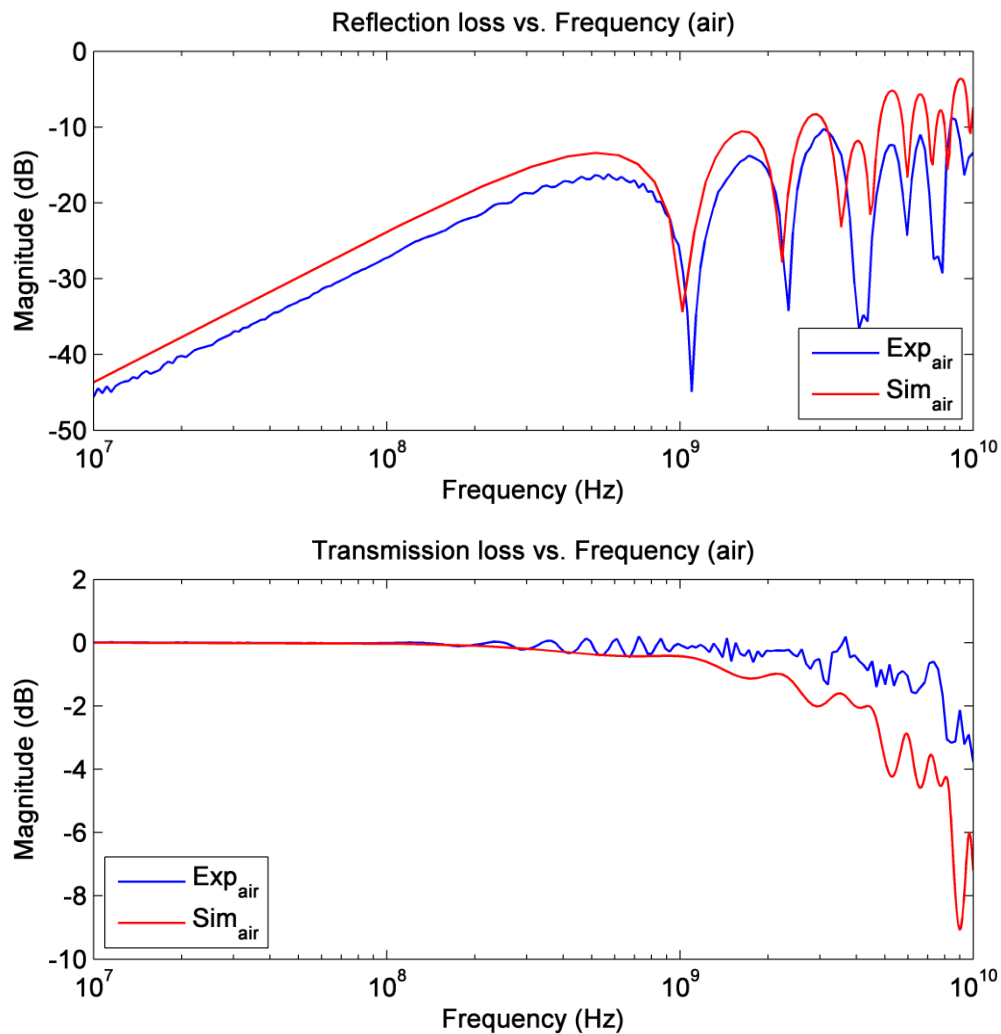


Figure 3.12 The reflection and transmission loss on sensor A with air as MUT. The simulation result is verified against the experimental result.

As observed, the simulation and experimental results match with each other quite well. Compared to the simulation results, there are additional ripples in the experimental data. Such slight differences between the simulation and experimental results are expected. The difference in ripples is because a simplified simulation model is implemented. Compared to the simplification of the simulation, the physical CPW sensor system includes the coaxial transition, the taper continuity and coaxial cables during the experiments. They all contribute to impedance mismatch in the measurement system. The impedance mismatch in the measurement system causes undesired reflections, which in turn leads to the differences observed in the ripples when comparing the simulated results to the experimental ones.

Similarly, the comparison for water is shown in Figure 3.13 below.

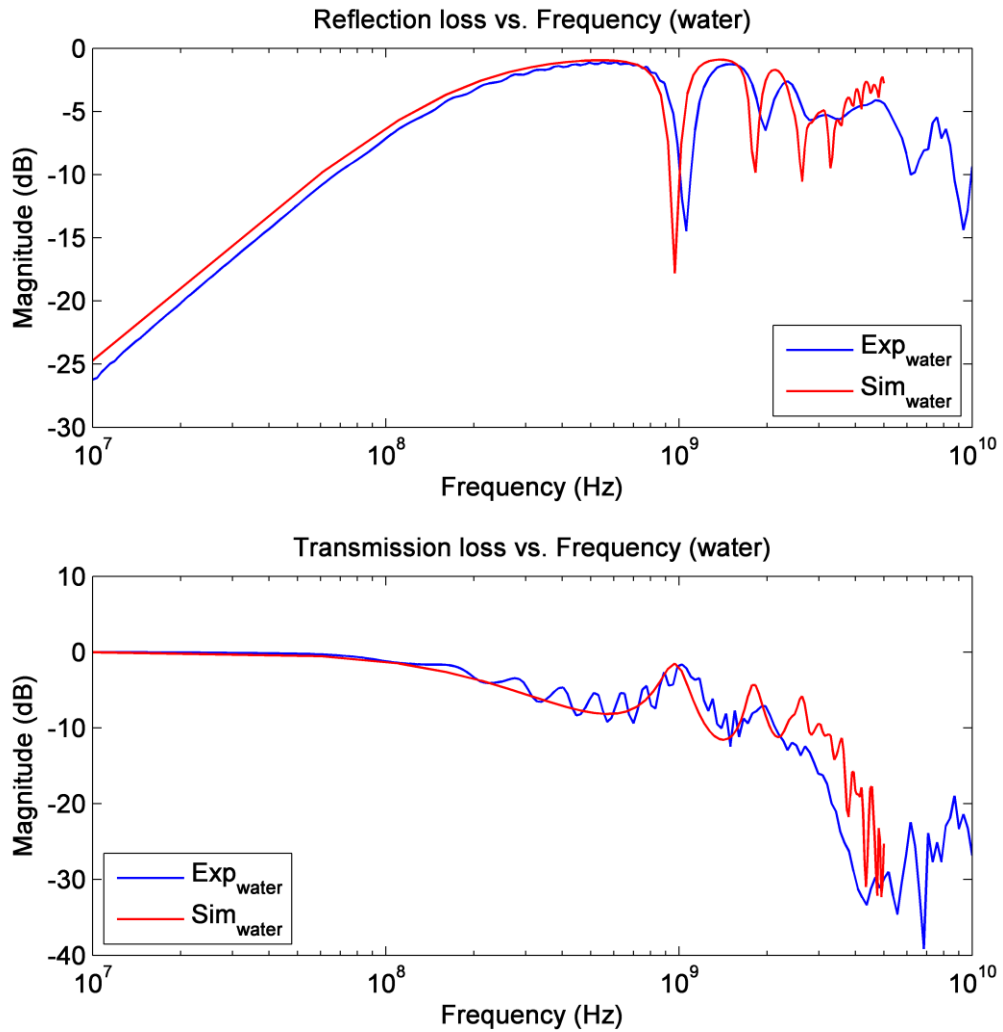


Figure 3.13 The reflection and transmission loss on sensor A with water as MUT. The simulation result is verified against the experiment result.

The simulation results using water shows close resemblance to the experimental measurement results as well.

In short, the simplified model produces simulation results that fit well with the actual experimental measurements. The permittivity of MUTs used in this project is inside the permittivity range between air (1) and water (~80). Therefore, the relatively good fit observed for both MUTs supports the confidence on using the software to simulate MUT with a permittivity between that of air and water. COMSOL is therefore used when designing sensor B and C in the project.

3.4 Modelling of Sensor B

The simulation model of sensor B was programmed prior to the manufacturing of the sensor. The purpose is to have an easily modifiable model available to assist during the design and development of the sensor. Different simulations are conducted to compare different sensor design of the sensor in order to find a reasonable design for the scope of the project.

The model of sensor B is quite similar to the actual design of sensor B. The only difference is that the wall of the container is omitted from the simulation model for simplicity, as shown in Figure 3.14.

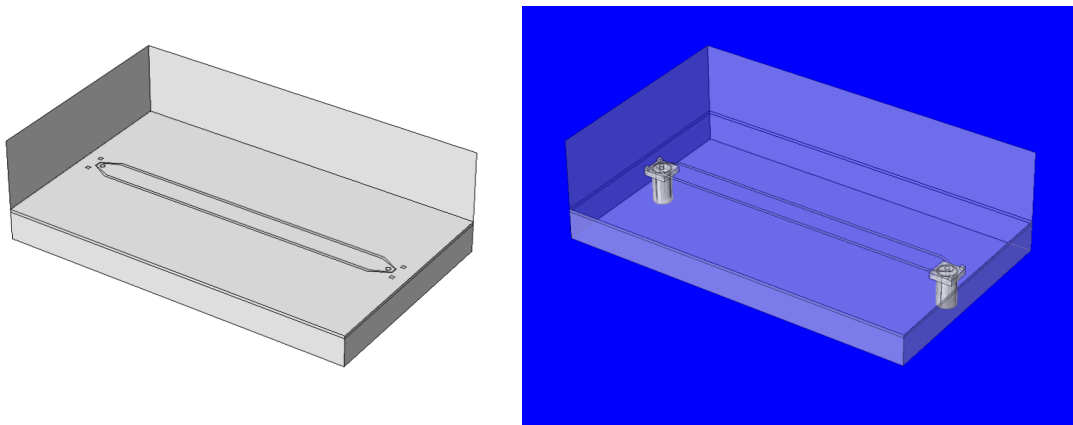


Figure 3.14 The model of sensor B using a solid view on the left and a transparent view on the right.

Similar to the model of sensor A, the CPW is modelled as an infinitely thin layer made of perfect electrical conductor. The CPW is placed on a thick layer of PVC as the substrate. The SMA connectors are made of gold, and they penetrate through the substrate, while the centre insulator of the SMA is made of Teflon. The simulation model replicates their geometrical and material details of the sensor as much as possible. Both connectors are used as excitation and receiving ports in the simulation. The central leg, i.e. the inner conductor, makes contact with the centre conductor of the CPW, while two other out legs make contact with the side conductor of CPW. The part of the legs that penetrate over the plane of the CPW, together with possible soldering compounds and geometries, are omitted from the model. This leaves the space above the CPW to be an absolute cuboid without intrusive geometry, which can be configured into different materials to perform simulations on the sensor. The scattering boundaries are set to be the outer surface of the bigger cuboid with the exception of the outer side of the SMA connector. This is reasonable since both the substrate and the area above the

CPW are thick enough to be similar to infinite depth with regard to the dimension and the sensing ability of the CPW.

3.5 Simulations on sensor B

The purpose for simulations on sensor B was to compare the simulations with the experimental measurements conducted on sensor B. Proven validity of the software in producing realistic simulation results allows further simulations to improve the study on non-uniform layers. It is generally easier to establish non-uniform layers of liquid in simulation than in a real experimental environment, since the confinement for liquids with non-uniform thickness will need to be reconstructed for each different configuration in the real experiments.

3.5.1 Simulation configuration

Air, water, methanol and ethanol are used as MUTs in the simulations. The mesh is configured to 'Finer' for air, and 100 measurements are taken evenly between 10 MHz and 10 GHz. The mesh is configured to 'Extra fine' for methanol, ethanol and water, and 100 measurements are taken evenly between 10 MHz and 5 GHz for each of these. The difference in mesh quality is shown in Figure 3.15 and Figure 3.16.

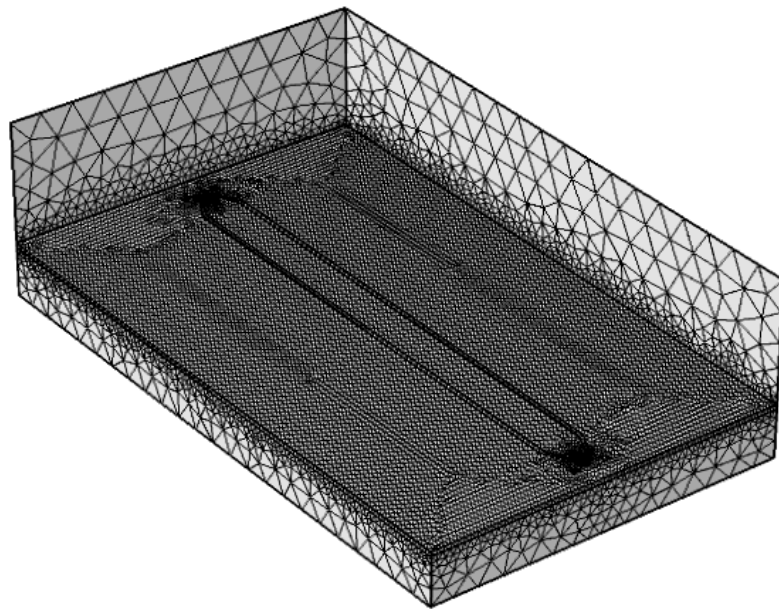


Figure 3.15 'Finer' mesh configuration used for sensor B.

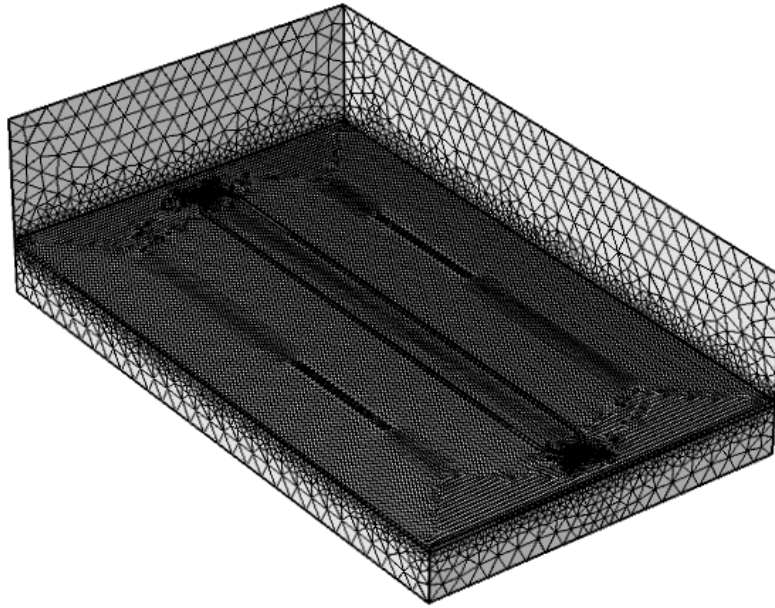


Figure 3.16 ‘Extra fine’ mesh configuration used for sensor B.

The difference in the mesh configuration between the simulations performed on sensor A and those performed on sensor B, is due to the increased complexity of the simulation model of sensor B. Sensor B is one of the two sensors developed in this project, and it is desired that the simulations are performed on the model as accurately as possible. This requires the simulation model to be as similar as possible to the actual sensor design. On the other hand, the more realistic the model is, the more geometrical details it needs to contain. The mesh configuration tool in the simulation software automatically generates a mesh configuration by a certain algorithm. In fact, the mesh will have a higher resolution at boundaries where geometry of the model changes. This implies that the more details the model contain, the more complex the mesh structure will be for the same mesh configuration setup in the simulation software. Thorough testing using the simulation software leads to the conclusion that the ‘Extremely fine’ mesh configuration is no longer a viable option. Because this mesh configuration generates a mesh map that requires a memory the size of which the computer cannot handle. On the other hand, the ‘Extra fine’ mesh configuration, which has one-step lower mesh quality than that of ‘Extremely fine’, does not have a small enough mesh resolution to simulate water as MUT even up to 5 GHz.

In such situations, a compromise needs to be made on the model. Multiple testing has proven that, the simulation bottleneck for the MUT with high dielectric constant reduces as all surfaces of the SMA connectors to be modelled as perfect electrical conductor.

This means that while the material of the SMA is modelled as gold, all the physical boundaries of the SMA connector, whether it is inner or outer as long as it separates different material, has to be modelled as a surface consisting of a perfect electrical conductor. Consequently, it is possible to simulate water as MUT at frequencies up to 5 GHz using an ‘Extra fine’ mesh configuration. The reason that the simulation result is easier to compute is possibly the fact that such a configuration of the surface, i.e. as a perfect electrical conductor, reduces the demands on mesh resolution close to the boundary between the materials. Obviously, the transition between the CPW and the SMA connectors and the SMA connectors themselves constitutes the most complex part of the simulation model. The simplification assuming that all the surfaces of the SMA connectors are perfect electrical conductor may have made it easier for the computer to run the simulation iterations, since the surface of CPW is modelled as perfect electrical conductor as well. Such a configuration may have reduced the need for a high quality mesh at these areas of the model. Further research is not conducted with regard to this finding, but it is recommended for possible future work. In addition, a comparison of simulation is performed with air as MUT for the ‘Finer’ mesh configuration, between the original model and the model that simplifies the surface of the SMA as a perfect electrical conductor. This test shows that there is hardly any difference in the simulation results for the two models. This confirms that the simplification is a plausible solution assuming limited availability of computational resources.

Firstly, single homogeneous MUT with a thickness of 2 cm, which is assumed as infinitely thick for the sensor B, is placed above the sensor and simulated.

Secondly, non-uniform layers of these MUTs are established above the sensor and simulated. For the purpose of reference, two scenarios are included for the non-uniformity simulations:

The first scenario is only a slope over the waveguide filled with MUT. The slope geometry is used as a representation of the non-uniformity in the thickness. Above the slope, the material is modelled to be air. The geometry is shown in Figure 3.17.

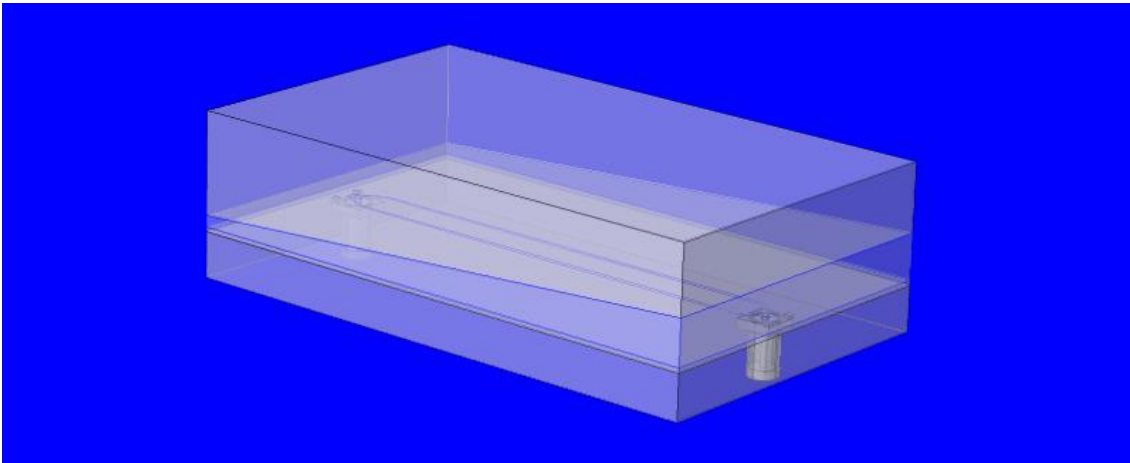


Figure 3.17 The slope geometry established for model of sensor B.

The dimensions are 2 mm at the lower end and 8 mm at the higher end. The purpose of the design is for the sensor to simulate the non-uniform thickness of the MUT, which can give new insight into the research concerning examination of random non-uniformity in hydrate deposition layers. In this project, the homogeneity of the MUTs is kept constant while its geometrical formation, i.e. its thickness distribution over the parallel direction of the planar transmission lines is altered. These tests will provide information on how the difference in the thickness of MUT will influence the measured S-parameters and thereby the calculated effective permittivity. Reversely, knowledge is gained on how the calculated effective permittivity can be related to information of the thickness of the MUT. The MUTs in the simulation are chosen with regard to the substances that will be used in the experiments. Complete simulation of hydrate formation is not included in the project.

The second scenario is a flat cuboid above the waveguide of a homogeneous MUT with thickness being that of the average thickness of the slope scenario described above, i.e. 5 mm. This is to establish a reference scenario using the same amount of MUT as in the non-uniform case, but in a uniform structure. In this way, assessment can be made on how the non-uniformity affects the measured S-parameters, and thereby the effective permittivity.

3.5.2 Results

The results in the form of measured S-parameters, including both magnitude and phase are shown in Figure 3.18 with air, Figure 3.19 with distilled water and Figure 3.20 with

methanol as MUTs respectively. For water and methanol as MUTs, the figure consists of three cases that are compared:

MUT in the form of cuboid with the depth of 2 cm under the mark ‘bulk’;

MUT in the form of a slope under the mark ‘slope’;

and MUT in the form of flat cuboid under the mark ‘flat’.

There is only one case for air since the controlling medium above other liquid slope is air itself.

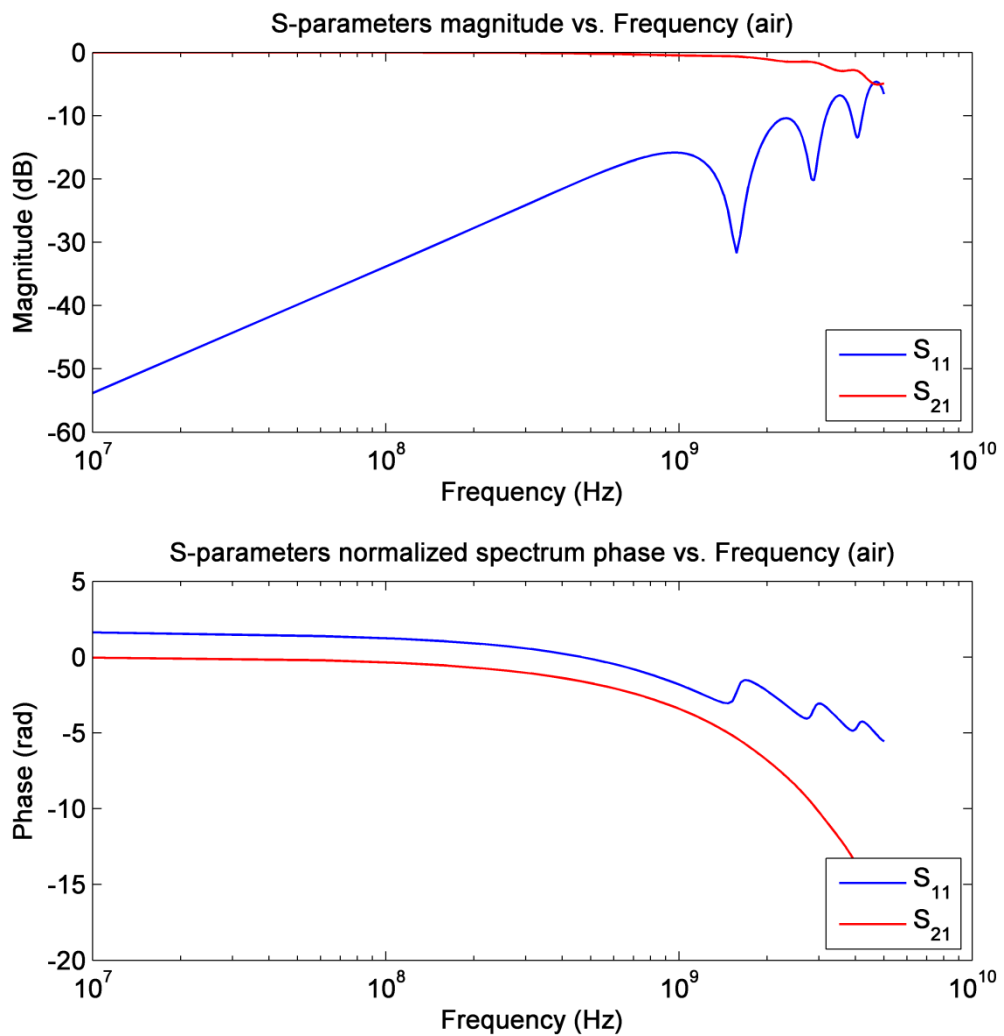


Figure 3.18 Magnitude and phase of measured S-parameters with air as MUT in simulation on sensor B.

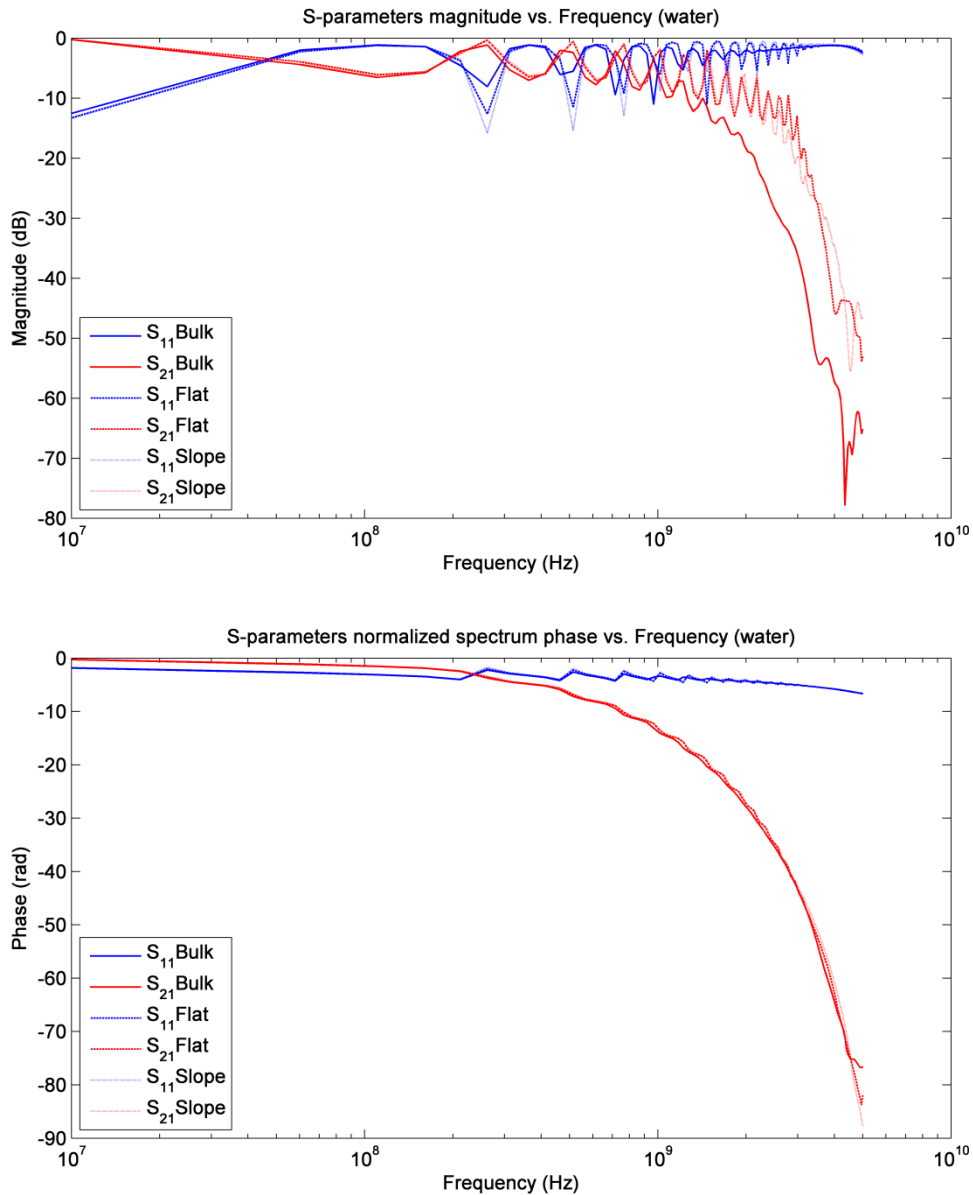


Figure 3.19 Magnitude and phase of measured S-parameters with water as MUT in three simulation scenarios on sensor B.

As shown in Figure 3.19, the magnitude of transmitted signal attenuates more rapidly in the ‘bulk’ case, compared to ‘flat’ and ‘slope’ cases when the container is just partially filled. Magnitude of reflected signal appears to be more stable in ‘bulk’ case compared to the fluctuated ones of the other two cases. It also appears that both reflected and transmitted signals in ‘slope’ and ‘flat’ case are very similar to each other. The reason might be that the amount of liquid in both cases is the same. On the contrary, there is hardly any difference in phase for both reflected and transmitted signals among all three cases.

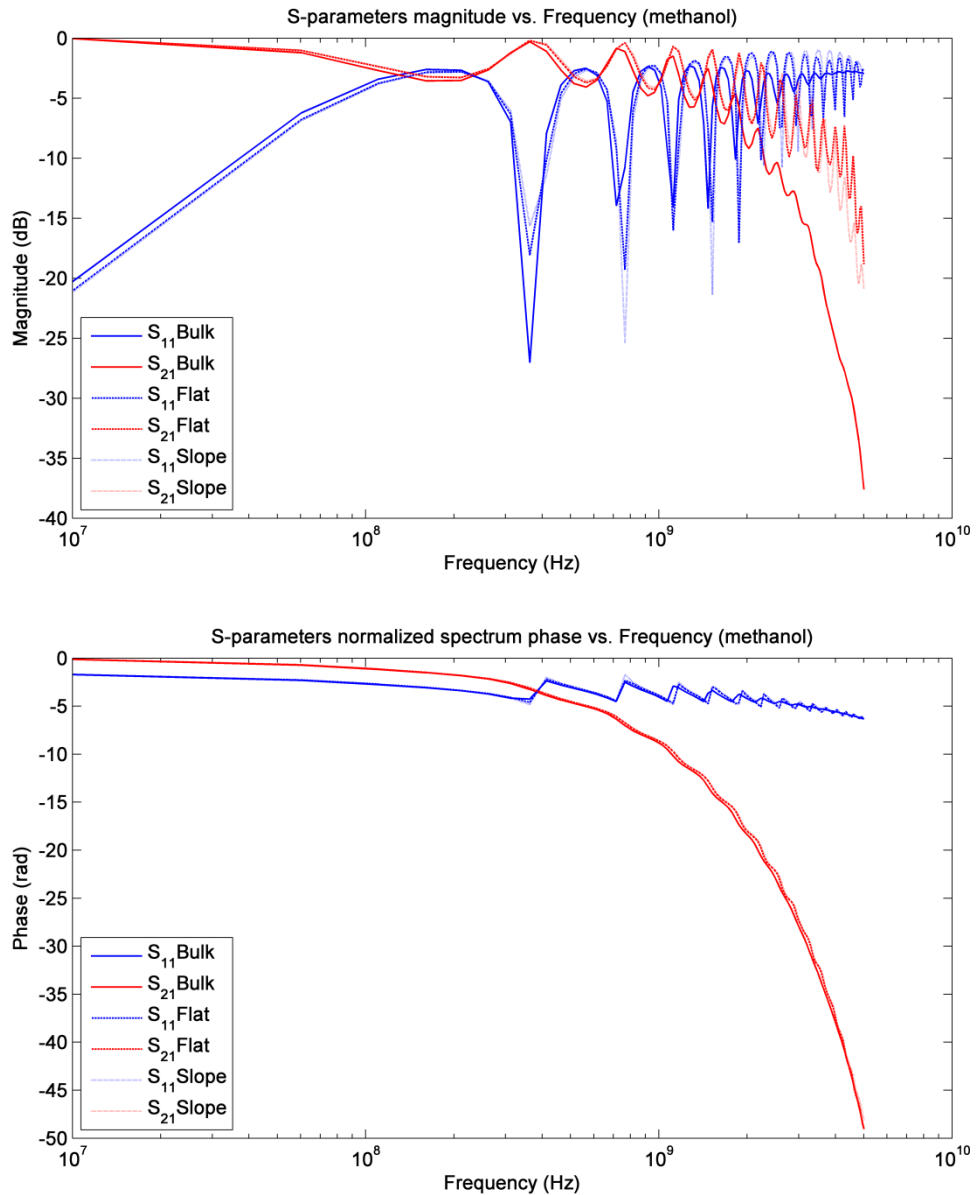


Figure 3.20 Magnitude and phase of measured S-parameters with methanol as MUT in three simulation scenarios on sensor B.

As shown in Figure 3.20, the magnitude of transmitted signal attenuate more rapidly in the ‘bulk’ case, compared to ‘flat’ and ‘slope’ cases. Similar to the results for water, magnitude of reflected signal appears to be more stable in ‘bulk’ case compared to the fluctuated ones of the other two cases. Again, both reflected and transmitted signals in ‘slope’ and ‘flat’ case are very similar to each other. There is hardly any difference in phase for both reflected and transmitted signals among all three cases.

3.6 Design of sensor B and sensor C

Two sensors are made in the project, named sensor B and sensor C.

The actual thickness d of the substrate of the CPW on the PCB is between 0.01 mm to 0.03 mm (Appendix). Obviously, a contact between the underside of the substrate and any metallic material would create a GCPW, meaning that a significant part of the electric field energy would be directed to the area under the CPW. Therefore, a structure of known material - solid PVC (Polyvinyl chloride) is attached to the underside of the substrate, partially for supporting the flexible CPW to maintain its desired form, as well as for a better measurement setup compared to directly attaching it to metallic or uncharacterized material.

The permittivity ϵ_{sub} of the dielectric substrate affects the measurement. Increasing permittivity of the substrate leads to reduced sensitivity. This can be explained by the increasing loss of electric field to the substrate. Therefore, low permittivity of the substrate is also required for the sensors. PVC substrate used in both sensors has dielectric constant of approximately 3, which is close to the original thin substrate of the waveguide layer. A thin layer of adhesive compound, with a dielectric constant of 3.6, is located between the contact of the layer and the PVC substrate to ensure sufficient mechanical stability of the sensor surface and to prevent leakage of MUT to the underside of the CPW. The dispersion of the substrate permittivity as a function of frequency is neglected.

The connectors at the two ends of the CPW penetrate through the PVC substrate to make contact with CPW on the upper surface of the sensor. The legs of the connectors that penetrate through towards the surface are soldered to the CPW. When coaxial cables are connected to the sensor for measurement, the soldering itself is not strong enough to hold the SMA connectors stable. Therefore, the connectors are mechanically fixed inside the substrate so that it is not susceptible to movement that will distort the measurement signal.

The two sensors have different outer structure, i.e. containers holding the MUTs. They are explained in detail separately.

3.6.1 Structure of sensor B

As shown in Figure 3.21, the designed CPW is placed and fixed on a flat substrate in sensor B.

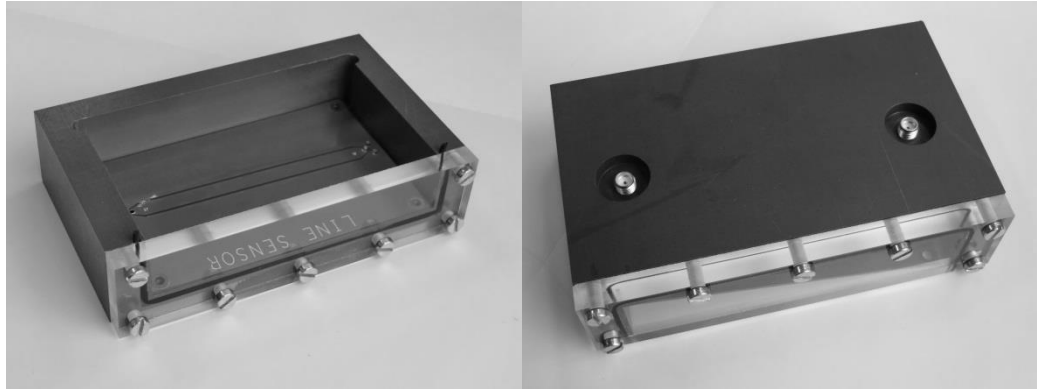


Figure 3.21 The structure of sensor B as seen from the top and the bottom.

The grey-coloured wall and the substrate are made of PVC. Together with one side of transparent wall made of PMMA (Polymethyl methacrylate), the PVC walls form a container able to contain most non-corrosive hydrocarbons. The depth of the container, i.e. to CPW surface, is 2 cm, which when fully loaded, has sufficient thickness to be considered as being of infinite depth.

The two SMA connectors are embedded in the PVC substrate. Their legs are soldered to the strips of the coplanar lines. Extra spaces are made on the backside of the substrate for the SMA to be connected to the coaxial cables.

3.6.2 Structure of sensor C

As shown in Figure 3.22, the designed CPW is placed and fixed on a semi-cylindrical substrate in sensor C.

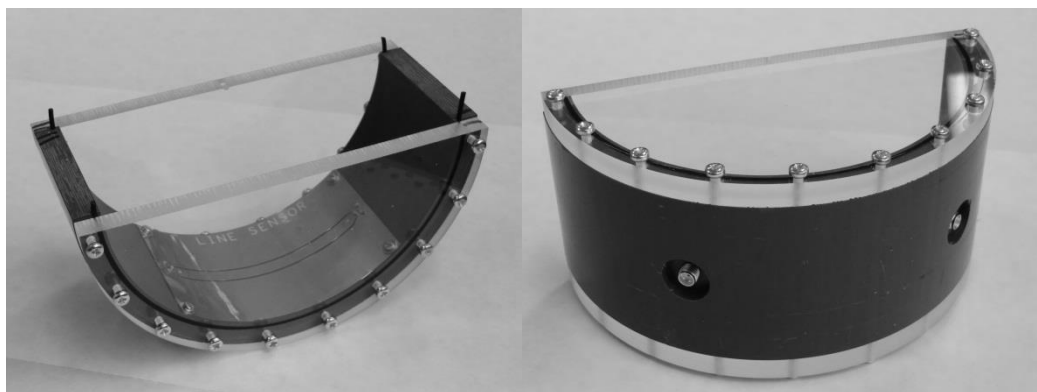


Figure 3.22 The structure of sensor C as seen from the top and the bottom.

Similar to sensor B, a container-like structure is formed above the CPW. The difference here is that the lower surface of the container is curved. The purpose of the design is to construct an experimental setup to simulate that of a pipeline. The container is formed

by two PMMA side fences in addition to the PVC substrate. The SMA connectors are embedded into the substrate as they are for sensor B.

4 EXPERIMENTS

In this chapter, the experiments conducted on the sensors are described, procedures documented and results presented. Initially, the experiments repeated on sensor A are briefly presented. Following, the experiments of both uniform and non-uniform layers on sensor B are described. Finally, the experiments on sensor C are presented.

List of equipment used is shown in Table 4.1.

Table 4.1 Equipment used in the experiments

Equipment	Model
Network Analyser	Rohde & Schwarz ZVL Network Analyser
Cables	Rohde & Schwarz ZV-Z191
Calibration Kit	Rohde & Schwarz ZV-Z132 CAL KIT

4.1 Experiments repeated on sensor A

The experiments conducted on sensor A were repeated. Air, distilled water, 1-Pentanol, methanol and acetone were used as MUTs, as a replication of the original experiments performed.

4.1.1 Setup and procedure

The MUT samples are injected so that the container in the middle of sensor A is completely filled. Subsequently, the ports are excited by the network analyser while the measurements are taken. Each measurement is averaged over 10 frequency sweeps.

Afterwards, the cleaning of the container is performed by sucking the liquid used in the finished experiment utilizing a syringe. This is followed by removing the residue using a paper towel. Before a new measurement is taken on the next sample, a reference measurement on air is taken. The purpose of this is to investigate whether there is still residue on the sensor surface as well as whether it will affect the measurement result.

4.1.2 Results

The results for air, water and methanol are shown in the following figures. Results for 1-Pentanol and acetone are recorded in Figure 6.2 and Figure 6.3 in Appendix. The figures show magnitude and phase of S_{11} and S_{21} , for both the new and the old results.

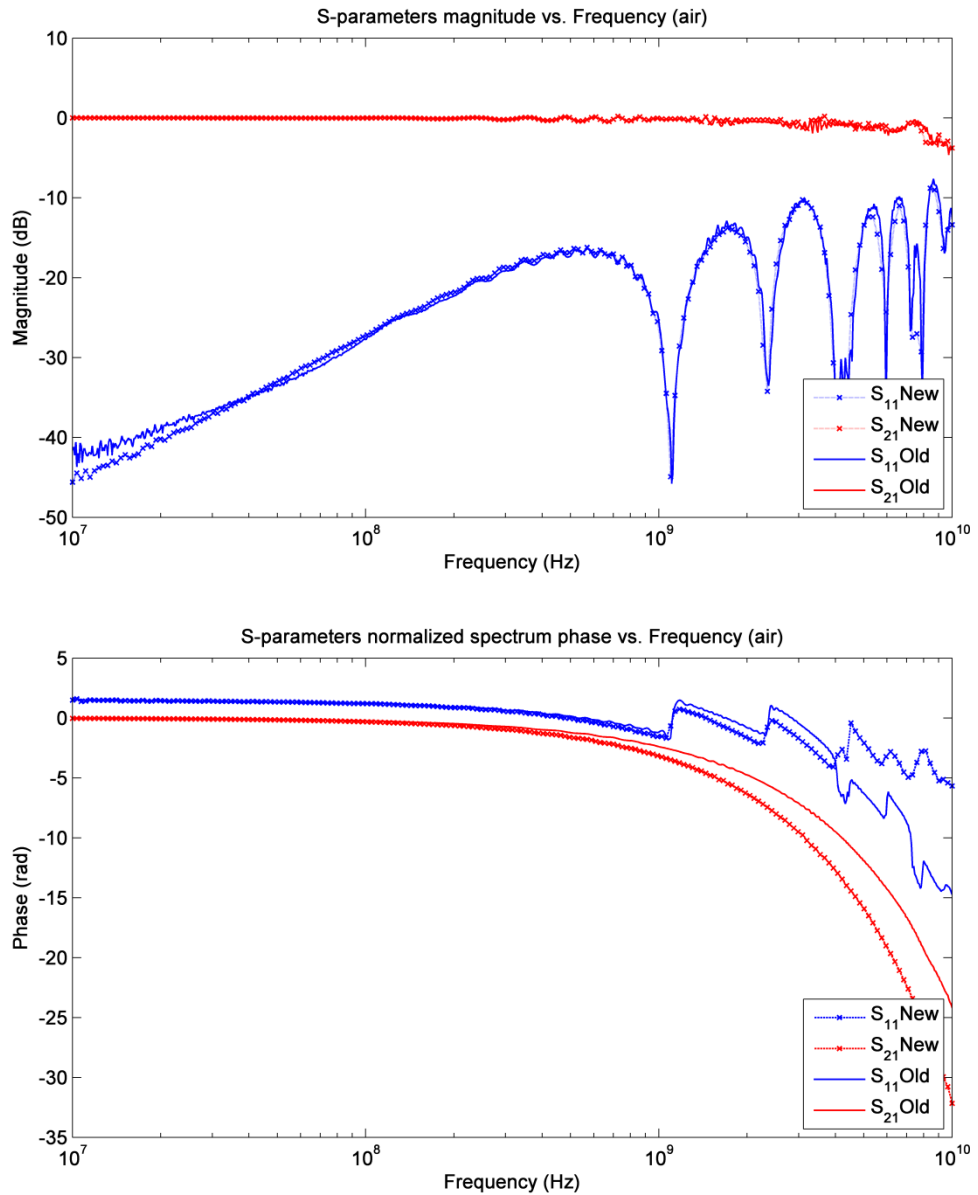


Figure 4.1 Comparison between new and old measurement taken with air as MUT on sensor A.

As shown in Figure 4.1, the magnitude of both newly measured S_{11} and S_{21} (dotted lines with cross marker) correspond well to the old ones, while there are some deviations in the phase. The jump of new S_{11} phase at the end of the spectrum is due to limitation of unwrapping function in Matlab.

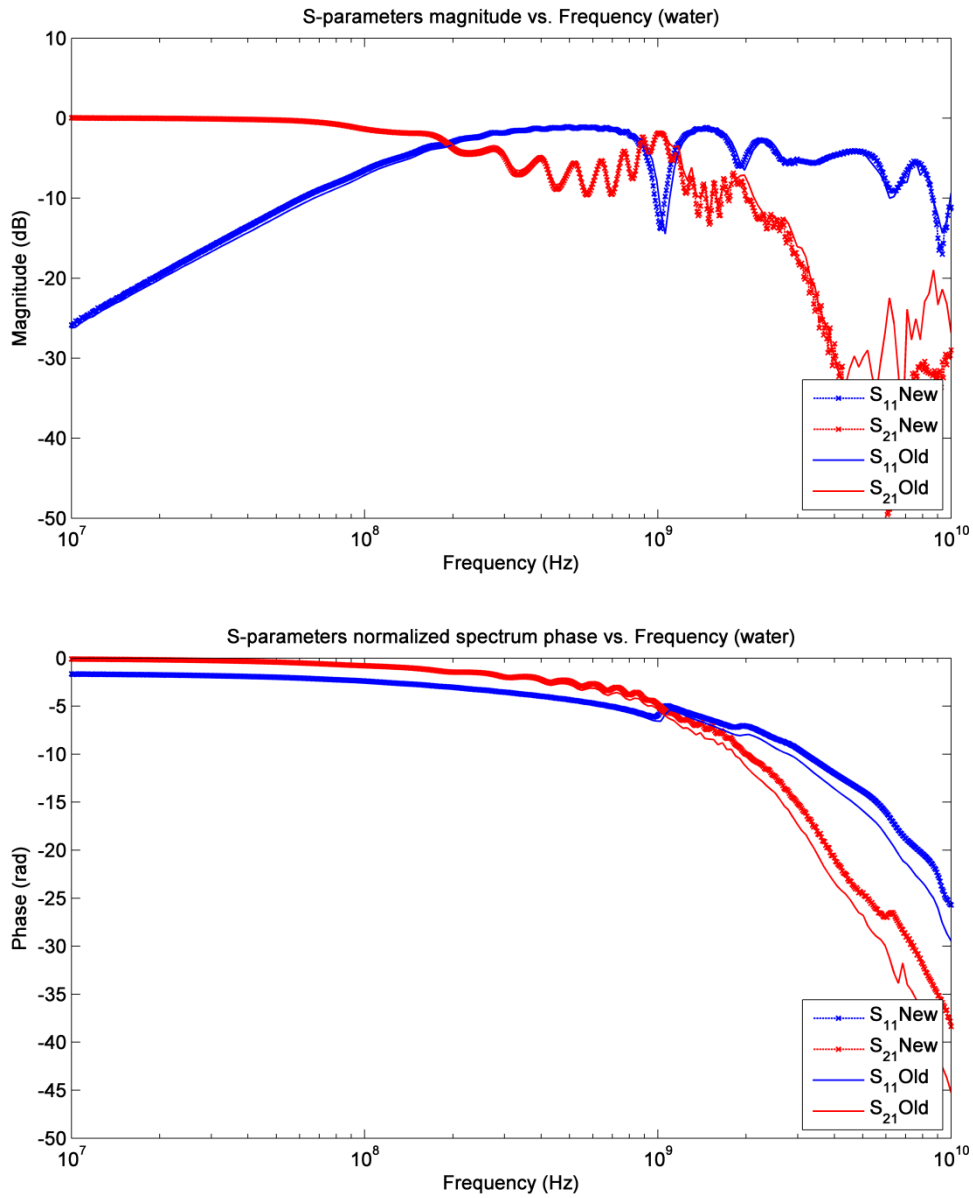


Figure 4.2 Comparison between new and old measurement taken with water as MUT on sensor A.

Similar to that of air, the results reproduced for water correspond to the old results well.

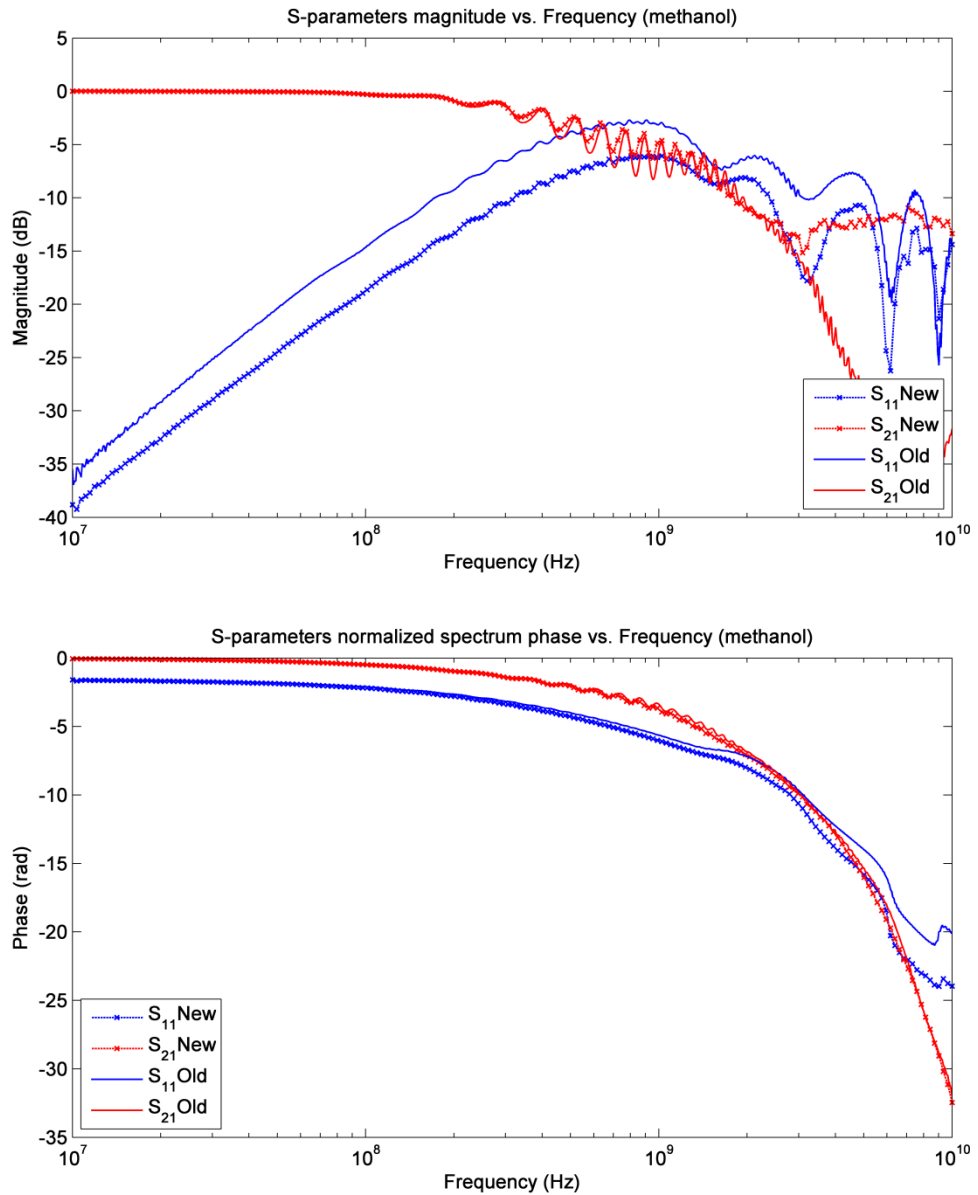


Figure 4.3 Comparison between new and old measurement taken with methanol as MUT on sensor A.

Figure 4.3 shows that the magnitude of S_{11} and S_{21} for methanol deviate a bit from the old results, while the phases fit well.

In general, most of the new results match well with those that were taken in the previous project. In addition, it appears that the residue left on the sensor can substantially affect the measurement afterwards. This observation is taken into account, and improvement on cleaning of the container is made in the following experiments.

4.2 Experiments on sensor B

Five MUTs are used in the experiments: air, distilled water, methanol, ethanol and vegetable oil. Their dielectric properties are presented in Table 4.2.

Table 4.2 Cole-Cole parameters that describe the dielectric properties of MUTs at 20 °C (Haukalid, 2011; Jakobsen & Folgerø, 1997; Vrba & Vrba, 2013).

MUT	ϵ_s	ϵ_∞	τ [ps]	α
Air	1			
Water	80.21	5.6	9.36	
Methanol	34.8	4.5	56	0.044
Ethanol	25.13	2.98	192	
Vegetable oil (sunflower)	3.233	2.275	2791	

4.2.1 Setup and procedure

Sensor B is captured firmly by a three-leg fixation device. The two ports under the sensor are connected to the network analyser by two coaxial cables with N-type on the side of the network analyser and SMA adaptor on the side of the sensor. By gravitational pull, the vertical connection ensures that the connections from the cable to the SMAs are stable and if slightly displaced, will return to its initial position. A photograph of the configuration is shown in Figure 4.4.



Figure 4.4 Photograph of the vertical coaxial connection on sensor B.

The sensor is placed inside a ventilation chamber for performing experiments with hazardous MUTs. The other ends of both coaxial cables are connected to the network analyser. A photograph of the experiment setup is shown in Figure 4.5.

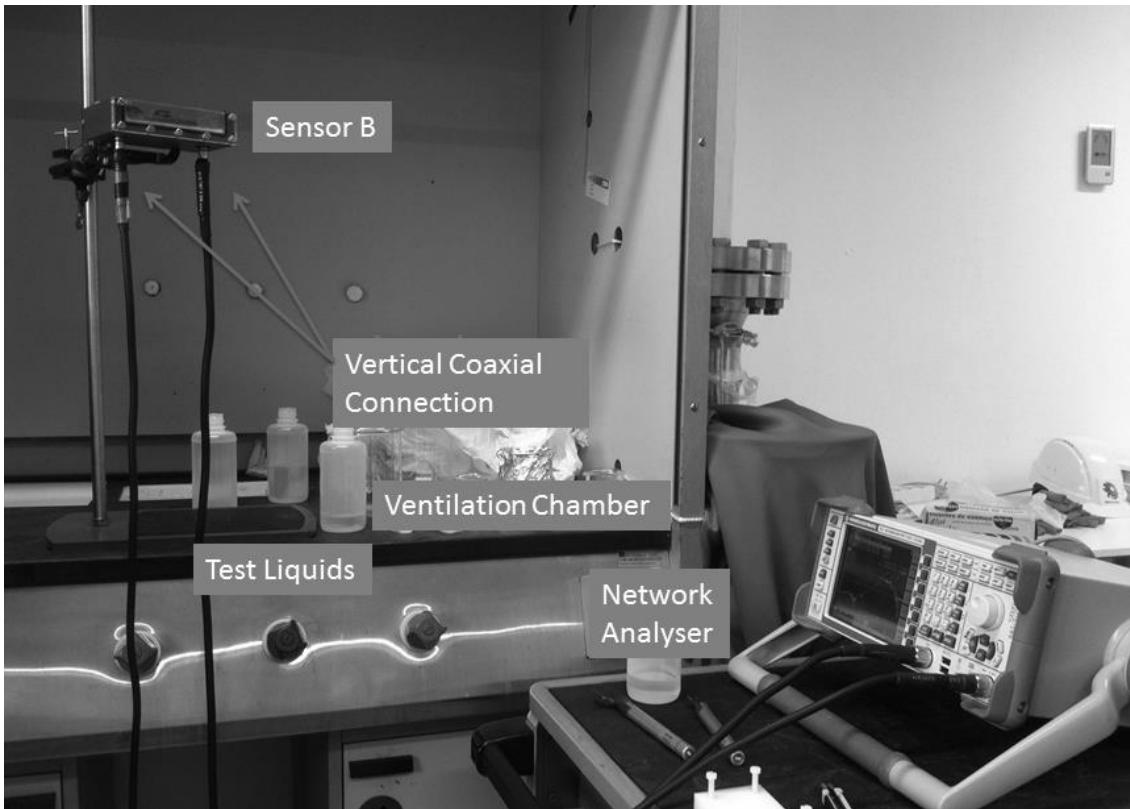


Figure 4.5 Photograph of experiment setup.

In the first phase of the experiments, samples are injected so that they completely cover the container over the sensor, as shown in Figure 4.6. MUT in this case is assumed infinitely thick. Ports are then excited by network analyser and measurements are taken. Similar to that of sensor A, each measurement is averaged over 10 frequency sweeps from 10 MHz to 10 GHz.

A similar cleaning procedure to that of sensor A is adopted. After each measurement, the liquid is taken away using syringe multiple times. Following that, the residue is wiped by paper towel carefully. Since most of the MUT in the experiment evaporate rapidly, a waiting period is included before each new measurement to ensure no residue is left. Before new measurement is taken on the next sample, a reference measurement on air is taken. The result is directly compared to the reference measurement with air. The purpose is to ensure that no residue of the previous experiment is left. After the last measurement, the setup is disassembled and contained carefully washed with a dishwasher liquid solution (“Zalo”).

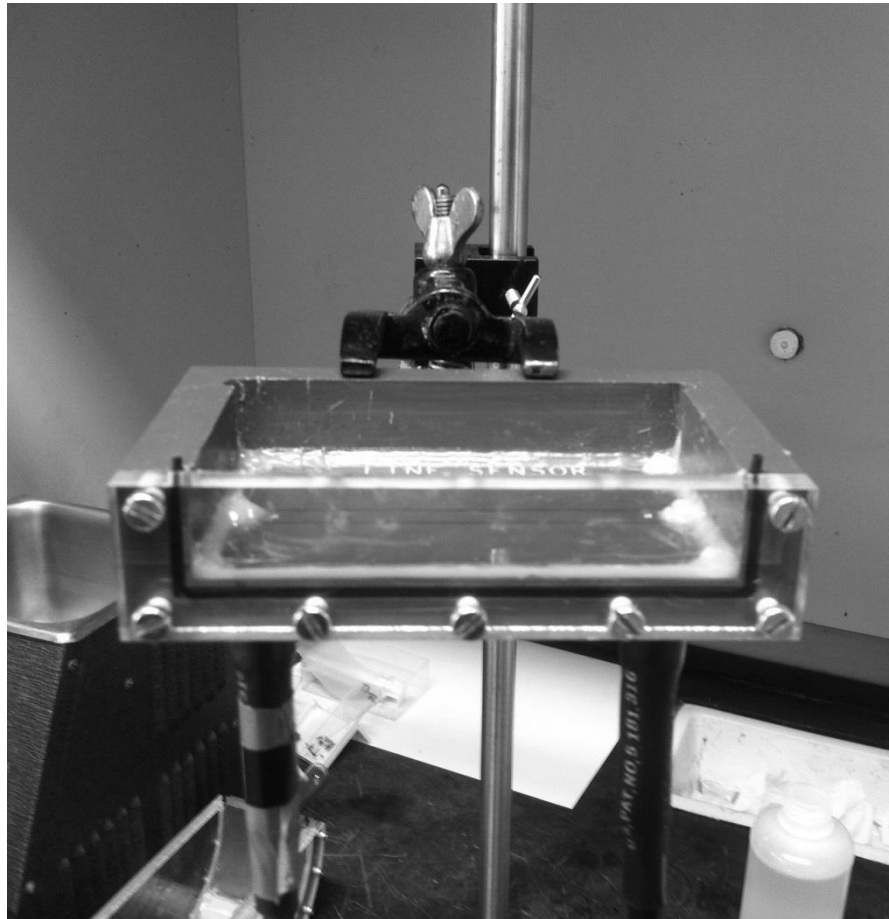


Figure 4.6 Close photograph from above sensor B during the experiment.

In the second phase of the experiments, control over the non-uniform thickness of MUT is applied to air, water and ethanol, where groups of measurements are taken for MUT of various thicknesses and geometries. A phantom made of POM (Polyoxymethylene) is used to create non-uniform layer structure in the sensor as shown in Figure 4.7.

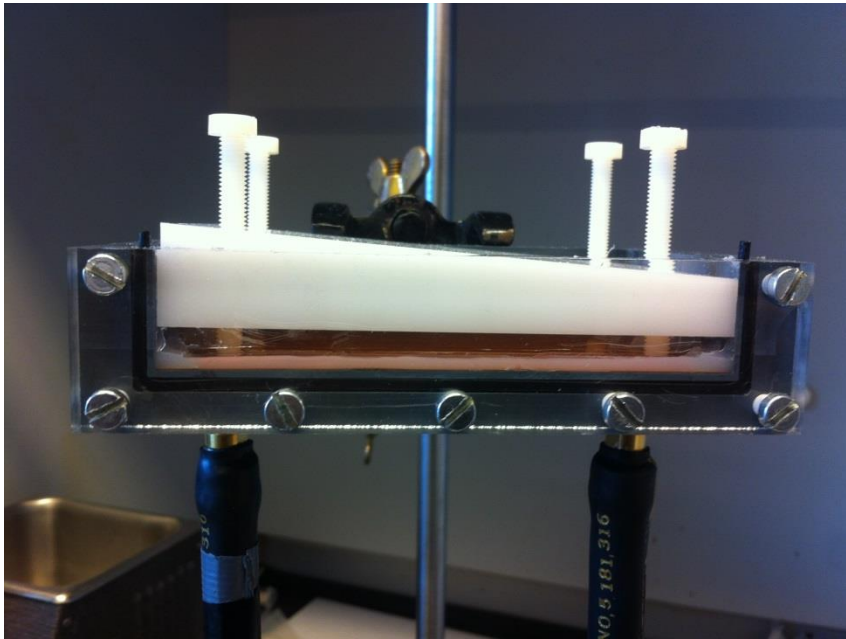


Figure 4.7 Photograph of using POM phantom to control the thickness of MUT.

Unlike in the simulation, it is not possible to control the shape of liquid without a specially designed object. The phantom can be flipped over and create non-uniform layer of MUT. The phantom is constructed in the form of a slope with dimensions that can fit into the container of sensor B. Difference in thickness between two ends of the slope is 6 mm, which is exactly same as the slope modelled in simulation.

Firstly, the measurements are performed while the container of the sensor is completely filled with MUT. Then the phantom is placed as shown in Figure 4.7 to form MUT with different thicknesses. Following that, the slope side of the phantom is then applied for taking two measurements on layer in slope form. One of them with thickness of 3 mm at lower end and 9 mm at higher end, the other one 5 mm and 11 mm respectively. Finally, the phantom is removed and measurements are taken for MUT with thicknesses under 3 mm. This is because the phantom cannot be placed in a distance shorter than 3 mm to the sensor plane. The silicone gel placed along the sides has an average thickness of 3mm, which prevents the phantom to be lowered further.

After each experiment, syringe is used to suck out the liquid. Tissue paper is used to absorb the residue. Measurements are then taken continuously to see if the results are close to the results with air as MUT, in which case the residue of MUT can be confirmed to have evaporated completely. Once confirmed, a similar procedure is applied to another MUT.

4.2.2 Results

The results for air, water and ethanol are shown in the following figures. Results in the form of measured S-parameters, including both magnitude and phase are shown in with air, water and ethanol as MUTs respectively. Each of the figures consists of three cases compared:

MUT in the form of cuboid with the depth of 2 cm under the mark 'bulk';

MUT in the form of a slope (3 mm on the lower end and 9 mm on the higher end) under the mark 'slope';

and MUT in the form of flat cuboid (6 mm) under the mark 'flat'.

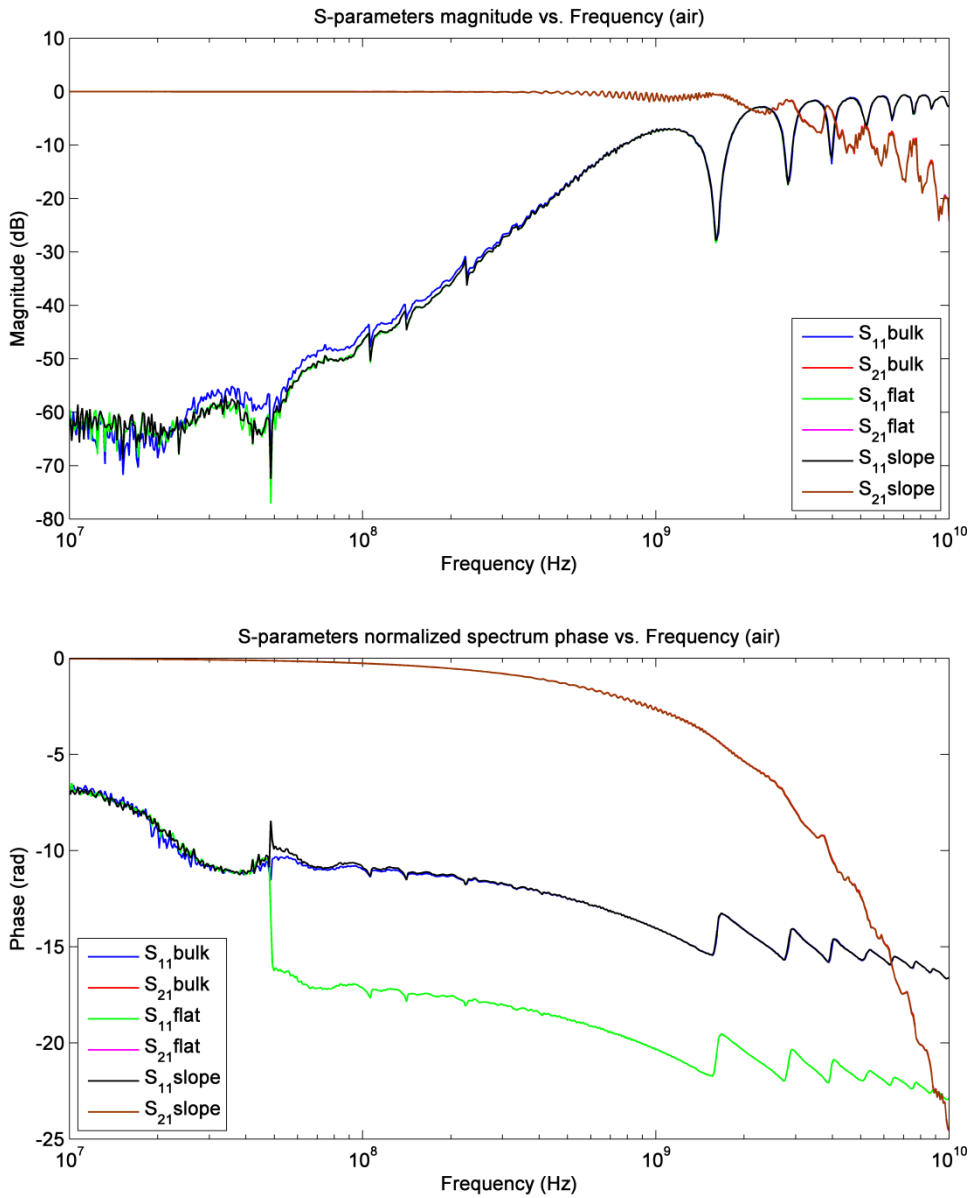


Figure 4.8 Magnitude and phase of measured S-parameters with air as MUT in three experiment scenarios on sensor B.

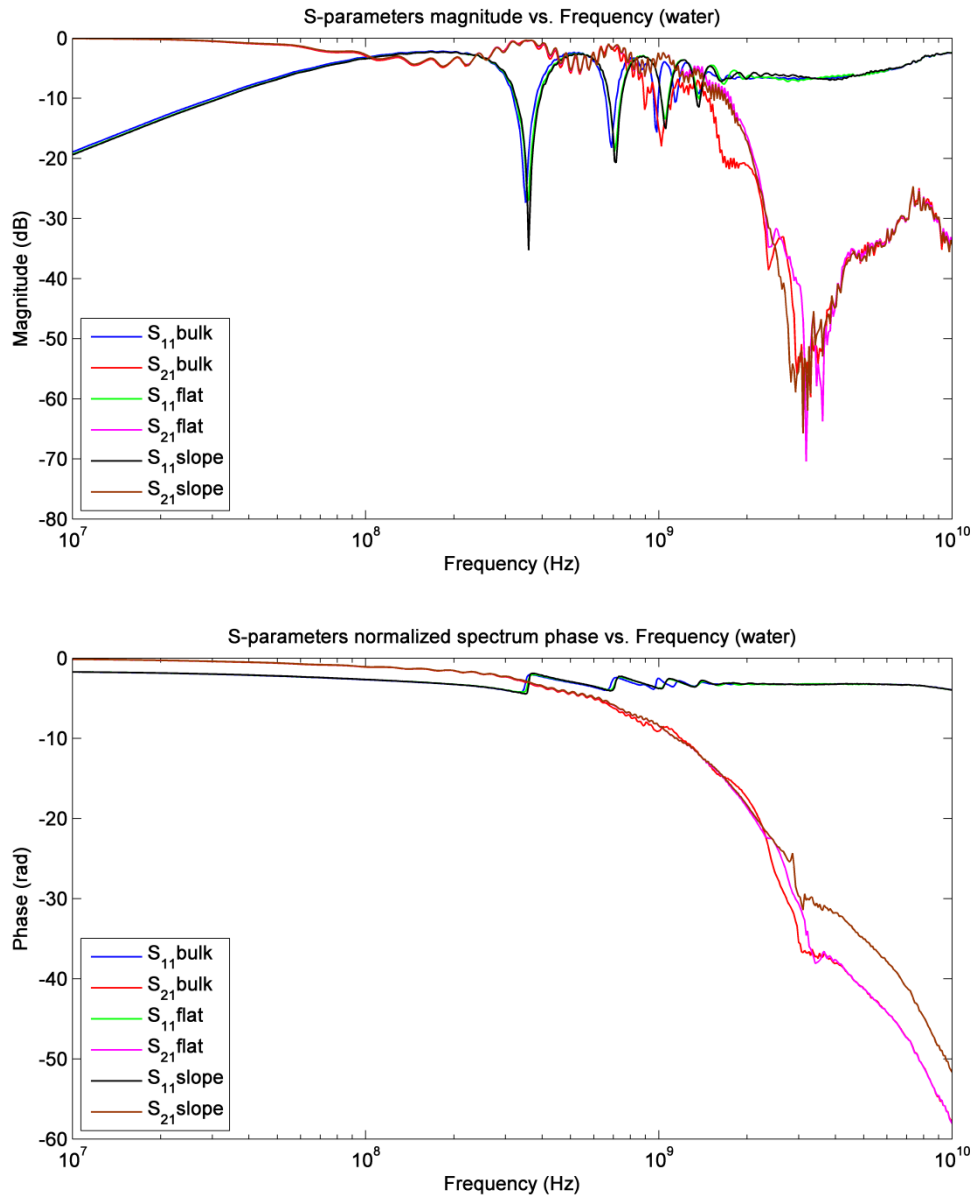


Figure 4.9 Magnitude and phase of measured S-parameters with water as MUT in three experiment scenarios on sensor B.

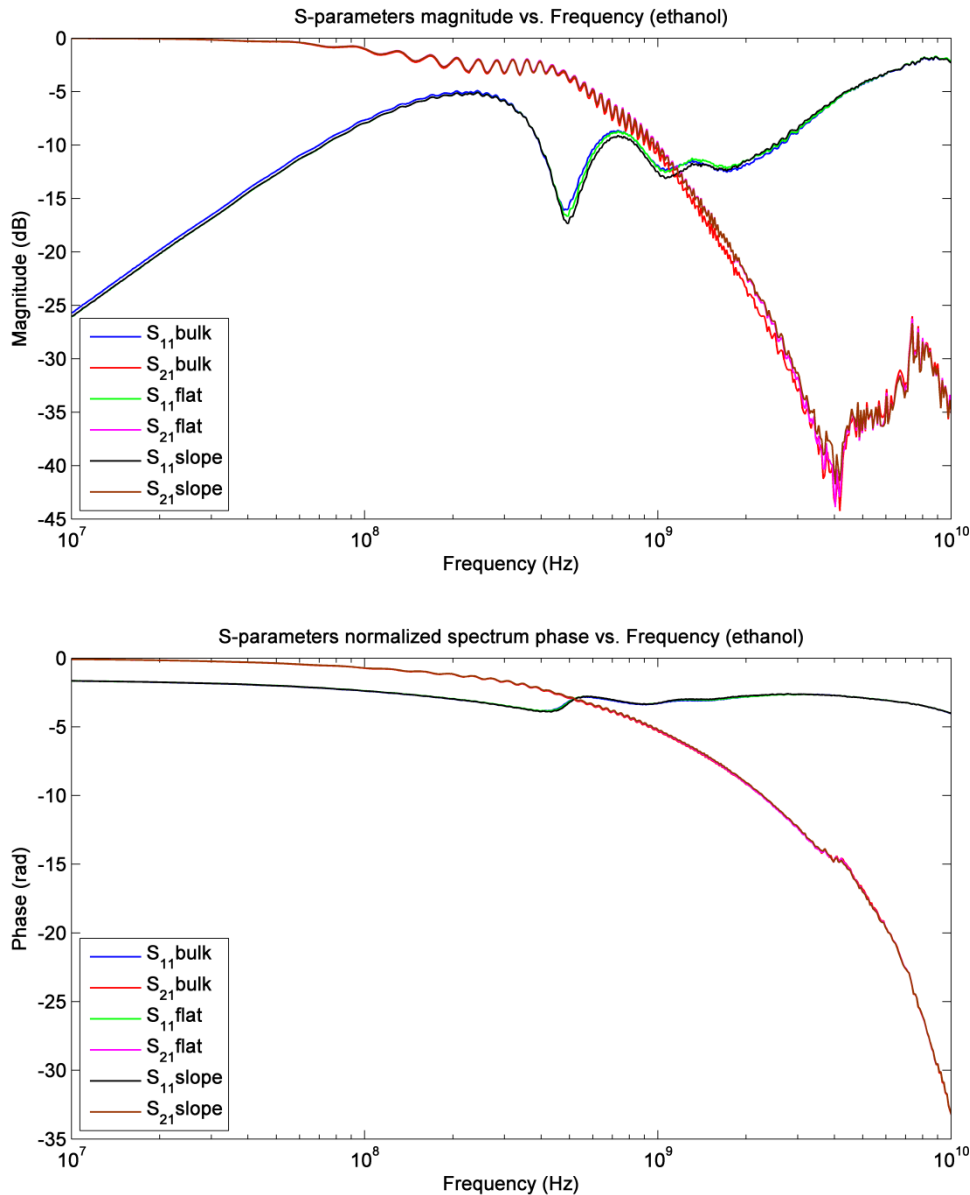


Figure 4.10 Magnitude and phase of measured S-parameters with ethanol as MUT in three experiment scenarios on sensor B.

In all the figures, the magnitude of S-parameters measured in ‘flat’ and ‘slope’ cases correspond to each other, while there is a small difference between them and those measured in ‘bulk’ case. This is anticipated according to similar simulation performed on sensor B in the previous chapter. Such relation is not observed in the phase of S-parameters.

As observed, the sensor produces similar measurement results for the same amount of MUT, and it is not dependent on the non-uniformity in thickness of MUT.

4.3 Experiments on sensor C

Same group of MUTs as used in experiments on sensor B are used for experiments on sensor C.

4.3.1 Setup and procedure

Similar to sensor B, sensor C is fixated inside ventilation chamber. The coaxial connections make approximately 45-degree angle to ground, as shown in Figure 4.11.

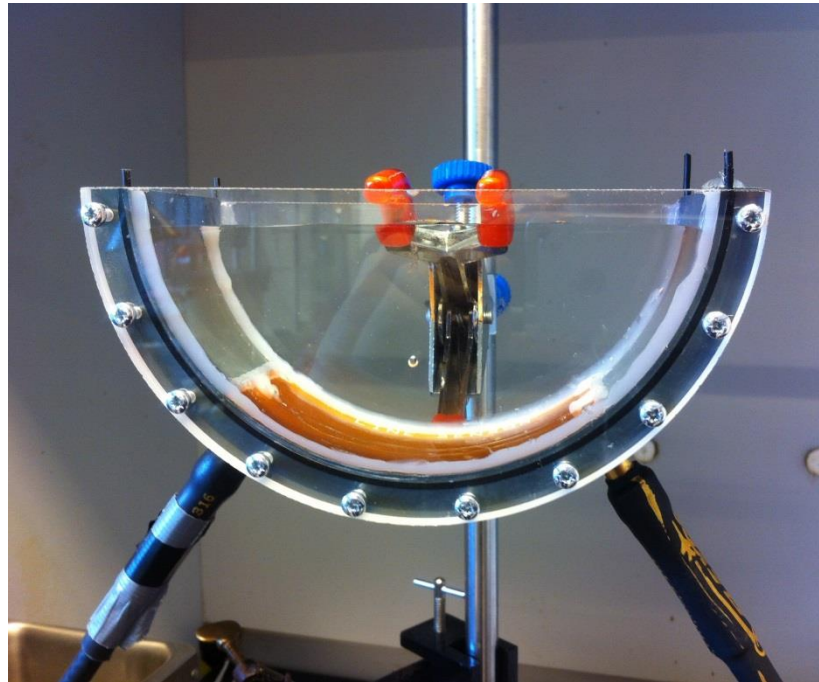


Figure 4.11 Photograph of sensor C during the experiment.

No POM phantom is created for sensor C. Instead, main purpose for sensor C is to examine how transmitted signal varies with regard to the bending of CPW.

4.3.2 Results

The results for air, water, methanol ethanol and vegetable oil are shown in the following figures. The figures show magnitude and phase of S_{11} and S_{21} , and they are compared with results of 'bulk' case from sensor B.

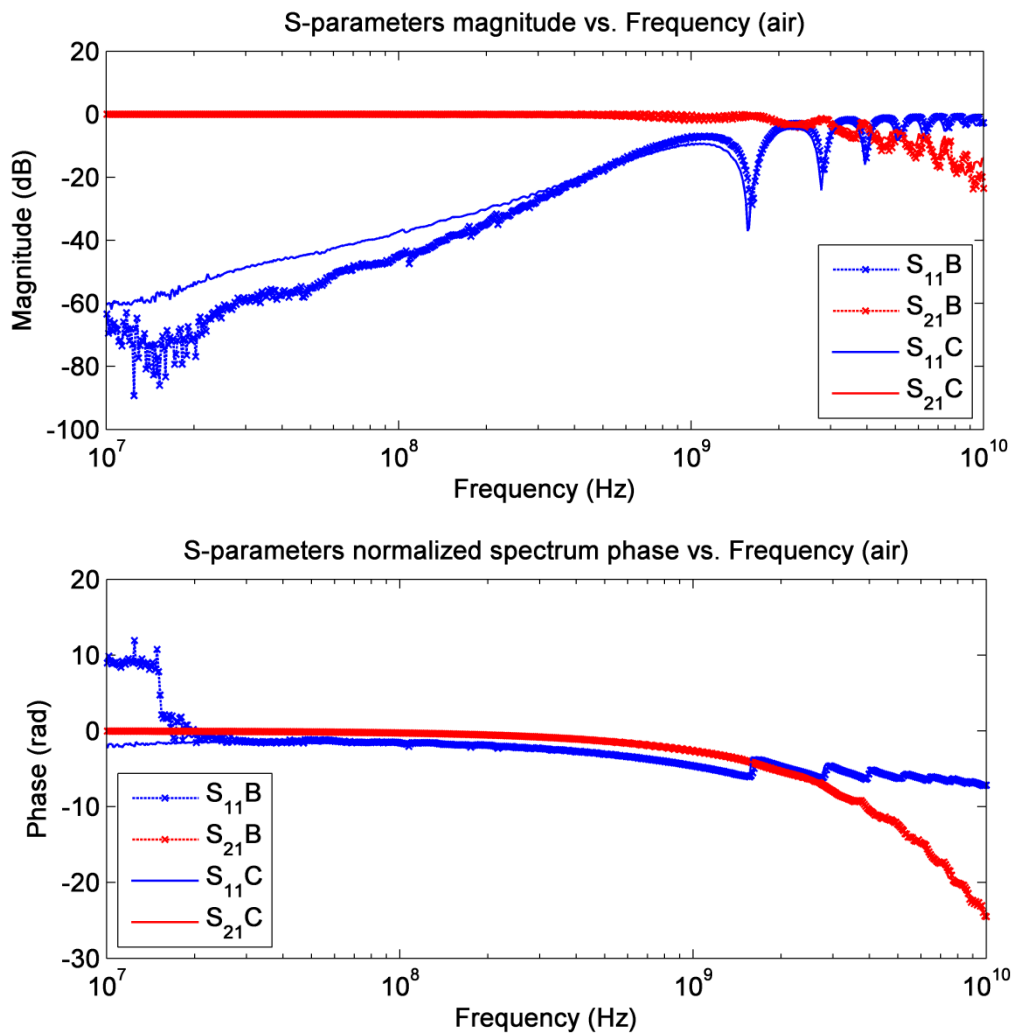


Figure 4.12 Measurement results compared for sensor B and C with air as MUT.

Figure 4.12 shows that the measurements performed on sensor C correspond well to those on sensor B, when air is used as MUT. The difference in phase for reflection loss is simply caused by mathematical calculation in unwrapping function inside Matlab.

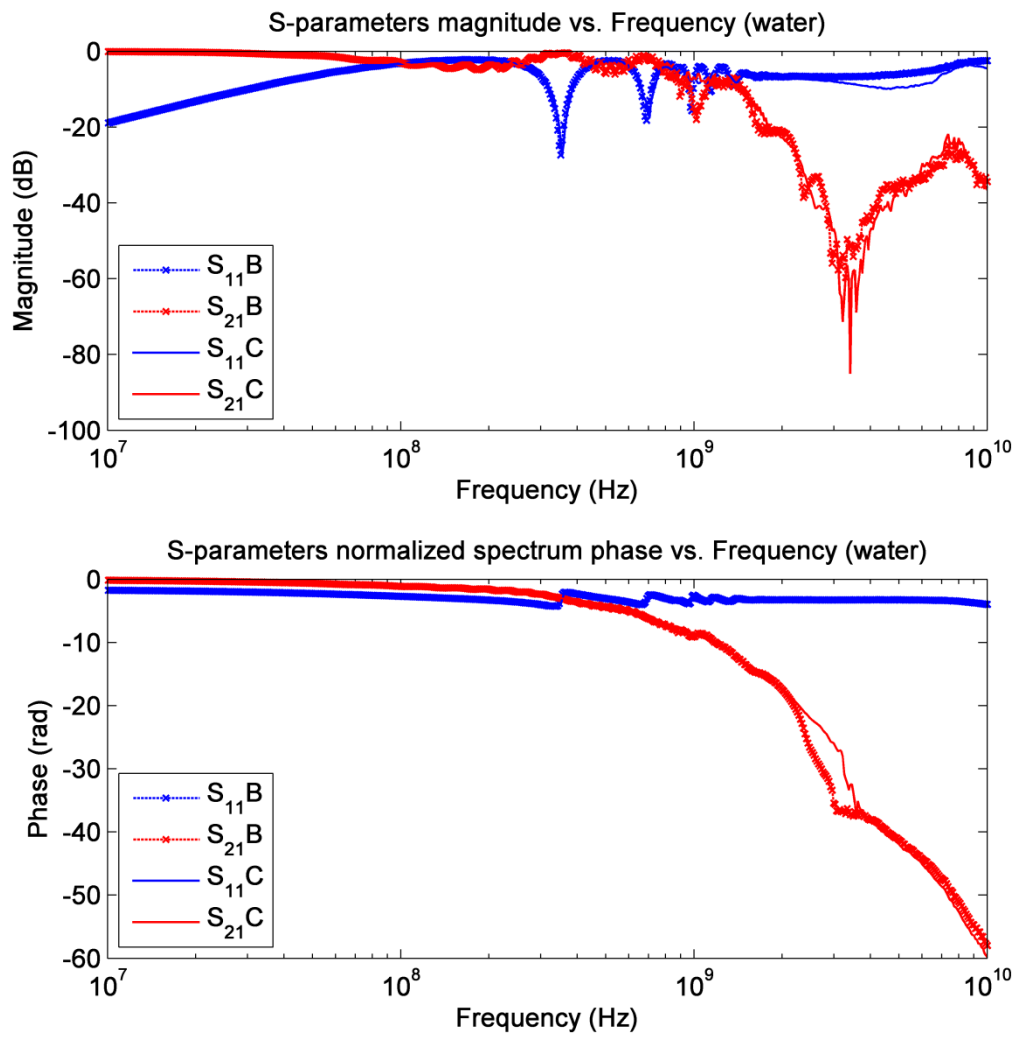


Figure 4.13 Measurement results compared for sensor B and C with water as MUT.

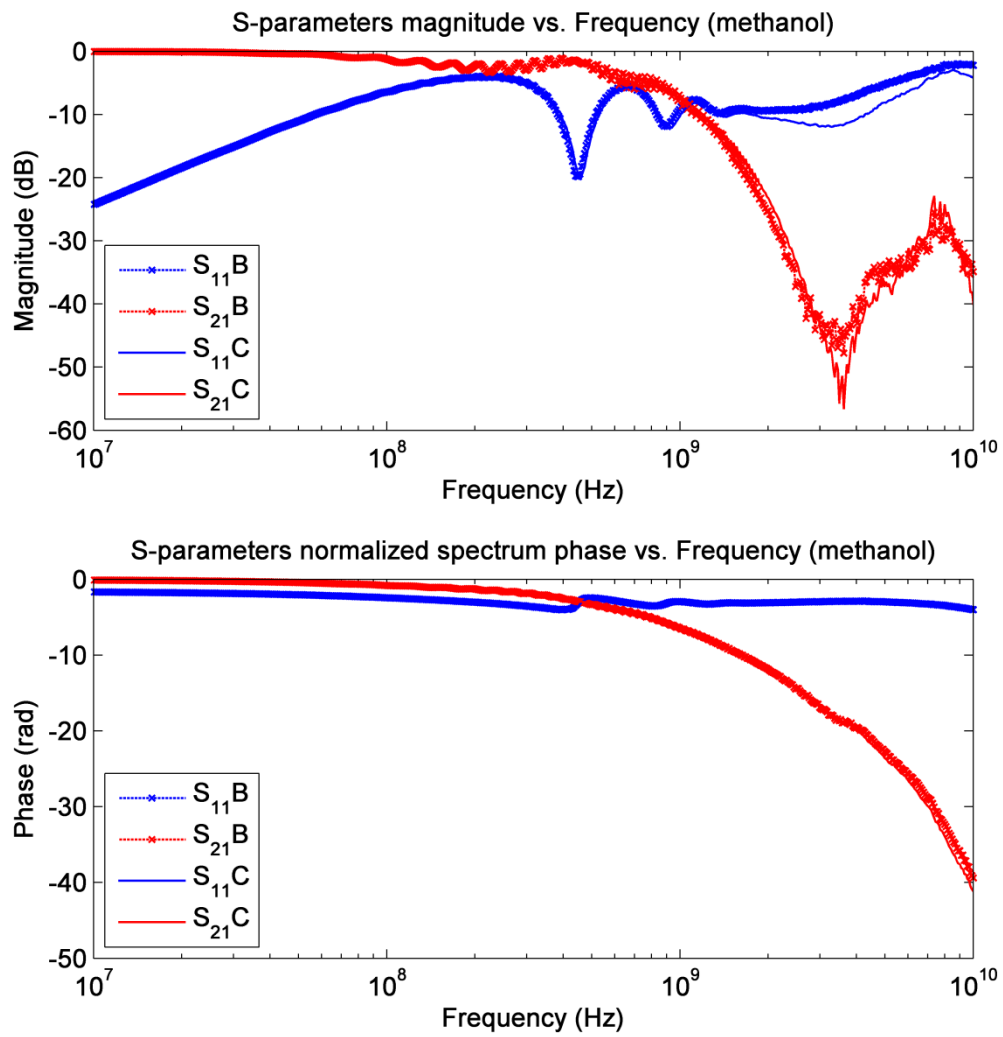


Figure 4.14 Measurement results compared for sensor B and C with methanol as MUT.

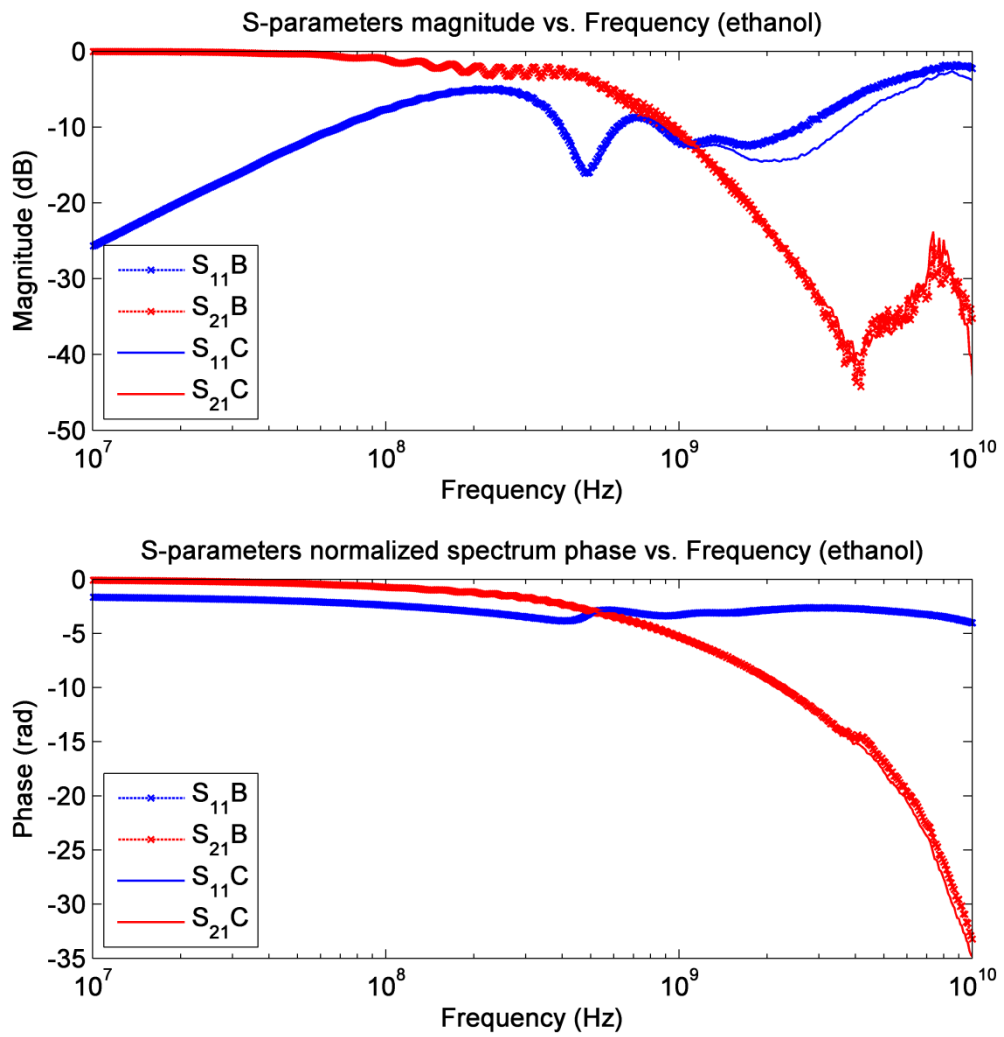


Figure 4.15 Measurement results compared for sensor B and C with ethanol as MUT.

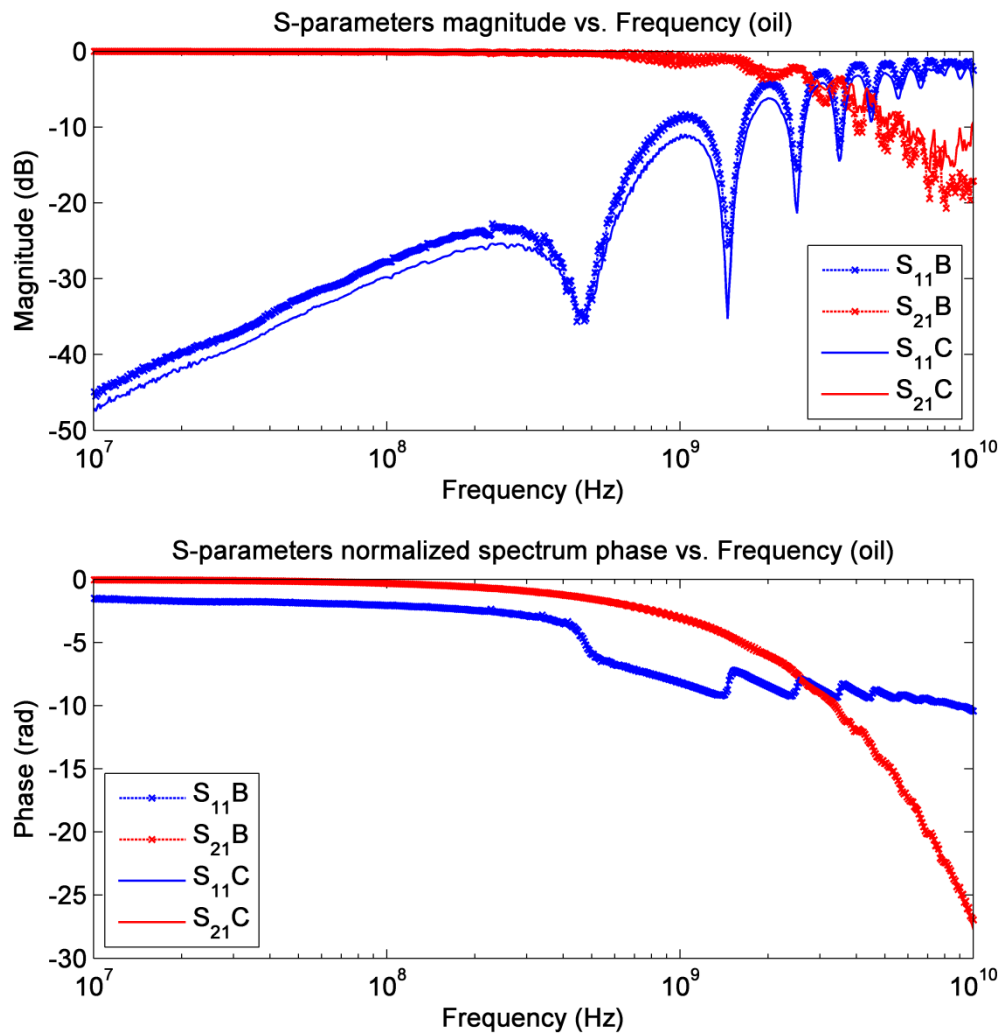


Figure 4.16 Measurement results compared for sensor B and C with vegetable oil as MUT.

All the above figures confirm that sensor C produces very similar measurement results as sensor B, inside frequency range from 10 MHz to 10 GHz for MUT with static permittivity from 1 up to 80. This confirms that the bending of PCB has minimal effect on the measurement performance of CPW. The CPW designed in this project can thusly adapt to different geometrical conditions.

While sharing the same CPW design, sensor B and C went through different construction process. Consequently, similar measurement performance is observed on both sensors. It can therefore be concluded that the manufacturing of such sensor with the same characteristics and quality is reproducible.

5 DISCUSSION

In this chapter, the results from chapter 3 and 4 are discussed. First, a comparison of performance between the sensors is presented. Then, simulations and experiments performed on sensor B are compared to verify the reliability of the simulation software. Following, liquid leakage encountered in experiments is discussed. Finally, the measurement results on non-uniform liquid layers and the comparison of calculated effective permittivity are discussed.

5.1 Comparison between sensors

One of the goals for this project is to test industrial viability of CPW-based permittivity sensors. Out of the two sensors built in the project, the flat sensor B is designed for comparison with sensor A. It is also constructed for preliminary testing on CPW using vertical connection and entire-surface measurement. The curved sensor C on the other hand, is built as a testing prototype – suitable for pipeline installation. Constructed differently, the two sensors are installed with CPW layer of the same design. Therefore, the experimental results on these two sensors are comparable. Consequently, an analysis on the comparison leads to improved knowledge on the industrial viability of the sensors.

5.1.1 Sensor A and sensor B

A comparison of the measured S-parameters for various MUTs on sensor A and sensor B is shown in the following figures:

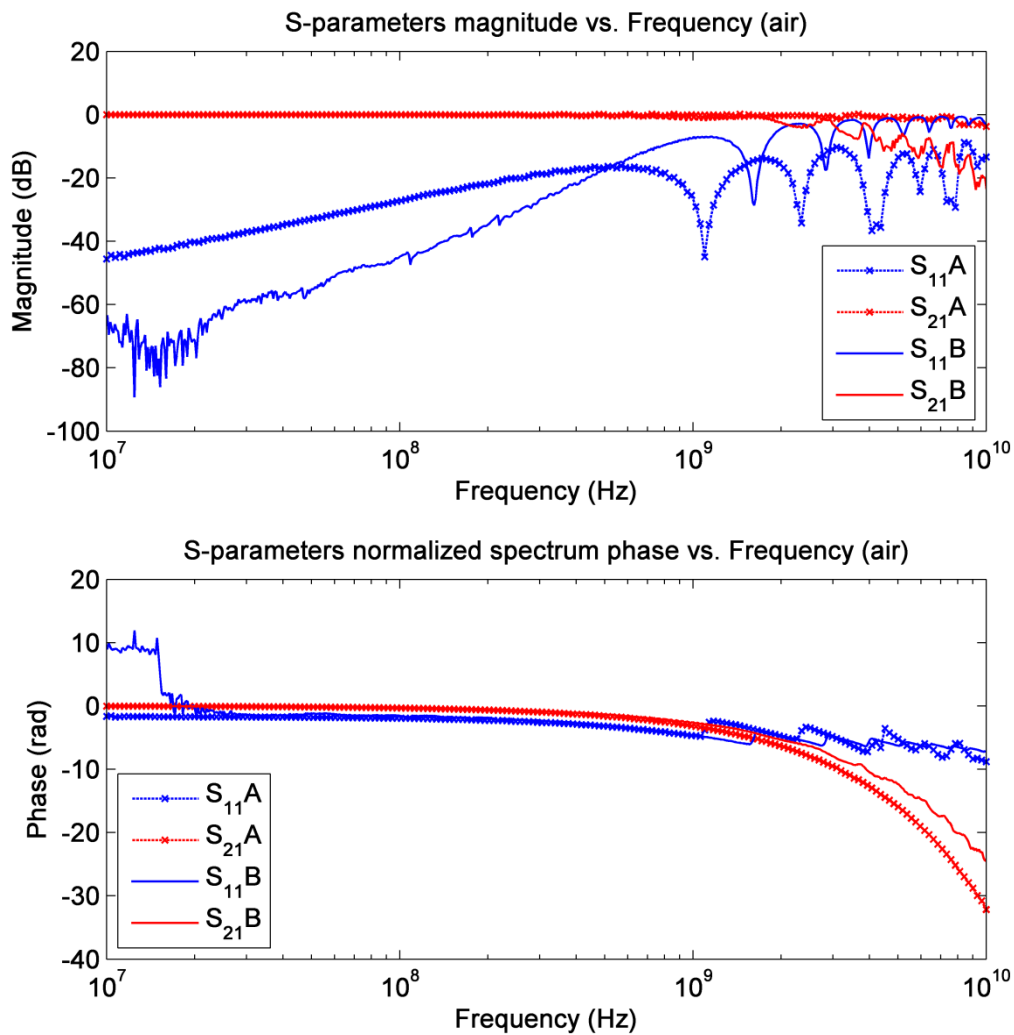


Figure 5.1 Measurement results compared for sensor A and B with air as MUT.

When measuring on air, the distance between the resonances (i.e. where S_{11} reach minus infinity) is defined by the electrical length between the coaxial connectors. Figure 5.1 shows that the first resonance occurs at 1 GHz for sensor A and approximately 1.5 GHz for sensor B, which indicates that the sensing area on sensor A is longer than that of sensor B.

When measuring on air, the main impedance mismatch is at CPW and coaxial transition, for both sensor A and sensor B. The container used to hold MUT on sensor A is built in the middle, while the total length between the coaxial connectors are longer which is 10 mm. Since the area outside the container is always filled with air, the sensing length when measuring air is thusly 10 mm. This is in fact longer than 87 mm used in sensor B.

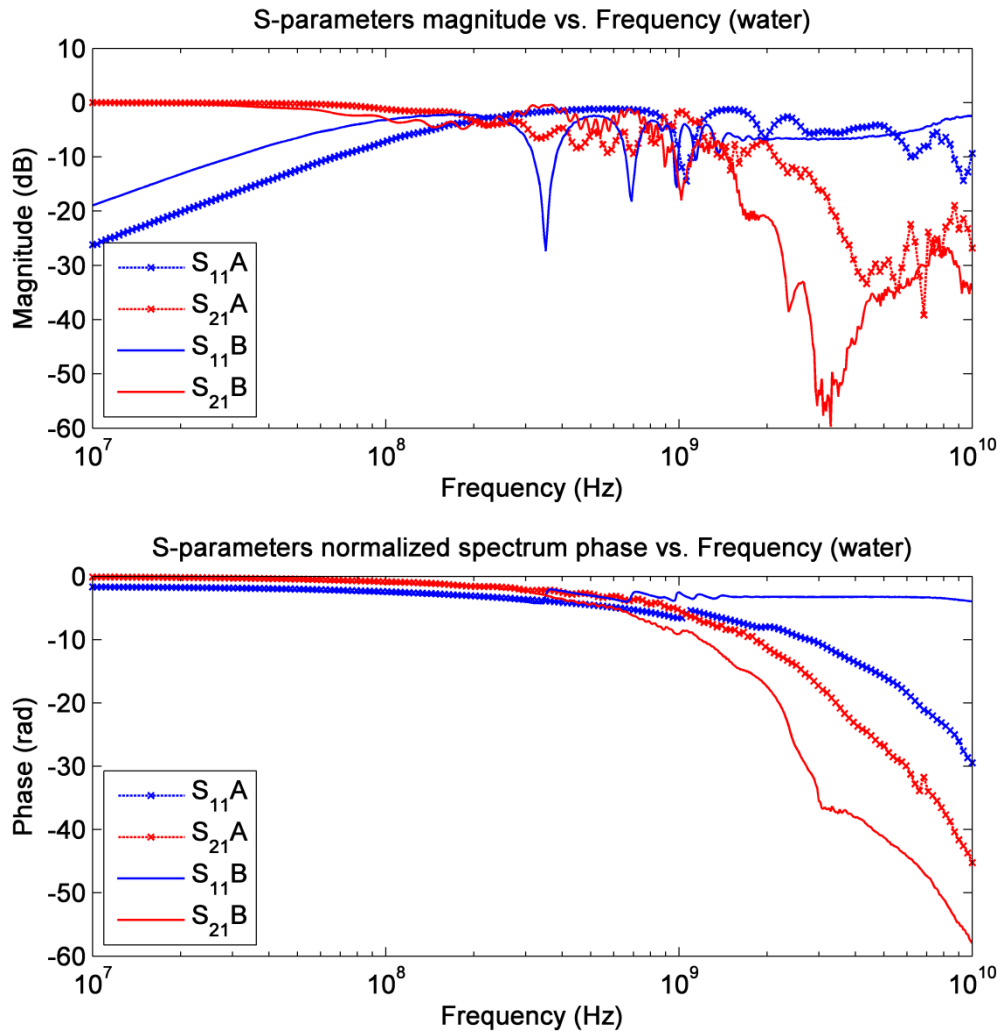


Figure 5.2 Measurement results compared for sensor A and B with water as MUT.

When measuring on water, the main impedance mismatch is where the transmission line meets the sensing area that carries the MUT. The distance between the resonances for sensor A is thusly defined by the electrical length between the walls of the container in the middle of the sensor instead. Meanwhile, the case of sensor B remains the same as the transmission line meets the sensing area at coaxial transition. For sensor B, the electrical length increases because the wavelength is reduced due to MUT while the physical length remains the same. Thus, the resonance frequency for sensor B is much lower than when measuring on air. The physical sensing length for sensor A becomes much smaller because the main impedance mismatch is where the CPW meets the container that carries the water. As the wavelength is also reduced, the electrical length remains approximately the same. Therefore, the resonance frequency for sensor A is much higher than for sensor B, as shown in Figure 5.2.

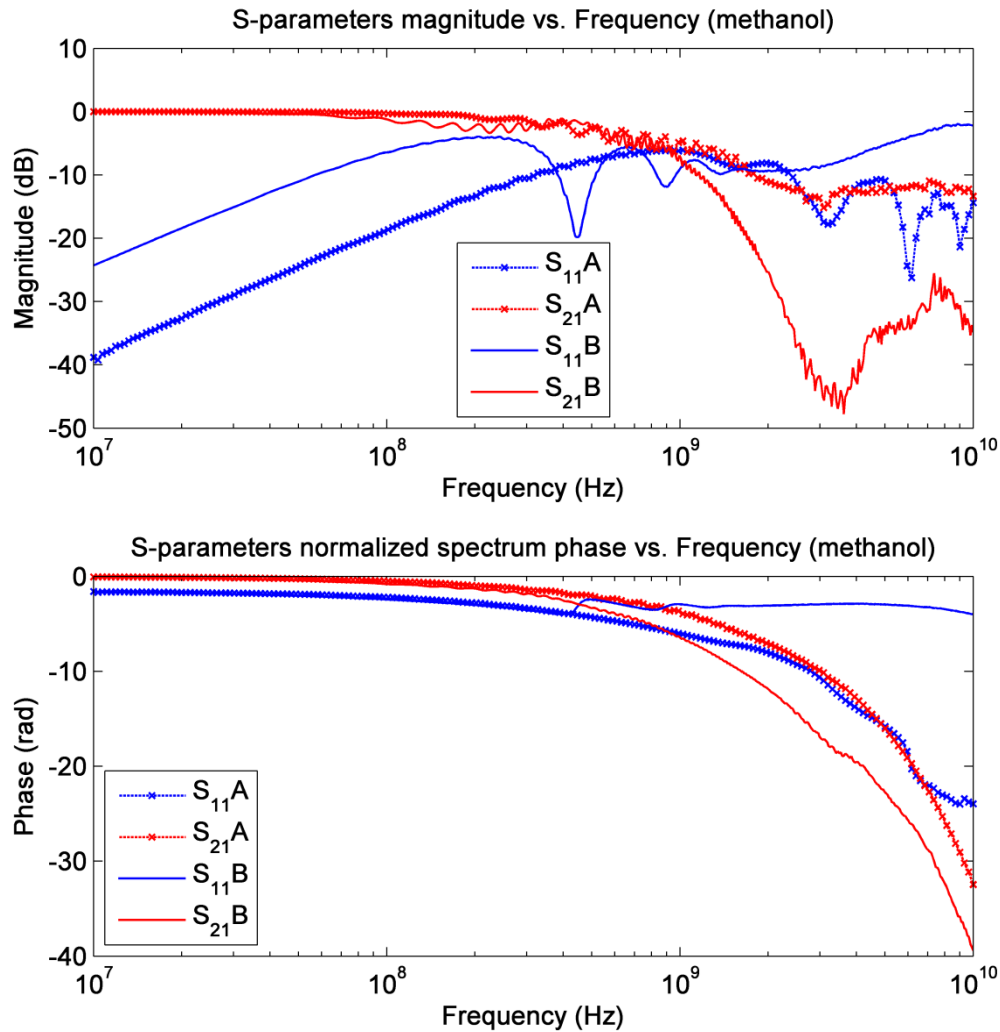


Figure 5.3 Measurement results compared for sensor A and B with methanol as MUT.

Similar pattern is observed for methanol as for water. When measuring on MUT other than air, the physical sensing length for sensor B is much longer than that of sensor A. Therefore, the electrical length for sensor B is larger. This results in the decrease of the resonance frequency where the reflection loss peaks. In addition, the vertical transitions on sensor B introduce more impedance mismatches. This also results in increased reflection loss for sensor B at higher frequencies.

5.1.2 Sensor B and sensor C

No device for thickness control is constructed for sensor C. The comparisons are therefore presented only for MUTs that fully cover both sensors. They are assumed infinitely thick for the sensibility of both sensors. As has been discussed in 4.3.2, there is a correspondence between the measurement results on the two sensors for different

types of MUTs. Thusly, it can be concluded that the shape of the PCB can be altered without affecting its measurement performance. With this knowledge in hand, more prototypes based on this model can be constructed and adapted to different geometries in future research, without altering the characteristics of the CPW.

5.1.3 Calculated relative permittivity

To understand the actual performance of the three sensors, permittivity is calculated from measured S-parameters. Measured S-parameters differ between sensors because the sensors are designed and constructed uniquely, and thusly have distinct impedance transitions. However, the derivation process via bilinear calibration procedure (BCP) peels off the possible differences between models and sensors. This in turn makes the comparison of material property – permittivity possible, which improves the understanding of the differences between the CPW sensors.

BCP as described by equation (25), is used to calculate the permittivity of the methanol from the S-parameters. Water, air and acetone are used as calibration MUTs for sensor A. Water, air and ethanol are used as calibration MUTs for sensor B and C. The calculated permittivity of methanol is compared for sensor A, B and C, including a reference from literature, in Figure 5.4.

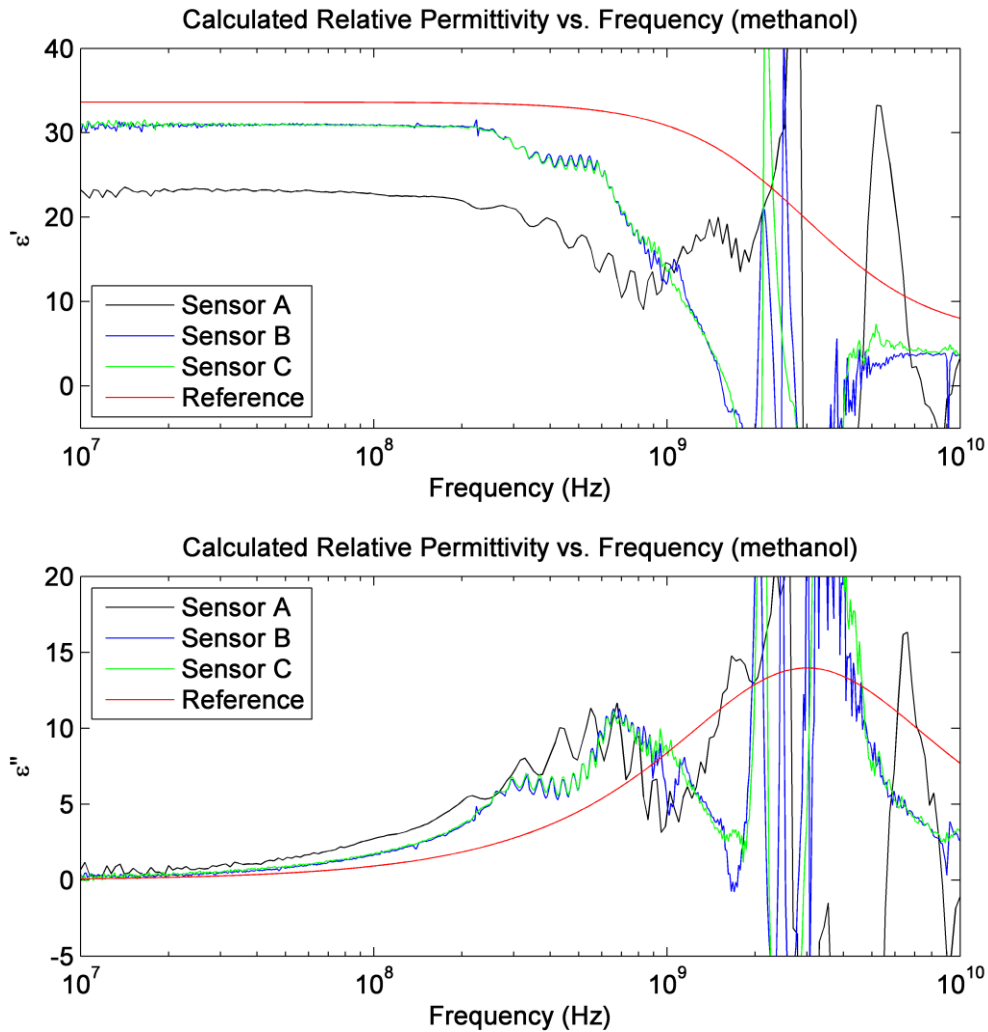


Figure 5.4 Calculated relative permittivity of methanol.

In this case, sensor B and C produce close results compared to reference permittivity, while sensor A produces results that deviate further. The difference in calculated permittivity between sensor A and B can be explained by the observed deviation in S-parameters for methanol in Figure 5.3.

The calculated permittivity starts to fluctuate and deviate from literature value significantly at frequencies above 200 MHz. This is due to the limitation of BCP. The solution of BCP is divergent at frequencies corresponding to multiples of one quarter wavelength in the sample for calculation from reflection loss (S_{11}) and a half wavelength for transmission loss (S_{21}) (Folgerø, 1996).

5.2 Simulation and experiment

In chapter 3, experiment and simulation results were compared for sensor A. They showed a close resemblance to each other. In this section, the comparison between experiment and simulation results for sensor B is discussed.

Transmission and reflection loss and their phase information are compared for experiments and simulations performed on sensor B, as shown in the following figures.

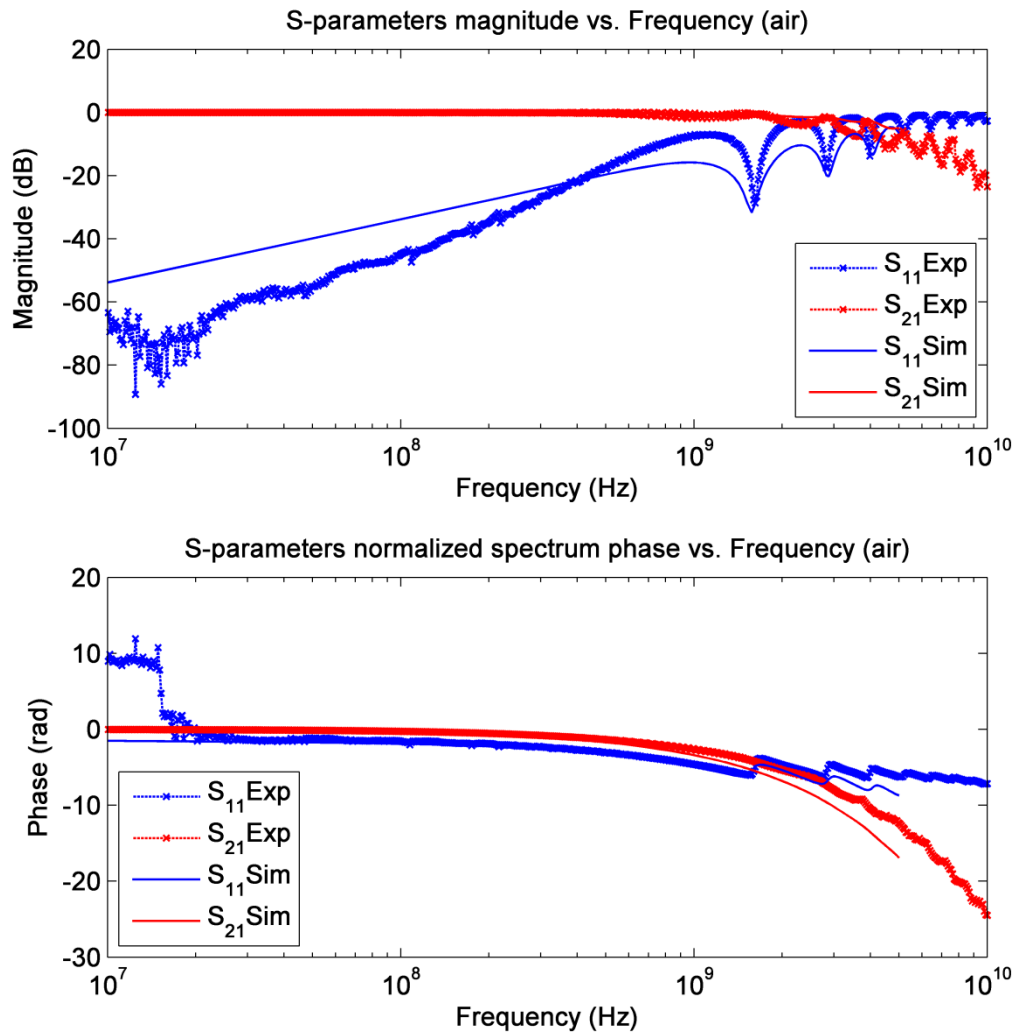


Figure 5.5 Comparison between experiment and simulation results taken with air as MUT on sensor B.

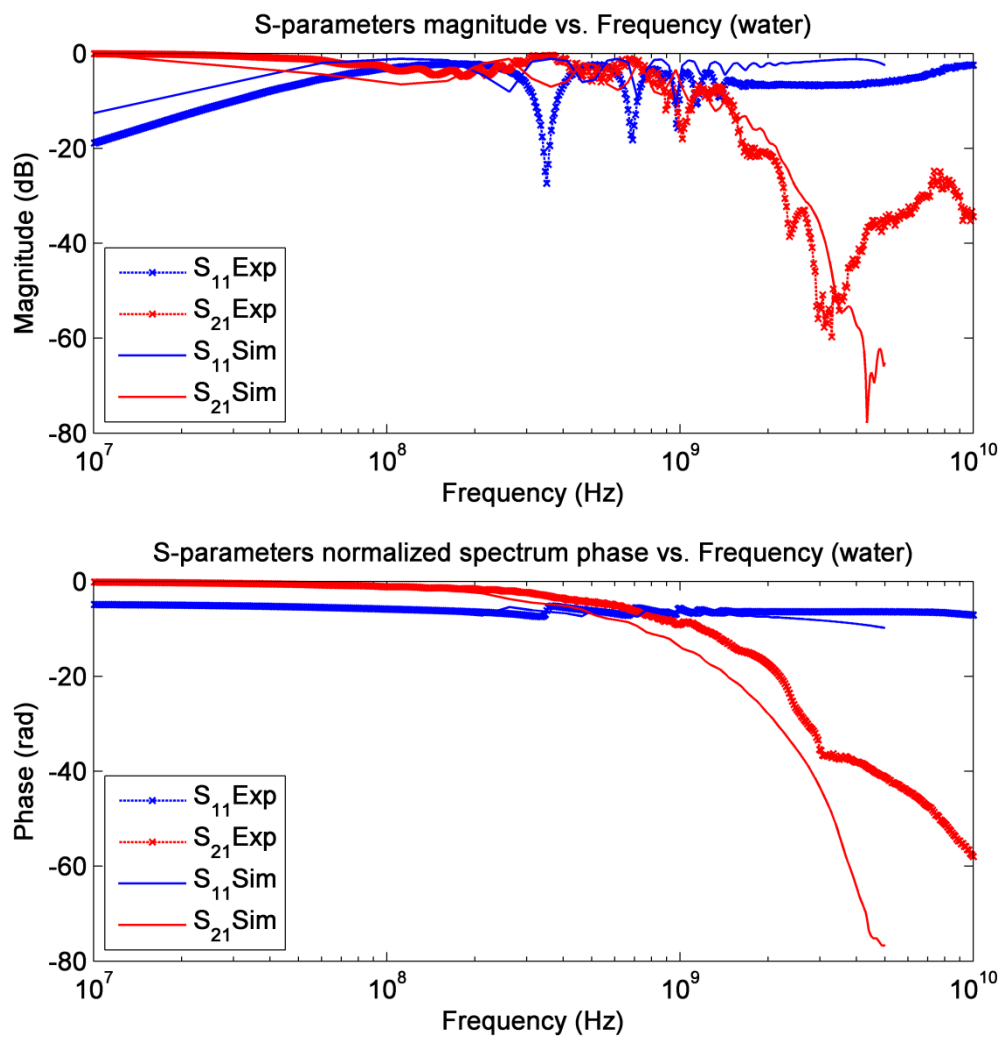


Figure 5.6 Comparison between experiment and simulation results taken with water as MUT on sensor B.

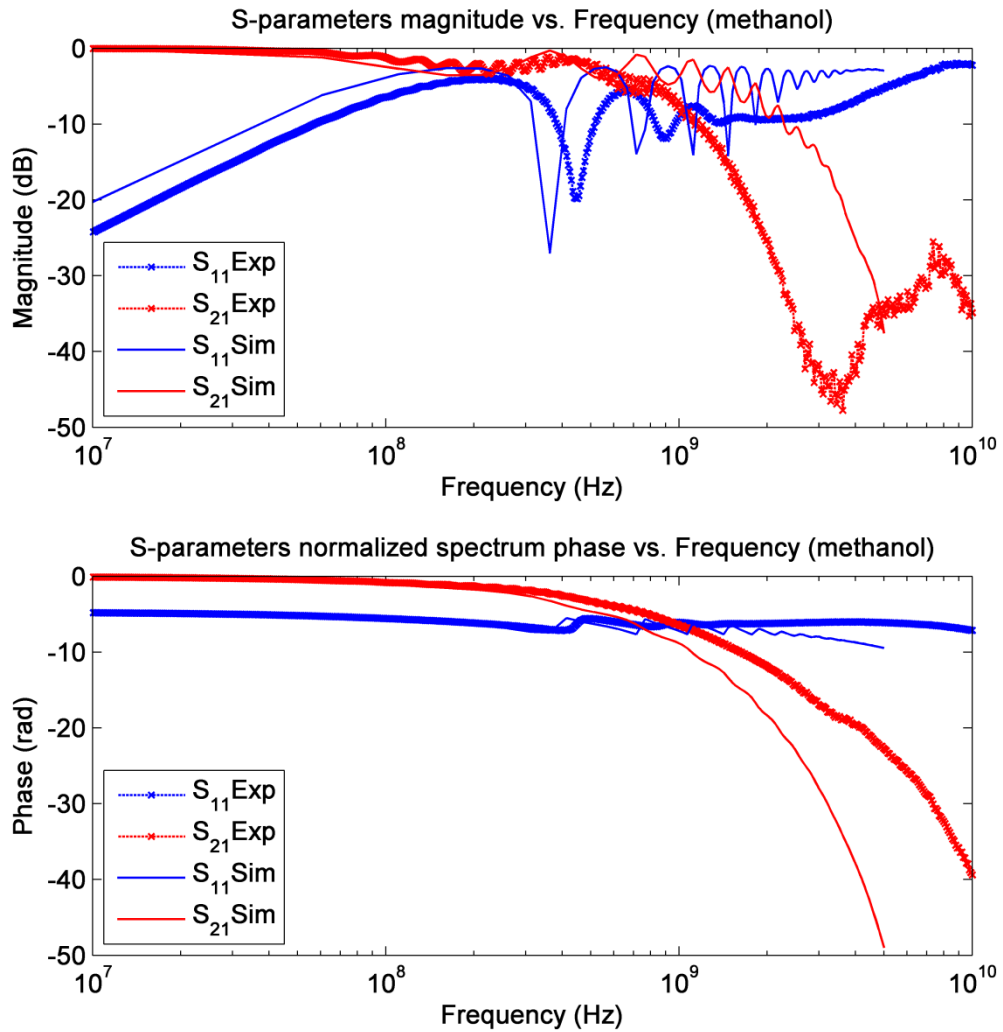


Figure 5.7 Comparison between experiment and simulation results taken with methanol as MUT on sensor B.

Some difference between simulation and experiments results can be identified in these figures. However, the deviation is small between 10 MHz and 10 GHz. There is a bigger deviation in the case of methanol, and the difference spreads across the entire frequency spectrum. It might have been caused by permittivity's dependency of temperature in the experiment.

The simulation results produced by COMSOL are thusly verified against experimental ones. This close resemblance confirms the viability of using COMSOL in modelling and simulating CPW sensors.

5.3 Leakage of liquid in experiment

In the beginning phase of the experiments, leakage of MUTs into the underside of the PCB surface became a significant problem. In the original design for both sensor B and

C, the flexible CPW is placed on a PVC substrate without adhesive in between. This is to avoid introducing another layer of a different material (adhesive) between the CPW and the substrate. The CPW is fixed onto the substrate by the silicone gel placed above along the rectangular edges only. The gel also serves the purpose of preventing the MUT to leak under the CPW.

While the experiment was conducted successfully with water as MUT, problem was encountered for other MUTs such as methanol. The MUT leakage between the CPW and the substrate was discovered by visual inspection. A further comparison of the measurement results confirms a difference in measured S-parameters for air before and after the measurement. This is likely caused by the MUT residue. The leakage may have been caused by different physical properties of MUT such as surface tension.

Consequently, a new design in addition to the silicone gel was implemented. “Araldite plus”, a strong adhesive 2-component epoxy was used in the design. It was placed between the CPW and the substrate to ensure that they are adhered together. Further experiments confirm no leakage after the re-design.

5.4 Sensing of non-uniform layers

Non-uniformity in thickness of the liquid layer inside the sensor leads to change in effective permittivity of the area above the sensor. By using BCP, S-parameters can be transformed into effective permittivity to interpret the thickness information of the MUT.

In chapter 4, it has been described that the geometry of MUT is controlled by a POM phantom in the experiments on sensor B. The non-uniformity in thickness is realized by liquid MUT confined in the form of slope by the phantom. The aim is to observe how the change of calculated effective permittivity is related to the variations in the thickness. Thus, knowledge can be gained on how effective permittivity is affected by the non-uniformity in thickness.

The results confirm that for thicknesses above 3 mm, a same amount of MUT leads to a similar measurement result, regardless of the non-uniformity in thickness. However, the thickness at the lower side of the MUT cannot be reduced to smaller than 3 mm in this project. This is caused by silicone sealing at the edge of the surface, which is about 3 mm thick. It was nevertheless possible to take measurement without the phantom for MUT with different thicknesses.

5.4.1 Effective permittivity and non-uniformity

BCP is used to calculate the permittivity of the MUT. Water, air and ethanol are used as calibration MUTs. As an example, the real and imaginary parts of the calculated permittivity for ethanol with various thicknesses are shown in Figure 5.8.

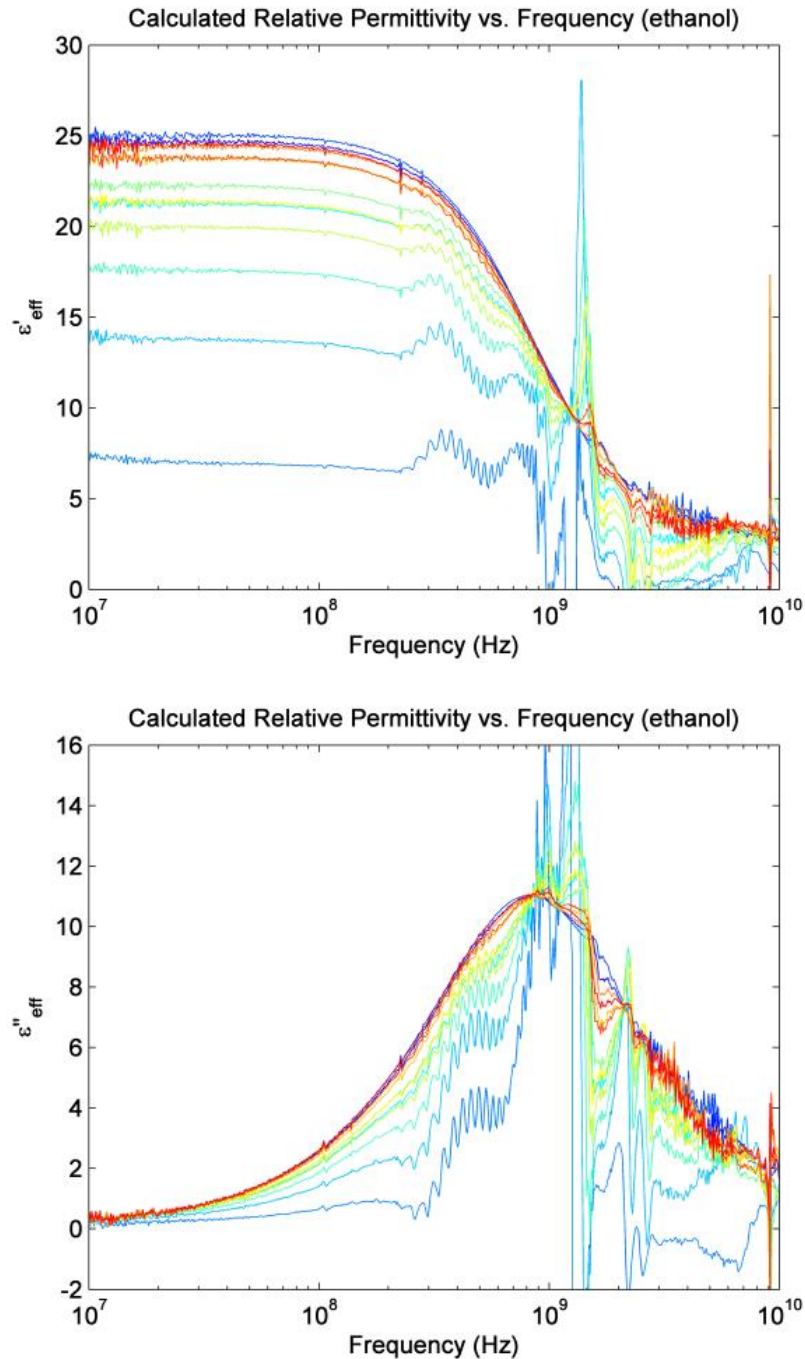


Figure 5.8 Brief comparison of calculated permittivity for ethanol with different thicknesses.

Sensor B is able to detect the difference in permittivity caused by thickness variation at frequencies up to 1 GHz. The permittivity distribution is distinct at frequencies lower

than approximately 200 MHz. The calculated permittivity fluctuates vastly at higher frequencies due to the calculating limitation of BCP.

As the derivation of permittivity is stable at frequencies below 100 MHz, permittivity averaged between 10 MHz and 100 MHz is taken and plotted against their respective thicknesses for ethanol, water and air in the following figures.

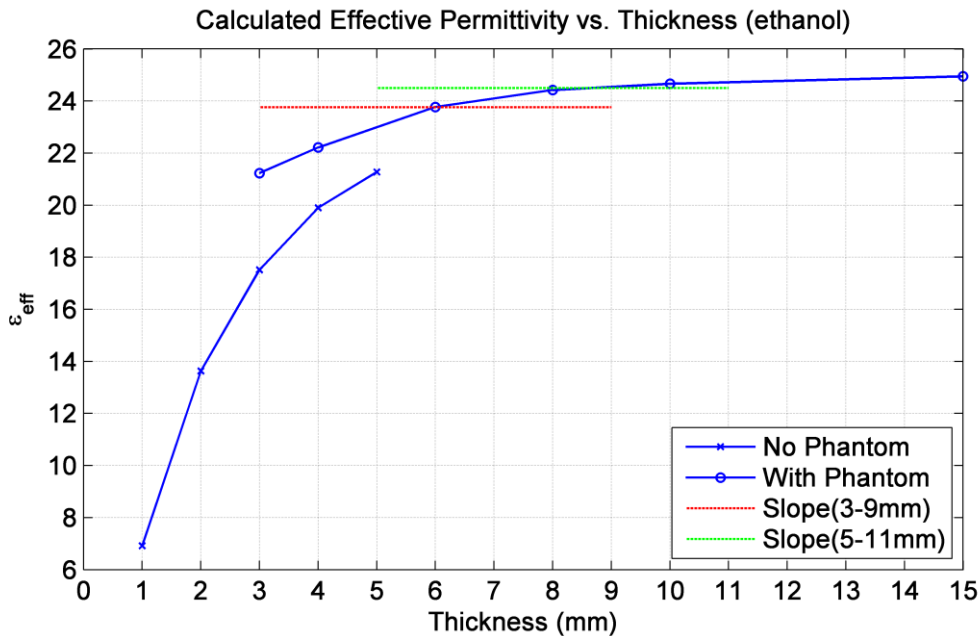


Figure 5.9 Calculated effective permittivity as a function of thickness of ethanol.

The ability of the sensor to measure thickness variations is reduced as thickness increases (blue lines). It is not able to detect thickness variation for liquid thicker than about 15 mm. In the two cases where slope is created (horizontal lines in red and green), their permittivity matches the cases when the thickness of the liquid is the average of that of the respective slope (as the horizontal lines cross with blue line). This observation confirms that same amount of liquid has similar effective permittivity, regardless of non-uniformity, for thickness above 3 mm.

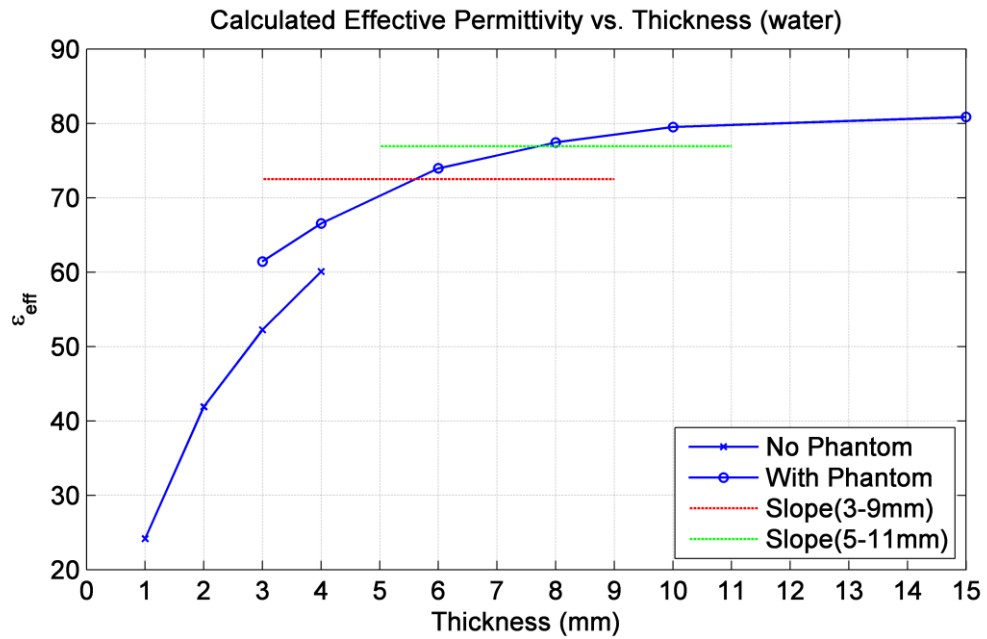


Figure 5.10 Calculated effective permittivity as a function of thickness of water.

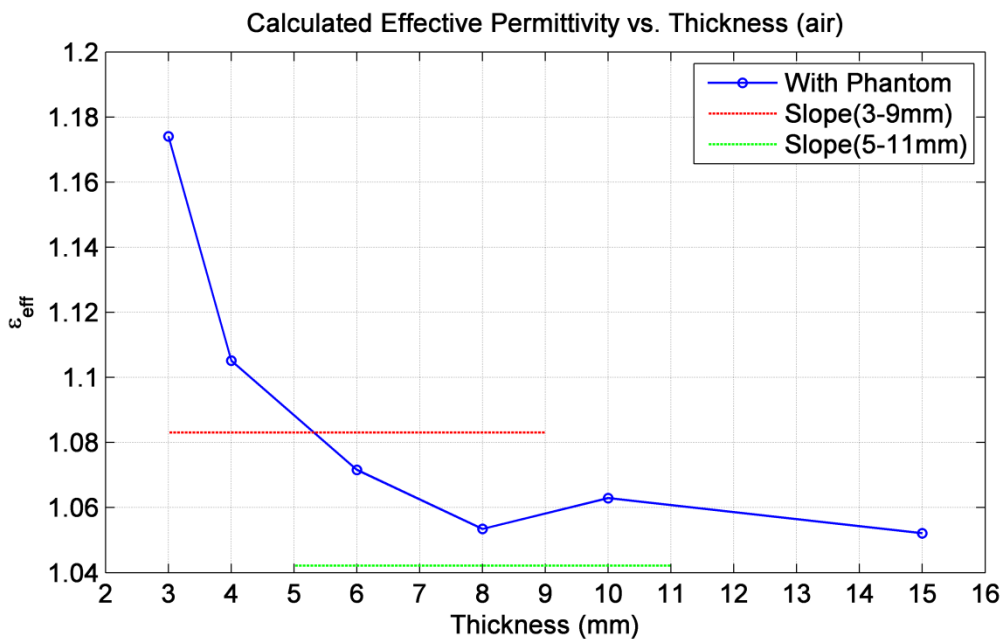


Figure 5.11 Calculated effective permittivity as a function of thickness of air.

In the case of air, the sensor is still able to detect the small difference in effective permittivity caused by varying thicknesses. Again, the sensitivity is reduced significantly at thickness above 15 mm.

6 SUMMARY

In this chapter, the conclusions of the project are presented. In addition, the outlook for the researched subject is addressed.

6.1 Conclusion

The possibility of using flexible PCB to construct CPW-based sensors for near-surface permittivity sensing is examined in this project. Two sensors addressed as sensor B and C, are built to examine the viability of different designs. These designs are generated from the idea that the sensor is to be applied in an industrial environment. The design of CPW that is implemented on both sensors builds on one previous prototype addressed as sensor A. In the new design, the effective sensing length is prolonged. Transition from coaxial to coplanar is completely re-designed for vertical mounting instead of horizontal connection. Flexible PCB is used as the material for CPW replacing traditional PCB. In addition, while sharing the same implementation of CPW, the two sensors differ in their shapes, i.e. how the MUTs are contained.

The results show that the two new sensors produces more accurate permittivity measurement than sensor A, at frequency lower than 200 MHz and for liquid with static permittivity between 1 and 80. This is due to increased sensing length on the new sensors. At higher frequencies, the calibration method BCP is not able to perform reasonable permittivity calculation from the measured S-parameters. It is therefore hard to determine whether the sensors are still correctly measuring S-parameters.

The CPW built on flexible PCB is verified to be effective for near-surface permittivity measurement. In addition, sensor C produces similar results as sensor B. This confirms

the viability of bending CPW to fit different experimental conditions. Therefore, the flexible CPW-based sensor is potentially suitable for industrial application. Furthermore, the result confirms that bending does not affect the sensitivity of the sensor. The design is stable and same characteristics can be reproduced.

The simulation software COMSOL Multiphysics used in the project is confirmed to be stable in producing realistic results, as have been verified against experimental data. As discussed in Chapter 5, there are often experimental conditions that are not easily achievable. For example, the silicone sealing prevented the POM phantom from forming a liquid slope at a thickness thinner than 3 mm. Contrariwise, the shape of the liquid can be easily defined in the simulation tool. Difficulties were encountered in simulations for liquids with high permittivity, as high quality mesh configuration required for simulating the liquid cannot be achieved by the computational resources used in the project. For similar reason, it can also take up to 16 hours for simulation to finish a complete frequency sweep. However, the mentioned drawbacks can be resolved by improving computer hardware. Consequently, using a simulation tool to assist the sensor design as well as experiments is helpful.

Non-uniform thin layers of the petrochemical can be sensed by permittivity measurement using CPW sensors. The sensitivity with regard to thickness of the layer is reduced as the thickness rises. However, the change in effective permittivity due to thickness variation can be detected regardless of the type of MUT. Even small changes (difference down to 0.01) in permittivity caused by thickness variations are detectable. For MUT with thickness above 3 mm, the measured S-parameters for the same MUT with the same average thickness are almost the same, whether it is in flat form or slope form. Thus, it can be concluded that for thickness above 3 mm, the calculated effective permittivity of MUT does not vary with different uniformities in thickness, as long as the average thickness across the sensor area is the same.

6.2 Outlook

It is of importance to the oil and gas industry to reduce operational costs. In a world market with falling oil price, it becomes harder to be profitable to operate offshore or subsea field. Real-time monitoring and control of gas hydrate deposition in the pipelines are possible ways of developing improved flow assurance scheme and technology for the future. Dielectric spectroscopy conducted by CPW sensor holds some obstacles that remain to be solved, some of which have been explained in this project. However, it is a

promising direction to devote research effort into. The use of CPW in sensing thin layers of petrochemical fluids above the sensor is proven viable. Such technology allows sensors to be mounted on the pipe wall and to characterize the type of material close to it. This can eventually lead to the development of a non-intrusive sensor for monitoring and detecting gas hydrate deposition.

During the project, several noteworthy findings may be beneficial to future research. Because the characteristics of the sensor vary with its geometry, more effort can be put into optimizing the design to improve the quality of measurement. One also needs to bear in mind that the optimization would only be effective for a limited frequency range. Hence, it is recommended that one first locate the ideal frequency range that is suitable for the specific measurement purpose. Afterwards, the work on detailed mechanical design and optimization can be conducted for the selected frequency range.

In order to implement CPW sensors into pipeline in high-pressure condition, more reliability testing is needed. For example, leakage can occur under high pressure at the vertical transition from CPW to coaxial lines. Pressure and stress testing can be introduced in future research to optimize the mechanical design of the sensors. Meanwhile, in order to monitor hydrate formation, there is a need for further research to extract information on hydrate from the measured effective permittivity spectra.

The use of simulation tool assisted sensor design. It has provided helpful test ground prior to the sensor construction. Therefore, incorporating simulation to assist future research is advised. With improved computational resources, accurate and trustworthy simulation results can be achieved. Unlike configuring the setups and the measurement scenarios for the actual experiments, simulations setups are quite easily performed using the software tool. For example, calibration needs to be conducted prior to the experiments in this project, and delicate cleaning of fluid residue needs to be performed after each experiment. Additionally, the control of the fluid thickness or geometry is difficult, and the result is not ideal. On the contrary, in the simulation tool, setup process is eliminated and environment can be configured accurately. Moreover, simulation probes can be deployed in the model to collect data that are not accessible in actual experiments. Therefore, it is recommended that simulation be incorporated in further research.

Slope shape is considered as a test option for non-uniform thickness in the project. However, liquid or possibly gas hydrate near the surface of the pipe wall in real industrial condition would have an undefined shape. It is thusly useful to create random

uniformity in thickness for future testing on the subject, in addition to the slope shape. Different phantoms can be built to create a controlled non-uniformity on the sensors. Simulation environment can be configured similarly for this purpose as well.

Limitation of BCP in producing permittivity calculation is met at frequencies in GHz range. New method for calibration and calculation can be investigated or created. It can be combined with BCP or to work by itself. Thus, permittivity calculation can be correctly performed across the selected frequency range.

REFERENCES

- Agilent Technologies. (2014). *Basics of measuring the dielectric properties of materials*. Retrieved from <http://cp.literature.agilent.com/litweb/pdf/5989-2589EN.pdf>
- Austvik, T., Hustvedt, E., Meland, B., Berge, L., & Lysne, D. (1995). Tommeliten gamma field hydrate experiments. *Multiphase 95—Where Are We on the 'S' Curve*, 539.
- Chemical polarity. (n. d.). *Wikipedia*. Retrieved February 4, 2015, from http://en.wikipedia.org/wiki/Chemical_polarity
- Chen, L. F. (2004). *Microwave electronics : measurement and materials characterisation*. Chichester ; Hoboken, NJ: John Wiley.
- Debye, P. J. W. (1929). *Polar molecules*. New York: The Chemical Catalog Company, inc.
- Dipole Relaxation. (n. d.). *Electronic Materials*. Retrieved August 10, 2015, from http://www.tf.uni-kiel.de/matwis/amat/elmat_en/kap_3/backbone/r3_3_2.html
- Electric dipole. (2015). *Encyclopædia Britannica*. Retrieved February 17, 2015, from <http://global.britannica.com/EBchecked/topic/182518/electric-dipole>
- Folgerø, K. (1996). Bilinear calibration of coaxial transmission/reflection cells for permittivity measurement of low-loss liquids. *Measurement Science and Technology*, 7(9), 1260.
- Frei, W. (2013). Modeling of coplanar waveguides. *COMSOL Blog*. Retrieved April 19, 2015, from <https://www.comsol.com/blogs/modeling-coplanar-waveguides>

- Grant, I. S., & Phillips, W. R. (1990). *Electromagnetism* (2nd ed.). Chichester England ; New York: Wiley.
- Guo, B., & Ghalambor, A. (2012). *Natural gas engineering handbook* (pp. 1 online resource). Retrieved from <http://app.knovel.com/web/toc.v/cid:kpNGEHE000/viewerType:toc/root/slug:natural-gas-engineering-2>
- Hatton, G., & Kruka, V. (2002). Hydrate blockage formation-Analysis of Werner Bolley field test data. *DeepStar CTR*, 5209-5201.
- Haukalid, K. (2011). *Den coplanare bølgelederen som permittivitetssensor*. Bergen: Institutt for fysikk og teknologi Universitetet i Bergen.
- Holzman, E. (2006). *Essentials of RF and microwave grounding*. Boston: Artech House.
- Jakobsen, T., & Folgerø, K. (1997). Dielectric measurements of gas hydrate formation in water-in-oil emulsions using open-ended coaxial probes. *Measurement Science and Technology*, 8(9), 1006.
- Khandpur, R. S. (2006). *Printed circuit boards : design, fabrication, assembly and testing*. New York: McGraw-Hill.
- Kremer, F., & Schönhal, A. (2003). *Broadband dielectric spectroscopy*. Berlin ; New York: Springer.
- Lingelem, M., Majeed, A., & Stange, E. (1994). Industrial experience in evaluation of hydrate formation, inhibition, and dissociation in pipeline design and operation. *Annals of the New York Academy of Sciences*, 715(1), 75-93.
- Maslin, M., Owen, M., Betts, R., Day, S., Jones, T. D., & Ridgwell, A. (2010). Gas hydrates: past and future geohazard? *Philosophical Transactions of the Royal Society A: Mathematical, Physical and Engineering Sciences*, 368(1919), 2369-2393.
- Nicholas, J. W., Dieker, L. E., Sloan, E. D., & Koh, C. A. (2009). Assessing the feasibility of hydrate deposition on pipeline walls—Adhesion force measurements of clathrate hydrate particles on carbon steel. *Journal of Colloid and Interface Science*, 331(2), 322-328.
- Nicolson, A., & Ross, G. (1970). Measurement of the intrinsic properties of materials by time-domain techniques. *Instrumentation and Measurement, IEEE Transactions on*, 19(4), 377-382.
- Ramo, S., Whinnery, J. R., & Van Duzer, T. (1994). *Fields and waves in communication electronics* (3rd ed.). New York: Wiley.
- Sloan, E. D., & Koh, C. A. (2008). *Clathrate hydrates of natural gases* (3rd ed.). Boca Raton, Fla.: CRC Press.

Vrba, J., & Vrba, D. (2013). Temperature and frequency dependent empirical models of dielectric properties of sunflower and olive oil. *Radioengineering*, 22(4).

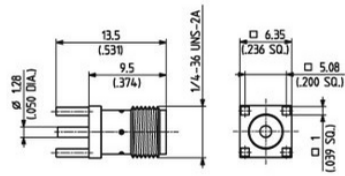
APPENDIX

Table 6.1 Table of detailed specifications on FPC

Layers	1 - 2	
Material	Polyimide, PEEK	
Board Dimension (max)	250mm X500mm	
Board Dimension (min)	5mm X10mm	
Copper thickness	1/3oz , 1/2oz , 1oz	
Finished Board Thickness	0.01mm--0.03mm	
Min. hole diameter	0.2mm(CNC)(8mil)	
Hole wall copper thickness	10-35um	
Hole diameter tolerance	±0.075mm	
Min. Hole to hole space	0.50mm	
Min trace width and Space	1/3 OZ	2.0mil/2.0mil
	1/2 OZ	2.5mil/2.5mil
	1 OZ	3.0mil/3.0mil
	2OZ	4.0mil/4.0mil
Trace tolerance	±20%	
Min. Annular ring	0.2mm	
Min center distance in contiguous finger	0.10mm	
Solder resistance clearance /coverage	0.15mm/0.1mm	
Soldering Resistance thickness	10um	
Silkscreen text height	0.8mm	
Silkscreen line width	0.15mm	
Based material(PI) thickness	0.025mm-0.125mm	
Selective finish	ENIG	Ni: 1—6 um
		Gold: 0.03—0.10um
	OSP	OSP film:0.2—0.7um
Profiling	Punching ,Routing ,V-cut	Tolerance :+/-0.13mm
Reinforce Material	PI , FP4 , Steel 3M adhesive , PET	
Design space	Min. Hole to hole	0.50mm
	Min. Copper to outline	0.20mm

Straight PCB jacks (female)

- Without stand-off



HUBER+SUHNER type	Item no.	Packaging	Plating body	Mounting hole
82_SMA-50-0-1/111_NE	22543359	single	gold	ML41
82_SMA-50-0-1/111_NH	22644334	bulk 100 pcs.		

Figure 6.1 Specification of coaxial SMA connector.

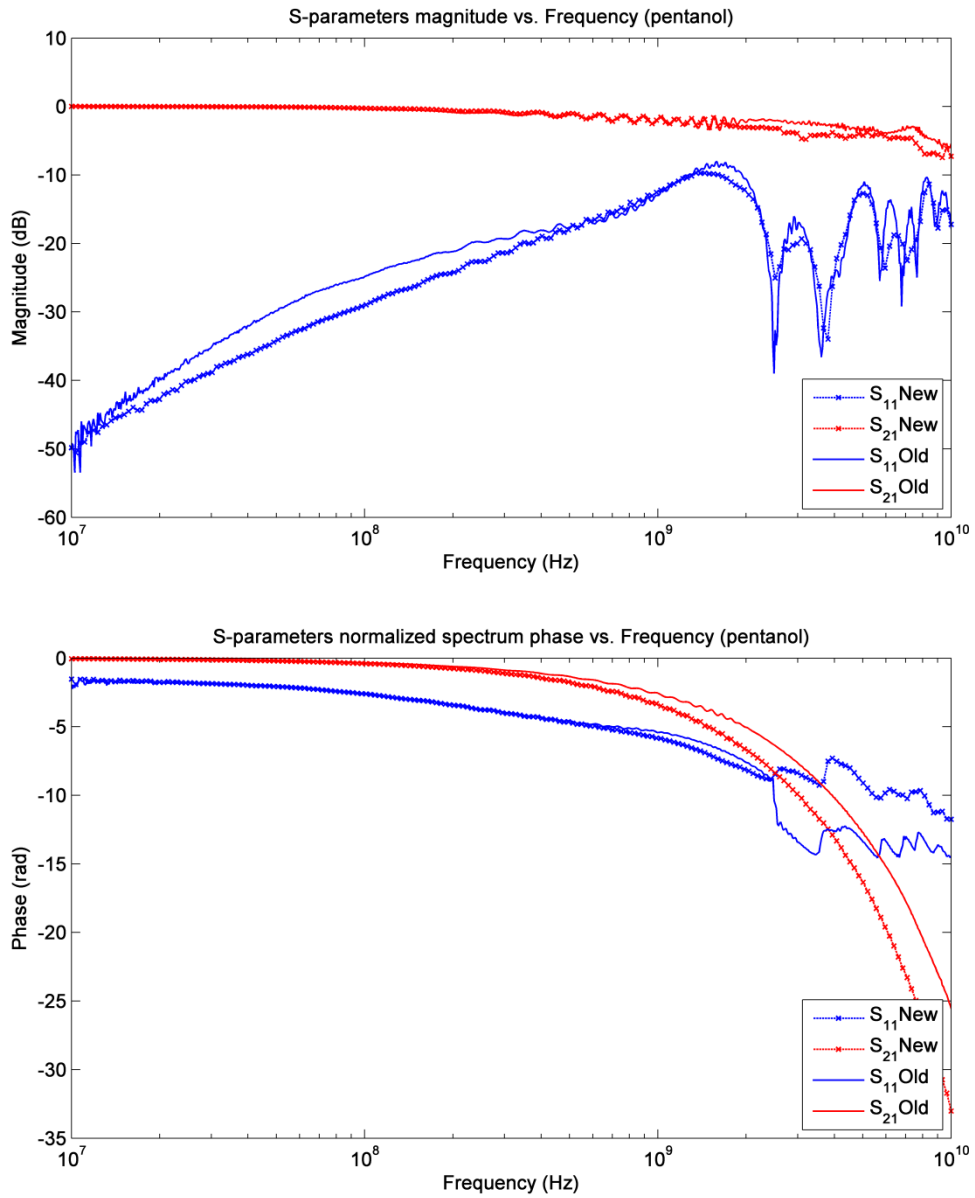


Figure 6.2 Comparison between new and old measurement taken with 1-pentanol as MUT on sensor A.

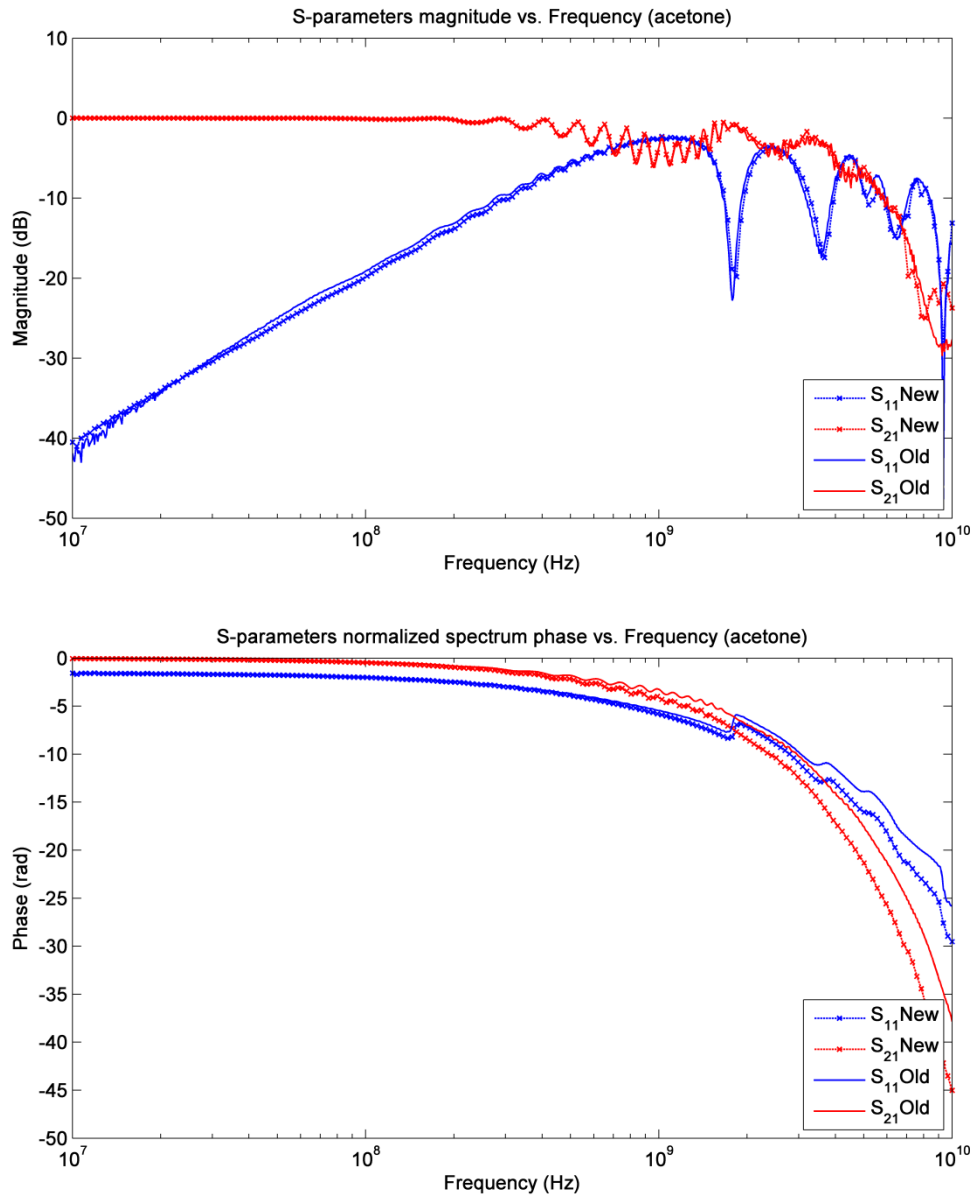


Figure 6.3 Comparison between new and old measurement taken with acetone as MUT on sensor A.